SIMULATION AND ANALYSIS OF Co-Pt BASED GRANULAR MAGNETIC RECORDING MEDIA NEAR THE CURIE TEMPERATURE

AARON KAMMULA

A THESIS SUBMITTED TO
THE FACULTY OF GRADUATE STUDIES
IN PARTIAL FULFILLMENT OF THE REQUIREMENTS
FOR THE DEGREE OF
MASTERS OF APPLIED SCIENCE (MASc)

GRADUATE PROGRAM IN ELECTRICAL AND COMPUTER ENGINEERING
YORK UNIVERSITY
TORONTO, ONTARIO

April 2024

ABSTRACT

This thesis presents the modelling and simulation of Co-Pt based thin-films that can be used in magnetic data storage with the use of VAMPIRE, a magnetization dynamics software for nanomaterials. The mathematical models of the magnetization dynamics and structure of the thin films, along with a procedure to simulate the behaviour of magnetic nanomaterials at varying temperatures and material properties, is analyzed. Afterwards, the switching probability in terms of the applied magnetic field magnitude and angle, cooling rate and material properties such as layer thickness, anisotropy, saturation magnetization and exchange parameter are analyzed for each sample. Because Co-Pt multi-layers can exist in stoichiometries outside of 50:50, this allows for tunable anisotropy and magnetization saturation values. An effective medium model is used to describe the magnetic properties of the multi-layer thin-film, an atomistic spin model is used to model the magnetic spins, and the Landau-Lifshitz-Gilbert equations (LLG) are used to model the magnetization dynamics under the presence of thermal effects. Our results confirm that materials with a higher uniaxial anisotropy value (K_{ui}) have a higher blocking (T_B) to Curie temperature (T_C) ratio, resulting in larger areal densities and writing times. However, such materials require a higher write field, which has a limit. If a higher cooling time is allowed, then writing becomes easier.

DEDICATION

This thesis is dedicated to the people who have supported me throughout my education – directly or indirectly. Thank you all for helping me throughout this adventure until the very end. I would not have been able to make it this far if it weren’t for the people who helped me throughout my education, and provided me with inspiration to study at the post-graduate level.

ACKNOWLEDGEMENTS

Words cannot express my fathomless sense of gratitude to my supervisor - Dr. Simone Pisana. His passion and expertise in the fields of heat transport and magnetism, paired with his overwhelming generosity to provide me with structured and diligent guidance throughout all of the stages of my MASc degree has provided me with many valuable skills and knowledge that will prepare me for future academic and industrial pursuits. I would also like to express my gratitude to the other member of my supervisory committee, Dr. Anatharaman Kumarakrishnan, for his valuable time and guidance.

A debt of gratitude is also owed to the members of the HEATED lab for their generous advice, encouragement and support during tough times. All of these attributes have contributed to creating a productive and welcoming environment for me.

It is impossible to extend enough gratitude towards my family and friends. My family - especially my parents, have given me the financial support and encouragement I needed throughout my life. My friends have helped and provided me with reminders to take care of my physical and mental health when stressed.

TABLE OF CONTENTS

LIST OF FIGURES

LIST OF TABLES

LIST OF ACRONYMS & MATHEMATICAL SYMBOLS

a	Lattice spacing value
ASD	Atomistic spin dynamics
ASTC	Advanced Storage Technology Consortium
CAGR	Compound Annual Growth Rate
CMR	Conventional magnetic recording
DFT	Density functional theory
Co-Pt	Cobalt-Platinum
FC	Field cooling
FCC	Face-centered cubic
FDT	Fluctuation Dissipation Theorem
FOM	Figure of Merit
$\hat{H}$	Hamiltonian

HAMR	Heat assisted magnetic recording
HDD	Hard disk drive
H_{app}	Applied magnetic field
H_c	Magnetic coercivity
H_K	Anisotropy field
HEATED	Heat Transport in Electronic Devices
J_{ij}	Exchange interaction value
k_B	Boltzmann's constant
K_u	Uniaxial anisotropy constant
K_{ui}	Uniaxial magnetocrystalline anisotropy constant
LLB	Landau-Lifshitz-Bloch
LLG	Landau-Lifshitz-Gilbert
M_M	Molar mass

M_S	Saturation Magnetization
N	Demagnetizing shape factor, or demagnetizing field tensor
N_A	Avogadro’s constant
N_{Steps}	Number of time-steps
N_{atoms}	Number of atoms
NE	Nearest neighbor exchange
NFT	Near-field transducer
PMR	Perpendicular magnetic recording
$\boldsymbol{S}_i$	Unit vector of the local spin moment in the direction ‘i’
SNR	Signal-to-noise ratio
T_B	Blocking temperature
T_c	Curie temperature
t_{Co}	Thickness of Cobalt

t_{Pt}	Thickness of Platinum
z	Number of spin interactions
ZFC	Zero field-cooling
β	Critical exponent
θ_H	Applied magnetic field angle with respect to K_u axis
λ	Gilbert damping parameter
μ or μ_s	Atomic spin moment
ξ	Thermal fluctuation function
ρ	Density
τ_m	Measured relaxation time
τ_N	Néel relaxation time
τ_0	Attempt time
γ	Gyromagnetic ratio

CHAPTER 1: INTRODUCTION

The hard disk drive (HDD) has supported the increasing demands of digital storage requirements for over 50 years due to its low cost and fast memory access times in comparison to tape and other media like CD's and DVD's [1]. These demands are exponentially increasing as days go by; over 300 hours' worth of video content are uploaded to YouTube every minute [2], meaning that an additional 15000 hard drives (10 TB each) are required every month to sustain this. In addition, due to the Covid-19 pandemic, increases in HDD memory are required to sustain the rapid increases in storage demands of video recording and streaming, making it possible to sustain a virtual environment that ensures everyone is able to socially distance themselves from others. Historically, the best approach to mitigate the increased demand was to increase the areal storage density, also known as the number of bits per square inch of a HDD, (more detail can be found in section 1.1.2) of the HDD by reducing the grain size of the ferromagnetic storage material [3]. However, as the grain size decreases, the magnetic energy becomes too small to ensure stable magnetization because the energy difference between the switching states is too small compared to thermal fluctuations to ensure long-term thermal stability (also known as the superparamagnetic limit) [4]. As a consequence of the superparamagnetic limit, if the grain size is too small, then if the temperature of a medium becomes too high, the magnetic spins will randomly switch states, destroying the data that was originally stored on the hard-drive. The readability of the hard-disk drive is measured by analyzing the signal-to-noise ratio of the data (more detail can be found in section 1.1.2). Ideally, a high signal and a low noise magnitude is desired [3, 4]. Therefore, an increase in magnetic anisotropy, which refers to the energy required to switch the magnetic spin system from the lowest to the highest energy state (more detail in section 1.2), is required to enforce a preferred magnetic field direction, resulting in higher thermal stability, which leads to less overall noise within the system. Thermal stability is enforced when thermal agitations are substantially less energetic than what is required to switch the preferred magnetic field direction. In perpendicular, or conventional magnetic recording (PMR/CMR, see figure 1.1), it is possible to adjust the magnetic anisotropy value through a selection of the magnetic material the recording medium is composed of [5]. Unfortunately, as the magnetic anisotropy increases, the required magnetic field to switch the magnetic spin of the grain increases, and there is a limit on how much magnetic field the HDD write head can produce (~2 Tesla) [5]. As a result, there is a trilemma (three-way compromise) between magnetic writability, thermal stability and signal-to-noise ratio (SNR) that is experienced once the grain size reaches a size below 10 nm [6], as shown in figure 1.2. As seen in figure 1.2, the smaller the grains are, the lower the product between the uniaxial magnetocrystalline anisotropy (K_{ui}) of a material and the volume (V) of the grain, which is a figure of merit (FOM) for long-term thermal stability of the data recorded in perpendicular recording methodologies (also known as conventional magnetic recording, or CMR) [1, 3]. More specifically, $\frac{K_u V}{K_b T}$ must be greater than 60 to ensure thermal stability [7].

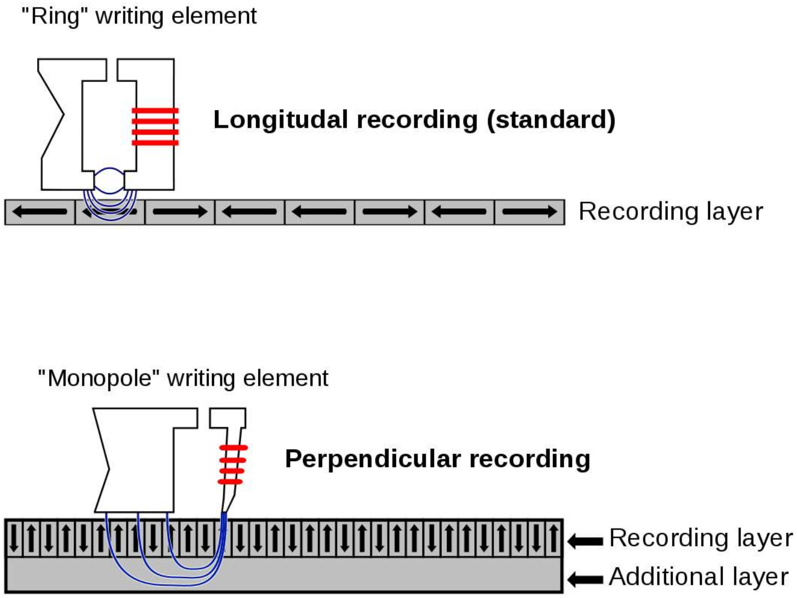

Fig. 1.1. Visualization of the two major types of magnetic recording topologies [8]. With longitudinal recording (top image), the direction of the write field is perpendicular to the spin directions. To maximize the number of spins enclosed within an area, thereby increasing areal density, perpendicular recording (bottom image) is used. With the spins being parallel to the direction of the write field, switching becomes easier. The additional layer is added to ensure the write field follows the correct direction.

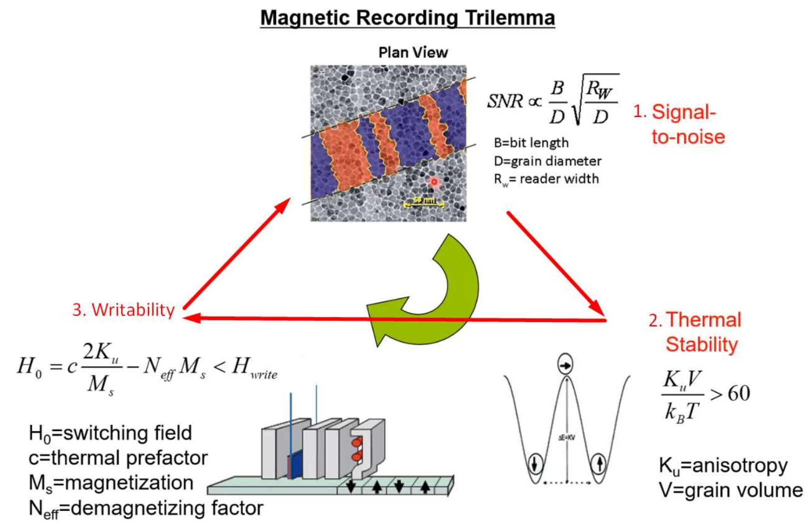

Fig. 1.2. Visualization of the magnetic recording trilemma. Unfortunately, the maximum areal density is limited when juggling these three requirements [6]. The SNR is proportional to the ratio between the bit length (B) and grain diameter (D) multiplied by the square root of the ratio between the reader width (R_W) and D ($SNR \propto \frac{B}{D}\sqrt{\frac{R_W}{D}}$). Thermal stability is attained when $\frac{K_{ui}V}{K_b T}$ is greater than 60. The switching field (H_o) of the system is proportional to the difference between the required anisotropy field ($\frac{2K_{ui}}{M_s}$) and the demagnetizing field ($N_{eff}M_s$) due to dipolar effects. The applied write field ($\boldsymbol{H}_{write}$) must be larger than $\boldsymbol{H}_o$.

When reducing the grain diameter in attempts to increase the SNR, the volume (V) decreases, thereby reducing the thermal stability ($\frac{K_u V}{K_b T}$) of the grain system. To overcome the thermal stability limitation, materials with a higher K_{ui} should be used. However, writing data into materials with a higher K_{ui} will be more difficult, as a larger $\boldsymbol{H}_{write}$ (greater than 2 T), which is limited by the HDD technology, is required [1]. To overcome such limitations, energy-assisted recording approaches such as heat-assisted magnetic recording (HAMR) have been devised in tandem with a material having a higher K_{ui} value to assist with writing data in HDD's. Although both HAMR and standard HDD systems use an actuator to scan a spinning magnetic disk (as seen in sections 1.1.3 and 1.1.1, respectively), HAMR additionally uses a nanosecond laser (for the best storage density, fast pulses are required) to temporarily heat-up the magnetic disk, making the magnetization of the grains more susceptible to the magnetic field produced by the writing coil [3]. Traditional HDD systems work by rotating a ferromagnetic, circular disk with a spindle, and using an actuator arm to read or write into each grain of the disk while it rotates. HAMR systems are an upgrade from traditional HDD systems by adding a laser diode to the actuator in order to heat up the disk, making it easier to write into. More details about how traditional HDD and HAMR systems work can be found in sections 1.1.1 and 1.1.2 of this thesis, respectively. Unfortunately, the known physical models of magnetism are not well established when the temperature of the magnetic disk is close to the Curie temperature (T_c), though reaching this temperature is necessary for optimal HAMR operation, as this makes the grains containing high K_{ui} values more susceptible towards a smaller write field (more information can be found in section 1.1.3) [3]. However, accurate knowledge of the switching physics is critical in determining the future areal density recording limits of HAMR storage systems.

To better understand the physics of magnetism as the temperature approaches the Curie temperature, where all magnetic order of a magnetic material is lost, this work studies the switching dynamics of multi-layered cobalt-platinum (Co-Pt) nanocrystalline grains as a model system that can be experimentally tested. The volumes of the grains are chosen to be near that of realistic recording media and will be arranged in a Voronoi lattice, also known as a structural formation of grains that replicates the natural way grains form during fabrication of magnetic storage media. These grain ensembles are then then tested with the use of VAMPIRE, an ultrafast magnetization dynamics testing software for nanomaterials. First, an effective-medium approximation of the varying Co-Pt multi-layer configurations were made in a way that the atomic spin moment (μ_s), T_c and K_{ui} values matched the literature. It is important that these values match the literature because this indicates that our approximations are valid and match experimental values, increasing the validity of our model. Afterwards, the size of the Co-Pt particles were adjusted to get the correct coercive field value at room temperature that matched the values obtained by past experiments performed in the HEATED lab. Lastly, laser heating will be simulated, and the switching probability will be analyzed afterwards as a function of cooling speed, magnetic field intensity and angle.

The reason why it is necessary to have a software system capable of analyzing and modeling nanomaterials is because nanomaterials are very difficult and costly to fabricate. Not only is it difficult to fabricate nanomaterials, but not enough experiments have been performed on these materials at high temperatures and short timescales. Therefore, in order to save a lot of time and money, and to be able to predict the long-term usefulness of HAMR systems, a modeling approach is required to make future fabrication of nanomaterials a predictable process. The theoretical model needs to strike a balance between physical accuracy and computational cost, meaning that leading models need to be benchmarked against real data. The goal of this thesis is to make a first step in this direction by making predictions about the switching dynamics of Co-Pt based thin-films according to a leading software model that can be later tested in fast switching experiments in order to validate the theory found in the literature.

1.1: Background

This section will cover the functionality of the HDD, how it has evolved over the years, an overview of the current limitations HDDs are facing, and how modelling Co-Pt-based thin films can be helpful when used for predicting the magnetization dynamics at higher temperatures for ferromagnetic thin-films.

Additionally, the performance metrics for size, thermal stability and writing efficiency will also be mentioned and analyzed for each evolution of the HDD system. Motivations for this thesis arise from the tunability of the parameters of Co-Pt - the main goal is to produce physics models that predict the behavior of Co-Pt when various parameters are tuned. By producing predictive physics models, more information regarding how well it can improve HDDs can be obtained, meaning that it is possible to predict whether HAMR-based hard-drives will work for very high data storage densities under a given set of parameters.

1.1.1: Hard-disk drive systems – functionality

As mentioned in the introduction, the hard-disk drive (HDD) is the main storage system used in consumer electronics and storage arrays in data centers. A visualization of this system can be seen in figure 1.3. An HDD works by rotating a circular platter (disk) made out of a ferromagnetic material (more detail in section 1.3) with a spindle motor placed in the center of the platter that spins at a speed between 5400 to 7200 RPM [9]. This platter stores all of the information. To read and write into this platter, an actuator arm scans the read/write head to read the magnetization, also known as the magnitude and direction of a magnetic spin of a specified section of the disk, then either reads it as a ‘0’ or ‘1’ (up or down spin direction) with the use of a giant magnetoresistor (GMR) that changes in resistance as the spin direction changes for read operations, or applies an external magnetic field (1.5 – 2 T) to change the spin orientation(s) for write operations [9].

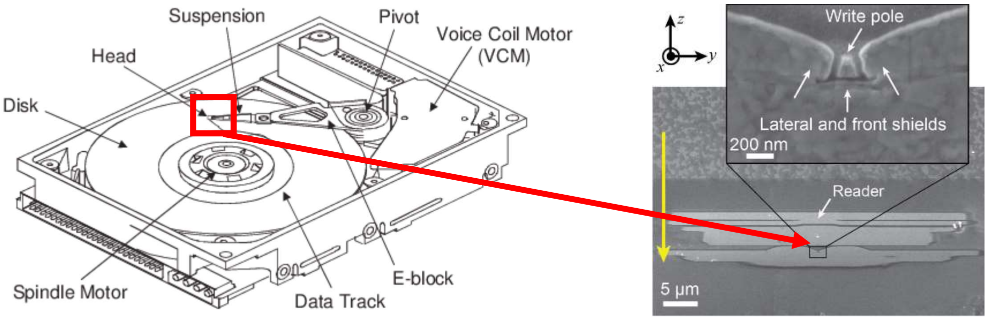

Fig. 1.3. A visualization of the mechanical components found in a typical hard-drive system (left). The read/write "head" can include an actuator that can further control the position of the head on the disk (right) [9, 10]. The yellow arrow (right) indicates the direction of the magnetic field.

1.1.2: Hard-disk drives – performance metrics and problems experienced

The reason why HDD's were able to dominate the digital storage market between 1956-2012 was because the FOM for the capacity of a hard-drive system, also known as areal density $(\frac{Tb}{in^2})$, kept increasing at a compound annual growth rate (CAGR) of at least 30% since 1956 [11]. However, according to the advanced storage technology consortium (ASTC) roadmap (see figure 1.4), the projected CAGR after 2012 has dropped to as low as 10%, which is not enough to support modern and future storage demands [12]. In order for HDDs to be cost-efficient and feasible, the areal density should reach 10 $\frac{Tb}{in^2}$ by 2025 [13]. However, at the projected rate, it is expected to reach that benchmark by 2043 (see figure 1.5 for a visualization), which is not fast enough. The reason why the CAGR of HDD's have not met expectations are numerous and complex; principally, it is taking longer than anticipated to replace PMR systems with an improved technology such as HAMR [14]. On the other hand, the areal density, a less complex variable to analyze, is primarily affected by thermal stability issues - as the grain size decreases, the magnetic spin becomes too unstable due to the increased effect of thermal fluctuations. Additionally, although a possible solution to this problem involves increasing the applied magnetic field, materials with the highest known magnetization in the writing poles are already being used, meaning that creating write heads that can produce more magnetic field is not possible [15]. Therefore, given these two road-blocks, a new system that can reduce the magnetic field required to change the spin polarity of the magnetic grains is required [15].

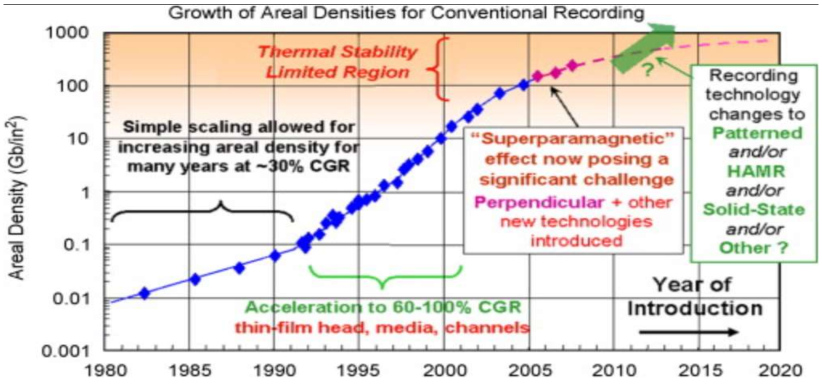

Fig. 1.4. 2010 ASTC roadmap. Note: 1000 Gb = 1 Tb [15].

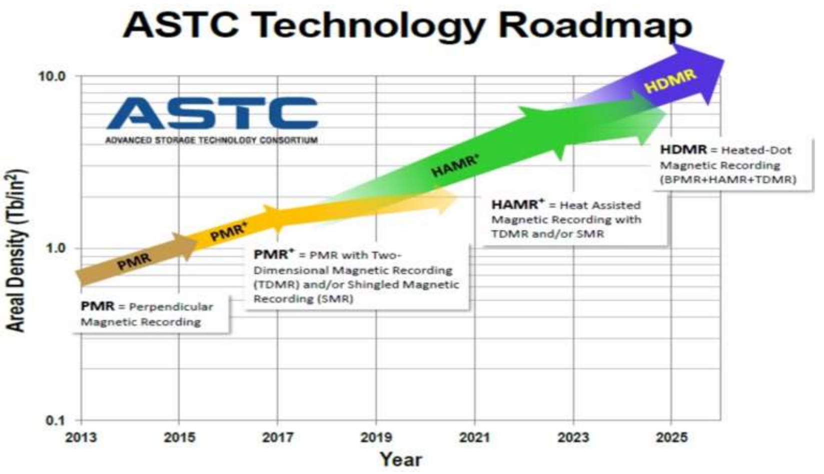

Fig. 1.5. 2016 ASTC roadmap. As seen from both figures 1.4 and 1.5, reaching the areal density benchmark with HAMR is becoming a challenge [16].

1.1.3 HAMR systems

Heat-assisted magnetic recording (HAMR) is an upgrade from the traditional PMR-based HDD system. A laser diode, along with a near-field transducer (NFT) is now added to the tip of the actuator, as seen in figure 1.6. An NFT works by concentrating the laser pulse produced by the laser diode into a small, confined space, which turns the laser pulse into an evanescently coupled wave. An evanescently coupled wave, which refers to a wave that propagates through a surface with the use of total internal reflection (TIR), then exponentially decays as it travels through a medium, is needed to exert radiational pressure over smaller particles, making them heat up faster. Afterwards, the evanescently coupled wave is absorbed in the medium, which raises its temperature, and together with the magnetic pole, which supplies the write field, is responsible for changing the polarity of the magnetic grains found on the disk within nanoseconds [17]. With an increase in the medium's temperature to a value near the Curie temperature (T_C), a smaller magnetic field is required to adjust the spin directions of smaller grains made of higher K_{ui} materials, meaning that hard drives can have higher data storage densities, while maintaining the same bit error rate. In other words, the magnetic pole does not have to produce such a high write field to change the direction of each individual spin within the grains of a medium. Although HAMR fixes the thermal stability issue experienced with the traditional PMR-based HDD system, it also shifts the superparamagnetic limit to a higher areal density. This imposes an upper limit on the areal density of the system. On top of that, due to the difficulties of collocating the NFT and the write pole, the applied field cannot be perpendicular to the surface medium, which places a constraint on the applied field angle, making it difficult to write into a magnetic medium. Unfortunately, as there are several theoretical models that differ in their result when predicting magnetization dynamics at temperatures near the Curie temperature, it is difficult to predict the long-term success of the materials. Therefore, more research is needed with regards to developing a physics model that accurately matches the theoretical and experimental values to a high degree of accuracy, thereby reducing the dependence on which type of model to use.

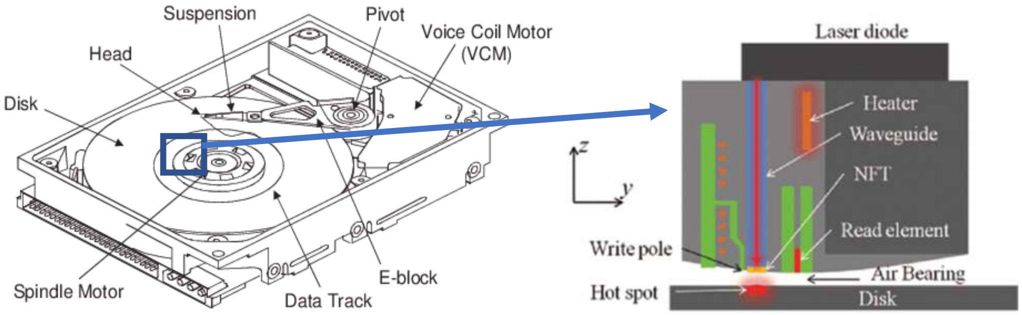

Fig. 1.6. A visualization of the changes made when implementing a HAMR system. [9, 17].

1.1.4 Thesis Motivation

As seen in section 1.2, studies regarding the switching dynamics near the Curie temperature have been primarily focused on Fe-Pt alloys, including Fe-Pt-Cu nanomaterials [18]. Part of the reason for this is that Fe-Pt is the primary material candidate for HAMR systems, owing to its large K_{ui} and moderate T_c. However, most of the analyses performed were theoretical, and the theories that govern the switching dynamics are not unique, leading to different results [19]. Moreover, Fe-Pt nanomaterials used in HAMR systems have only been tested with 50% Fe and 50% Pt composition because stoichiometries outside of a 50-50 split between Fe and Pt have lower anisotropy values [3]. With such a tight constraint on the material's fractional composition, tuning the anisotropy and the Curie temperature becomes a very difficult task, providing less flexibility with regards to optimizing Fe-Pt-based HAMR systems. With the use of a more tunable material, more analyses regarding how anisotropy plays a role in the switching dynamics of HAMR systems can be performed.

The advantages of Co-Pt multilayers include: i) tunable multi-layered configurations, ii) grain sizes and ii) material compositions. As Co-Pt materials can be stable in a multi-layer configuration (not a natural configuration, which lowers the entropy of the system), the anisotropy of the material becomes easier to tune, making it possible to control many of the magnetic properties of the material. However, if the multilayered system is exposed to an excessive temperature, interlayer diffusion could take place and ruin the structure. The anisotropy of the material comes from the interaction between stacked layers, also known as the interfacial anisotropy, which is tuned by modifying the number of Co-Pt layers stacked on top of each other (see figure 1.7) [3]. The pressure of the deposition can also be controlled, which affects the granularity of the film (continuous films for low pressure vs. segregated grains for high pressure). By being able to tune the thickness, percentage composition and granularity of the Co-Pt multilayered system, it is possible to tune the Curie temperature, saturation magnetization, anisotropy and coercivity [5]. Tuning the coercivity of the material makes it possible to prevent switching at room temperature, as the magnetization needs to be stable for long-term data storage [4].

As there are many parameters to tune in a Co-Pt multilayer, not only is it necessary to use software that can model all the adjustable parameters, but it is also necessary to have accurate models of the switching dynamics, and how it changes as we increase and decrease the cooling rate around the Curie temperature (the HAMR writing process happens when the magnetization is “frozen” in an external magnetic field as the medium cools from a high temperature). Moreover, since studies regarding Fe-Pt have mainly been theoretical, the theory that best matches the experiment must also be chosen. In the longer term, the results of this work will allow us to compare the results of the theory as implemented in the VAMPIRE software to experiment, and validate the software’s ability to predict switching dynamics near the Curie temperature.

Within the remaining sections of this chapter, basic concepts of magnetism relevant to this work will be briefly reviewed, and the scope of the thesis will be outlined in the end of this chapter. The main results from this thesis state that there is a tradeoff between areal density and K_{ui} – a lower K_{ui} value implies a higher switching probability, but a lower areal density. As a result, there is not enough information to determine which shape and composition of magnetic media perform the best. My role for this thesis is to model the magnetic media found within our lab, and simulate a field cooling experiment to attain information regarding the blocking temperature and switching probability of each medium.

1.2: Literature Review

Regarding Fe-Pt-based nanomaterials, the primary candidate material for HAMR systems, theories of magnetization near T_c, along with the methods of modelling the switching dynamics near T_c, have been studied, albeit not as extensively. If the primary candidate has not been experimented with as extensively, then it is safe to say that not many studies have been performed on Co-Pt as well. Most of the switching models regarding Fe-Pt and Co-Pt-based nanomaterials have been heavily theoretical, and the magnetization dynamics vary drastically based on the model being used. This section will cover all of the major research around the switching models and dynamics of Co-Pt and Fe-Pt.

1.2.1: Theories of magnetization dynamics near T_c for Fe-Pt

Only three models have been used to model Fe-Pt nanoparticles: modified versions of the (1) Hamiltonian, (2) Heisenberg and (3) a multiscale model. According to a computational study performed by O. Hovorka et al., on Fe-Pt nanoparticles [3], the Curie temperature of the nanoparticles vary a lot on the size of the particle used and the model. Due to the lack of experimental data regarding the size-dependent critical behaviour of FePt near the Curie temperature, not enough parameters were available for more detailed models. In other words, not enough information regarding the behaviour of T_c, M_s and H_c at varying sizes is given. The reason for the lack of experimental studies on quantitative size dependences is due to the lack FePt nanoparticles available with varying sizes. Therefore, only two models were analyzed – (1) an FePt effective Hamiltonian with a long-range exchange (LE) term that was derived from density functional theory (DFT) calculations, and (2) a nearest neighbor (NE) exchange model that closely resembles the quantum Heisenberg model. Studies were only performed on 2 nm and 9 nm nanoparticles of FePt, and it is noted that the NE model $(746.5^{\circ}K)$ was closer to the experimental bulk Curie temperature value $(775^{\circ}K)$ than the LE model $(677.41^{\circ}K)$. Another study performed by A. Meo et al. [40], uses a multiscale approach, which is a combination between an atomistic and a macrocell model. The macrocell portion of the multiscale model ensures that simulations are not limited by computational requirements and lack of detail, while the atomistic portion of the model tries to parameterize the main properties of magnetic materials, such as the exchange coupling, magnetic anisotropy and damping constant. The magnetization behaviour was modelled by the Landau-Lifshitz-Bloch (LLB) equations, as opposed to a set of Hamiltonian or Heisenberg equations. A bulk Curie temperature of approximately $720^{\circ}K$ was obtained. Although a bit inaccurate in comparison to the NE model, the computation time is notably faster, and does not require as many parameters.

1.2.2: Theories of magnetization dynamics near T_c for Co-Pt

No theoretical models or computational simulations have been published regarding the magnetization dynamics near T_c for Co-Pt. However, with a study performed by R.F. Evans et al. [41], the magnetization dynamics of a single Co particle was analyzed near the Curie temperature. This study could be useful for extrapolating the magnetization dynamics of Co-Pt-based nanomaterials. A LE model was used – similar to that mentioned in section 1.9.1.

1.2.3: HAMR switching models for Fe-Pt

A theoretical and experimental study regarding the switching dynamics in HAMR systems was performed by Li, H et al. [42], and the switching probability of Fe-Pt for a given externally applied magnetic field was experimentally determined by analyzing the magnetization value through the Magneto-optical Kerr effect with the use of the pump-probe technique and comparing it to the saturation magnetization value of a given sample at a given temperature. The medium was heated up to a temperature above the Curie temperature of the sample, then cooled down to room temperature. What they observed was that a stronger laser pulse, a higher applied magnetic field value and peak laser temperature always results in a higher switching probability. Theoretically, they used the LLB equations to model the magnetization dynamics near the Curie temperature, and performed simulations to verify the results they obtained from experiments. A simulation performed by Nieves et al. [43], analyzes the magnetic field (produced with the use of the inverse Faraday effect) necessary to successfully switch a grain for a given granular Fe-Pt sample, and how it changes over time through a HAMR simulation. Another simulation performed by Zhu, J et al. [44], observed how the magnetic field required for switching varies with the magnetic field angle. They observed that an angle of 45 degrees minimizes the switching field. Additionally, they analyzed the thermal stability as a function of the grain size, the noise power as a function of the grain height, and visually modeled how the spin of each grain changes throughout a heat-assisted simulation. It seems that as the temperature decreases, the grains at the center of the sample tend to switch to the correct direction first, then the ones at the sides follow along, implying that surface effects may be present. It has also been observed that the noise power exponentially decreases as the grain height increases. For all of the 3 studies mentioned in this section, perpendicular $L1_0$ Fe-Pt grains are the only kinds of samples that have been analyzed within their studies.

1.2.4: HAMR switching models for Co-Pt

Experimental studies have not been performed with regards to the switching probability of Co-Pt. There is only one theoretical model, being the Arrhenius-Néel

Brown model developed by X.W. Wu et al. [45], but it is only limited to elongated Co-Pt grains within a high anisotropy medium, and they only test the switching probability for temperatures up to $500^{\circ}K$, which is well below the Curie temperature for a typical Co-Pt sample. According to a study done by X.W. Wu et al. [45], the switching probability can be modelled as a ratio between a sample's coercive field and field required to completely switch a material's spin direction. They used an Arrhenius-Néel Brown model for the coercivity of the Co-Pt samples of varying thicknesses they used.

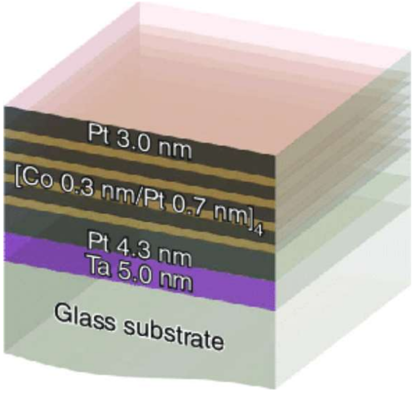

Fig. 1.7. Visualization of how the Co-Pt multilayer system is stacked together, and their thicknesses. Here, 4 repeats of a Co 0.3 nm/Pt 0.7 nm multilayer is shown, but these repeat units can number in the dozens for thicker multilayers. These layers are grown on top of a Glass-Ta 5 nm-Pt 4.3 nm layer that acts as substrate and texture layers to set the desired crystal orientation, and capped by a thicker protective Pt 3 nm layer to prevent corrosion [20]. In this visualization, only the layer structure is shown, and the granular nature of the film is omitted.

1.3: Anisotropy

With regards to magnetization dynamics in general, anisotropy refers to how the magnetization potential energy of a magnetic material varies as the magnetization points in different directions. In other words, the equilibrium magnetization is at a lower potential energy in some directions than others. These directions of lowest potential energy will be referred to as the anisotropy axes. Any deviations of the magnetization from these directions will lead to an energy penalty associated with changing the direction of the magnetic moment of the material [18]. The anisotropy field, H_k, is the external magnetic field that is required to rotate the spins of an anisotropic magnetic material from the anisotropy axis to the direction of highest potential energy. The units of magnetic anisotropy are typically in $\frac{erg}{cm^3}$ (magnetic anisotropy density in c.g.s units) or $\frac{J}{atom}$ (atomic anisotropy in S.I. units). This value will be specified as a single value rather than a tensor, as the most dominant form of anisotropy, also known as the uniaxial magnetocrystalline anisotropy value, is the only one that has been analyzed with Co-Pt-based nanomaterials [18].

1.3.1: Sources of Magnetic Anisotropy

Magnetic anisotropy can be induced in a variety of ways and they are expressed with several constants depend on their directionality and how they enter the equation for total magnetostatic energy. These constants are commonly tuned by: i) changing the shape of the material, ii) changing the material composition, iii) varying the interaction between layers of a film and iv) variation of a material's strain [21]. When modelling magnetic media with software, we will only focus on the most dominant anisotropy energy in Co-Pt multi-layers, which will be referred to as the uniaxial magnetocrystalline anisotropy constant (K_{ui}). This anisotropy is the result of the spin-orbit interaction of outer shell electrons in the crystal potential. For this computation, we chose the anisotropy direction to be in the z-direction, which is perpendicular to the thin film plane as in most Co-Pt multilayer samples [18, 21]. This is also the common anisotropy direction in modern recording media, which points perpendicular to the film plane [18, 21]. This uniaxial constant affects the coercivity of the easy axis hysteresis loop - more detail regarding this can be found in section 1.6 of this thesis.

1.3.2: Shape Anisotropy

The next most relevant form of anisotropy – also known as shape anisotropy, comes from the demagnetizing field (also known as the dipolar field) of a magnetic domain [18]. The demagnetizing field (the stray field outside a magnetic domain) acts to oppose the magnetic moment of a ferromagnet, and together, makes up the total magnetic flux density in a material [20]. The effective anisotropy field, $H_{k,eff}$ of a ferromagnetic domain can therefore be written as [22]:

$$H_{k,eff} = \frac{2K_{ui}}{M_s} - 4\pi N M_s \tag{1.1}$$

where M_s is the saturation magnetization and *N* is the demagnetizing shape factor. The first term on the right-hand side of the equation is the anisotropy field, H_k. The second term is the demagnetizing field due to shape anisotropy. Note that the factor of 4π comes from the use of c.g.s. units, which are historically more often used, and also used here in this text. $H_{k,eff}$ is the strength of an external magnetic field required to overcome shape and magnetocrystalline anisotropy effects [22]. The calculation of shape anisotropy effects in magnetic media is computationally expensive, as it requires an iterative approach to calculate the stay fields, updating the equilibrium magnetization of the medium, updating the stray fields based on the new magnetic configuration, and so on, until the magnetization converges. The computational cost increases due to the long-range effect (decay of statistical dependence as the time interval or spatial distance between adjacent points increases) [23] and the many-body nature (multiple interactions between many particles) of the problem. In this work, the effect of shape anisotropy is neglected to speed up computation – knowing that its effect, to a good degree of approximation (~0.1 T deduction in H_K), can be considered as an offset in the anisotropy field [24]. In other words, the magnetic media in practice will have a slightly larger anisotropy than the value used in computational analyses.

1.4: Exchange Energy Value

The exchange energy, also known as the exchange matrix or the exchange interaction value, refers to the occurrence whereby an individual magnetic spin will attempt to align adjacent magnetic spins within a material with itself [25]. Imagine that all spins are tied to each other with elastic bands - the thickness of the elastic band indicates how strong the exchange energy is, and the direction the elastic band turns indicates which spin direction dominates. Typically, the units are in joules (J), and the values are represented in the form of a matrix having J_{ij} elements – where each element represents a specific direction. Within ferromagnets, the magnetic spins have a tendency to align each other in a parallel fashion (the same direction) [26], which is why the anisotropy direction is usually in 1 direction. The reason why ferromagnets (Ex: iron, nickel and cobalt) are able to naturally align themselves in a parallel direction is due to their molecular band structure and spin distribution; for transition metals, the 3d orbital structure gets smaller as the number of protons starts to increase, meaning that the spins are forced to interact amongst themselves [26]. If there are an odd number of spins in the 3d orbital, then the magnetic field will not be cancelled out (for every "up" spin, there's a "down" spin that cancels it out). These two factors – contracting 3d orbitals and uneven spins, makes it easier for adjacent spins to co-operate with each other, as that consumes less energy than resisting each other [25, 26]. Therefore, adjusting the anisotropy, along with the 3d orbital structure and composition will affect the exchange energy [9]. The exchange interaction can also be negative, resulting in antiferromagnetic spin alignments (spins are aligned in opposite directions with respect to one another), but such interaction is not found in Co-Pt multi-layers.

1.5: Atomic Spin Moment

The atomic spin moment/value refers to how strongly the spins of a magnetic material can produce an external magnetic field. This moment is produced by the electrons within the atoms of a given material. For this thesis, the primary focus will be aimed towards thin-filmed materials. The shape of the electron orbitals, dimensions of the thin-film, and the intrinsic spin property of each electron within an atom affects the value of the spin moment of an atom [27]. Within a material, the total spin moment is affected by how the atoms are distributed within the material, along with the anisotropy and exchange interaction between adjacent spins. A visualization of the atomic spin moment, and where it fits in within a material can be seen in figure 1.8. As a nanomaterial has many atoms, the spin moment is typically averaged between each atom [27, 28]. The units are either in Bohr units (μ_B) or in $\frac{A}{m}$, whereas the magnetization of a material is often quoted in c.g.s units as emu/cc (electromagnetic units per cubic centimeter).

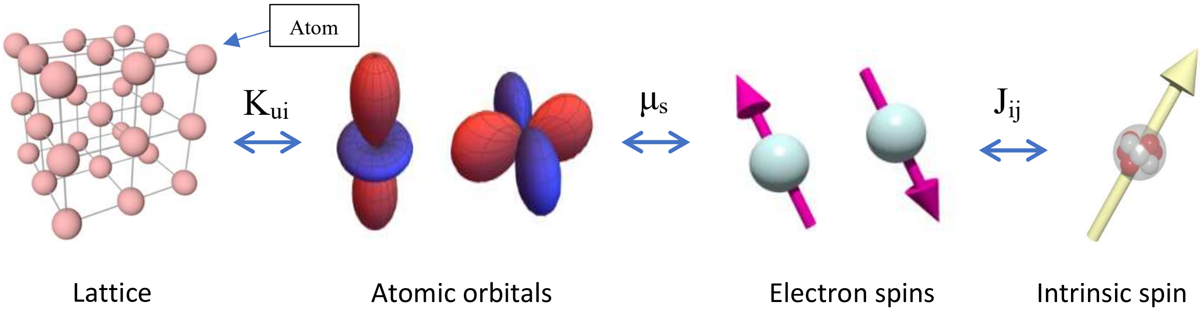

Fig. 1.8. A visualization of how all of the concepts mentioned in sections 1.2 - 1.4 are linked together. The atoms within a ferromagnet typically organized in a lattice-like formation [29].

1.6: Curie Temperature and Exchange Interaction Parameter

The Curie temperature (T_c), or Curie point – named after Pierre Curie, is the temperature at which materials lose their spontaneous magnetic properties [5]. For this experiment, only the Curie temperature of Co-Pt, which is a ferromagnetic material, will be analyzed. These spontaneous magnetic properties are in most part determined by exchange interactions within the material, which causes adjacent spins to be aligned within a magnetic domain (region within a material in which spins are uniformly aligned) [18]. As the temperature of a material increases, the magnetic exchange interaction competes against the thermal agitation within the material, resulting in the magnetization of domains to have a lower net value. Thermal agitation can also cause domains to move around, spin in random directions and reconfigure [18]. Once the Curie temperature has been reached, the spontaneous magnetization vanishes, together with the average size and orientation of magnetic domains [30]. The Curie temperature can be adjusted by adjusting the exchange interaction parameter (J_{ij}), which depends on the ratio of cobalt to platinum within the sample [20]. When performing simulations, the Curie temperature of Co-Pt samples will be matched to values found in the literature by adjusting the J_{ij} value. Afterwards, the normalized magnetization will be calculated using equation 1.2, then the values will be plotted with respect to temperature. Afterwards, Curve fitting with a typical Curie temperature curve that matches literature values will be done to find the Curie temperature, as seen in figure 1.9.

$$M_{normalized} = \frac{M(T)}{M(0^{\circ}K)} \tag{1.2}$$

$M(T)$ refers to the net magnetic moment at a given temperature, and $M(0^{\circ}K)$ represents the absolute maximum magnetic moment. The data is to fit the following relation obtained from the literature: $\frac{M(T)}{M(0^{\circ}K)} = (1 - \frac{\mathrm{T}}{\mathrm{T_C}})^{\beta}$, where β is a scaling parameter that is equal to $\frac{1}{3}$ for bulk 3-dimensional ferromagnets, and T_c is chosen in a way that best fits the data points. However, in practice, β can vary according to dimensionality in bulk systems, and is found to be lower in thin films and with surface effects (location of atoms on the surface of the material). Ideally, we do not want a Curie temperature that's too low or high. If the Curie temperature is too low, then the magnetization will be too unstable at room temperature (unpredictable spin direction behaviour) [30]. Alternatively, if the Curie temperature is too high, then it becomes too energetically expensive to write information in a hard disk drive due to the amount of thermal fluctuations that occur at higher temperatures. Additionally, if the Curie temperature is near the melting point of a nearby material in a HAMR system, then there are risks of melting the material when magnetic switching is performed [4]. Although there are benefits of increasing the Curie temperature – such as: increased areal density, larger temperature rises lead to larger temperature gradients on the disk and improved bit confinement, and faster read and write speeds (larger temperature gradients cool faster), acknowledging the drawbacks of increasing the Curie temperature is necessary. For the Co-Pt multilayer case, Curie temperature values are expected to be around $600°K - 800°K$ [13], which is significantly lower than the melting point of Co-Pt $(1200°K - 1400°K)$ [31], and comparable to the value of T_c of Fe-Pt used in HAMR media (~750 $°K$) [5].

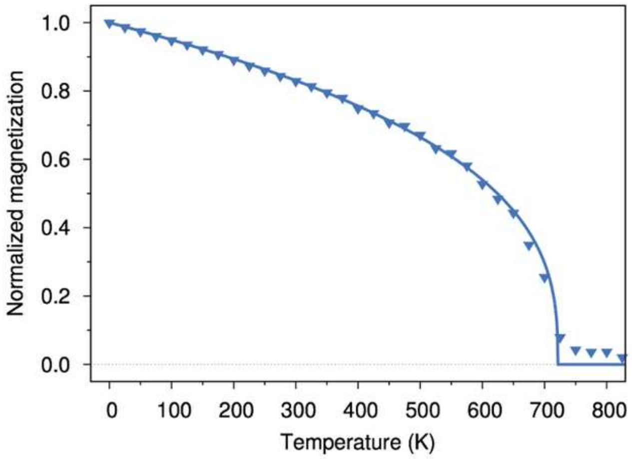

Fig. 1.9. Curie temperature curve produced by Vampire for a typical ferromagnetic material. The operating zone for switching occurs at around 710 to $730^{\circ}K$ [32].

1.7: Hysteresis

A hysteresis loop is a plot used for magnetic materials to show how its magnetization (M) depends on the external magnetic field (H). Since ferromagnetic materials with sufficient anisotropy will have a spontaneous magnetization without an applied field, and an applied field is needed to reverse the magnetization, more than one magnetization state may exist for a given applied field value, leading to hysteretic behaviour. In other words, the magnetization not only depends on the applied field, but also on the previous magnetization values. Since the magnetization is a vector in space, there are 3 orthogonal components of the total magnetization. Typically, a magnetization loop plots the component of the magnetization that is in the same direction of the applied magnetic field – if the magnetization is in the x-direction, but the loop is measured with a field applied in the *z*-direction, the value of the magnetization is zero (no component in the *z*-direction, although the total magnetization is not necessarily zero). Hysteresis curves also depend on the relative direction of the applied field with respect to the anisotropy axis of the magnetic material. There are two major types of hysteresis loops: i) hard and ii) easy hysteresis loops. Examples of these loops can be found in figures 1.10 and 1.11.

1.7.1: Easy axis hysteresis loops

To produce an easy axis hysteresis loop, the angle between the direction of the applied magnetic field and the anisotropy direction must be ~0° [33]. In other words, the applied magnetic field is parallel to the anisotropy direction, which means the magnetic field is being applied in the most energetically favourable magnetization direction. The word "easy" in "easy axis" refers to the axis along which the magnetization prefers to align, which is obtained by analyzing the magnetization direction at zero applied field below the Curie temperature (also known as the spontaneous magnetization of a sample). One purpose of analyzing easy axis loops is to obtain the coercivity, which is the magnetic field required to reverse the direction of the spontaneous magnetization of the material. This behaviour can be seen in figure 1.10. The coercivity is the result of a dynamic phenomenon where a given magnetization direction (stabilized by the anisotropy) is switched by destabilizing factors (such as thermal agitation and external field) [33]. It depends on many intrinsic and extrinsic factors, such as anisotropy, size of the nanoparticle (volume), temperature and how long the magnetic field is applied onto a material (magnetic residency). The coercive field values found in the literature can be indicative of the size of the magnetic particles at a given temperature, if the anisotropy is known [33].

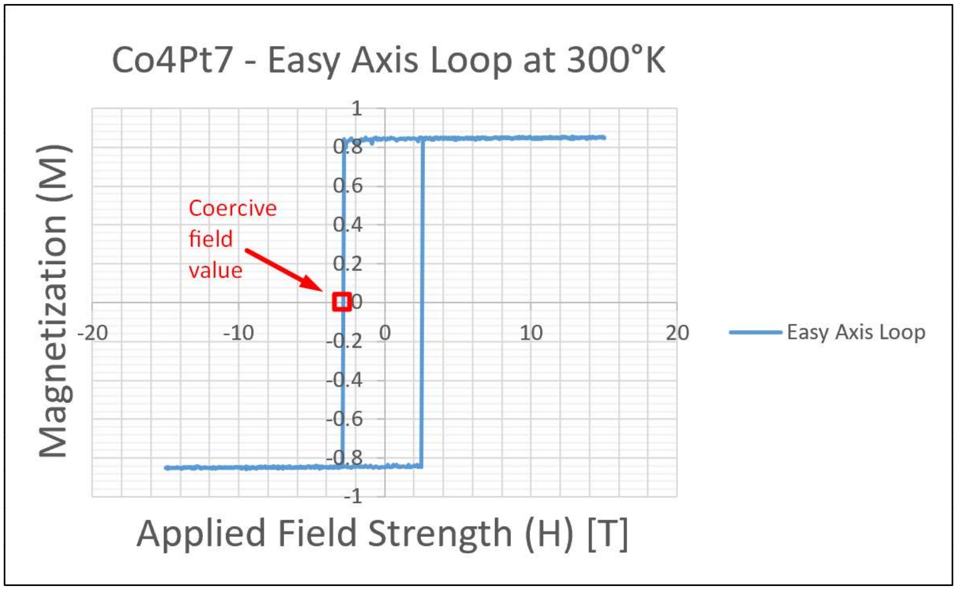

Fig. 1.10. An example of an easy axis hysteresis loop of bulk Co_4Pt_7 produced with the help of VAMPIRE. The H_c value (x-axis value) is taken from the value boxed in red. The left-most vertical branch represents the change in magnetization direction from the “up” to “down” direction, while the right-most vertical branch represents the opposite change in direction. The simulation starts at the top right corner, then the left-most vertical branch is the first branch that is taken. Once the bottom left most point has been reached, the right branch is taken.

1.7.2: Hard axis hysteresis loops

Contrary to the easy axis hysteresis loop, the hard axis hysteresis loop is obtained by applying the magnetic field at an angle of $\sim 90°$ with respect to the anisotropy axis [33]. In other words, the applied magnetic field is perpendicular to the anisotropy direction, which is the least energetically favourable direction for materials with uniaxial anisotropies. The word “hard” in “hard axis” refers to the direction along which the greatest external magnetic field is required to align the magnetization. The purpose of analyzing hard axis loops is to obtain the anisotropy field – the point at which the magnetization is completely turned along the hard direction by the external field and does not increase any further [34]. The magnetization at the anisotropy field value should match the magnetization value at the same temperature of a Curie temperature $\mathrm{M(T)}$ curve because when analyze the magnetization value at the applied strength value that matches the anisotropy field value (as seen in figure 1.11), the magnetization has been completely saturated in a given direction. In other words, the magnetization has reached the maximum possible alignment towards the hard axis direction. Regardless of whether a hard or easy axis loop is being analyzed, either loop shows how much of the magnetization aligns with the direction of applied magnetic field. The only difference is the direction that the magnetization is being compared to. The Curie temperature curve represents the total magnetization value in all directions that occurs at a given temperature. Therefore, it makes sense that the magnetization values must match. The anisotropy field value, which can be found in the literature, can be used to find the magnetocrystalline anisotropy constant of the material using eq. 1.1 [28].

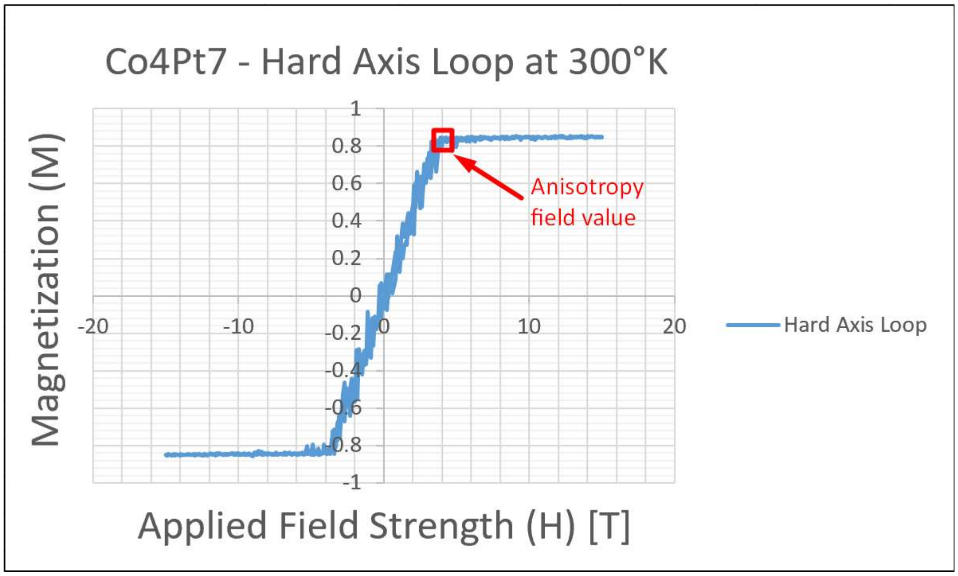

Fig. 1.11: An example of a hard axis hysteresis loop of bulk Co_4Pt_7 particle produced with the help of VAMPIRE. The anisotropy field ($H_{k,eff}$) value (x-axis value) is taken from the value boxed in red.

1.8: Blocking Temperatures

The blocking temperature of a nanomaterial is defined as the temperature at which the Néel relaxation time (τ_N) [35], which refers to the average time at which a nanoparticle's spin is prone to flip due to thermal fluctuations, is equal to the characteristic measurement time (τ_m) [35]. This is also known as the temperature at which the material transitions from a ferromagnetic to superparamagnetic state ($Case$ 1: $\tau_N = \tau_m$). The equation for both the relaxation time and the blocking temperature can be seen below for zero external applied field [35, 36]:

$$\tau_N = \tau_0 e^{\frac{K_{ui}V}{k_B T}} \tag{1.3}$$

$$T_B = \frac{K_{ui}V}{k_B \ln\left(\frac{\tau_m}{\tau_0}\right)} \tag{1.4}$$

τ_0 is referred to the attempt time and it represents the average time it takes for a spin within a material to scatter with another spin, K_{ui} represents the anisotropy energy and V represents the volume of the system [36]. When the system temperature is below T_B ($Case$ 2: $\tau_N < \tau_m$), a magnetic spin will be thermally stable, meaning that the measured magnetization will not change during the measurement time, τ_m. Above T_B ($Case$ 3: $\tau_N > \tau_m$), the thermal fluctuations are rapid to a point where the time-averaged magnetization reaches zero, even in the presence of an externally applied magnetic field [37]. As a result, a higher blocking temperature typically implies better thermal stability at higher temperatures, as the magnetization state is frozen for a longer period of time, meaning that the system is more robust towards larger thermal fluctuations. This implies that a transition between the original spin state and the "frozen" state occurs at a higher temperature. For field-cooling experiments, where the experiment starts at a very high temperature, this implies that the state gets frozen sooner, but that can also imply that not enough time is given for the spins to align themselves in a way that minimizes energy.

1.9: Magnetic Torque

Force between spins and an applied field are typically mediated through magnetic torque, which describes how strongly a magnetic spin reacts to the effective magnetic field it experiences. Writing into an HDD system happens when the average torque of the spins is at its highest point, as that is when the magnetization is in the process of changing its direction [38]. Torque is produced through the exchange interaction between the s and d orbitals of an atom; the magnetic field produced by the exchange interaction interacts with the applied magnetic field, which produces a torque on the atoms [39]. The torque is also limited by the dimensions of the nanomaterial; if the material is too large, then more torque is required to transfer enough torque to switch all of the atoms. However, if the material is too small, then the spins will rotate too rapidly, leading to more fluctuations that limit the transfer of information [39]. Therefore, an ideal thickness must be found. Magnetic torque is drastically affected by thermal fluctuations, dimensions of the material, and the angle at which an external magnetic field is applied (relative to the anisotropy axis of a material). The equation for magnetic torque can be seen below:

$$\boldsymbol{\tau}_{magnetic} = \boldsymbol{M} \times \boldsymbol{H}_k \tag{1.5}$$

$\boldsymbol{M}$ represents the magnetization of the sample, and $\boldsymbol{H}_k$ represents the anisotropy field of the sample. As torque is computed with the use of a cross product, the angle between the two vectors matters; therefore, the angle of the magnetic fields relative to a given direction is of importance. For all samples, the magnetic torque is computed by finding the cross product between the anisotropy field (which is the +z axis), and the coordinates of the average spin magnetization in each direction, then finding the magnitude of the vector produced from the cross product. For our case, the cross product produces the following vector: $M_y\hat{x} - M_x\hat{y}$, where M_x and M_y represent the magnetization in the x and y directions, respectively, and $\hat{x}$ and $\hat{y}$ represent unit vectors in the x and y direction. Therefore, the magnitude of the torque is $\left|\boldsymbol{\tau}_{magnetic}\right| = |\boldsymbol{H}|\sqrt{M_x^2 + M_y^2}$.

1.10: Chapter 1 Summary

The main purpose of this thesis is to create a virtual test bench with the use of VAMPIRE, and use it to analyze the factors that affect the switching probability of Co-Pt-based HAMR systems. As mentioned in the literature review (section 1.9), no experimental studies have been performed regarding the switching probability of Co-Pt nanomaterials, and given the range of experimental factors affecting the results, it is necessary to narrow all theories down to one model to reduce the variability of the results, or else the same modelling problem experience with Fe-Pt nanomaterials will be experienced. Therefore, this modeling framework will not only be able to test HAMR systems, but will also be able to predict the long-term usefulness of them. Furthermore, this work will provide a benchmark of the theory implemented by VAMPIRE so that it can be benchmarked against experiments to verify its accuracy in the experimental range (near T_c).

In this thesis, the uniaxial anisotropy value (K_{ui}), the exchange interaction value (J_{ij}), the atomic spin moment (μ_s) will be the material properties that will be modeled according to previous measurements from the literature, where the chemical composition of the material (% composition of Co and Pt in a Co-Pt multi-layer sample), along with the number of layers used within the thin film was varied. Once the bulk-like material properties are established, the behaviour of the thin granular film will be modeled, again driven by measured data, to simulate granular films with finite grain volume. Finally, HAMR writing processes will be modeled by measuring the switching probability as a function of several parameters. The parameters adjusted during the simulation are the magnitude of the applied magnetic field (H_{app}), the angle at which H_{app} is applied relative to the anisotropy axis, and the cooling rate. With the use of VAMPIRE, all of these material and simulation parameters will be adjusted in a way that maximizes the switching probability of the Co-Pt thin-film. The correctness of the predictions made by VAMPIRE regarding the Curie temperature graphs, hysteresis loops and switching probability will be analyzed by comparing them to trends and graphs found within literature and experimental values and studies.

This thesis is organized into six chapters. Chapter 1 provides a basic introduction and motivation for this work, HAMR systems and their applications, Co-Pt, anisotropy, exchange interactions, atomic spin moments, Curie temperature and hysteresis loops. Chapter 2 describes all of the experimental methods and approximations used to analyze thin films and Co-Pt nanoparticles, along with the detailed formulas and equations chosen to be used by the simulator, and the software being used. Chapter 3 covers the effective medium method for modelling Co-Pt atoms, and how to model the Curie temperature, coercivity and saturation magnetization for such atoms. Chapter 4 covers the Voronoi model for modelling Co-Pt-based thin-films, how to model the Curie temperature and coercivity in a way that matches experimental values. In chapter 5, the final experimental set-up, along with how each material and simulation parameter affects the switching probability will be analyzed, and 3-Dimensional graphs analyzing the factors affecting the switching probability, magnetic torque, blocking temperature and freeze time will be presented. Chapter 6 will conclude the thesis by summarizing all of the work performed, along with providing future directions for studies regarding switching probability analyses.

CHAPTER 2: COMPUTATIONAL TECHNIQUES

2.1 Overview

This section will discuss all the possible ways to computationally model Co-Pt nanomaterials. The three major things to consider are: i) how the spins are organized within the material, ii) the values to use for K_{ui}, μ_s and the exchange interaction constant (J_{ij}) based on literature values and our own samples, and iii) the software that can be used to put everything together. At the end of the section, a theoretical model will be chosen in accordance to the appropriate parameters in the literature, then imported into the software system of choice.

2.2 Approaches of obtaining the Co-Pt parameters

As there are multiple ways to arrange Co-Pt atoms within a crystal, decisions had to be made with regards to which structure to use. This section will discuss the different structure types and their relation to how magnetic spins are arranged. At the end of this section, a visualization of all the possible arrangements of Co-Pt will be shown in figure 2.1.

2.2.1 Ordered Alloys

Ordered alloys are composed of 2 or more types of atoms that alternate in a fixed pattern over a unit cell. Cobalt dilutions/insertions are placed into a lattice of platinum atoms [34]. To determine whether the alloy is ordered or not, the structure of the alloy is inspected for repeating patterns in the lattice as the cobalt to platinum ratio is altered. A simple example of an ordered alloy is one where Co and Pt atomic layers alternate within the FCC crystal lattice – the L10 ordered alloy. Due to the close proximity of the different types of atoms, the magnetic properties of a Co-Pt ordered alloy can be modelled together as a single atom in an FCC lattice that has the magnetic properties of the alloy as a whole (i.e. no magnetic variation from one atom to another). This results in a single value for J_{ij}. Depending on the ordering, the value can change quite dramatically.

2.2.2 Disordered Alloys

Disordered alloys are composed of 2 or more types of atoms that occupy random sites in a unit cell. The only difference between disordered and ordered alloy values are that no parameters are needed to describe the pattern (lattice structure). In other words, no restrictions are imposed on the alloy structure [34]. The value for J_{ij} varies continuously according to the proportion of Co and Pt atoms spanning the two bulk pure solid values, as long as the result is not an ordered alloy (i.e. the J_{ij} value is different for a 50% mix of Co and Pt, depending on whether they arranged in an ordered or disordered way). Figure 2.1 illustrates the structural differences between ordered and disordered alloys, along with multi layer systems.

2.2.3 Multi-layer

For a multi-layer, cobalt and platinum atoms are modelled as individual pure crystal layers as opposed to a cluster of atoms enclosed and arranged within a unit cell. Additional parameters are required to describe the number of layers the multilayer has, the thickness and composition of each layer, and how each layer interacts with each other (interfacial values) [34]. Typically, the J_{ij} values are provided as a matrix spanning all combinations of atomic interactions. Alternatively, an effective medium model (more details can be found in section 3.1) can be used to model these interfacial values, along with a macro-spin or atomistic approach. The effective medium model yields one J_{ij} value that is site-independent as in the case of alloys. Figure 2.1 illustrates the difference between the two types of alloys and a multilayer.

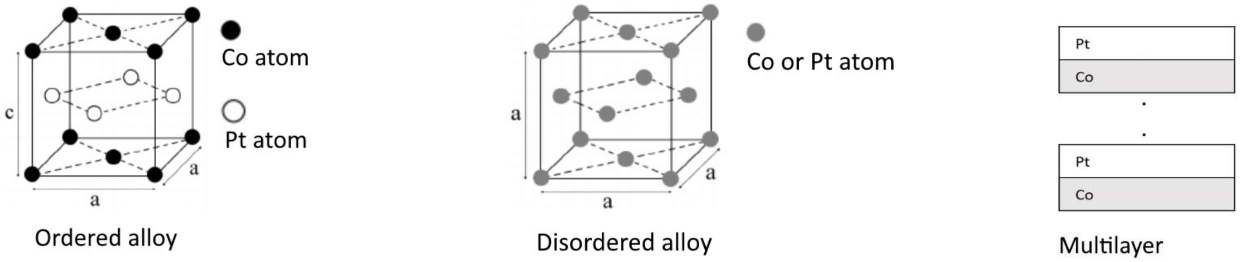

Ordered alloy

Disordered alloy

Multilayer

Fig. 2.1. A visualization of all the different ways of arranging Co and Pt atoms [46]. Note that for a multilayer, the sample doesn’t have to start and end with Co and Pt, respectively.

2.3 Approaches of modelling the magnetism of Co-Pt

For this work, there are two major ways of modelling the magnetism of nanoparticles – the atomistic and macro-spin approach. Both approaches use the same equations, but how the spins are interpreted – either on a per-atom level or one “macro-spin”, resulting in different output values. How the magnetic spin directions and magnitudes change over time determines the magnetic behaviour of nanomaterials, and can lead to other magnetic phenomena that happens at the nanoscale level. Both methods will be discussed, then compared and contrasted in this section.

2.3.1 Atomistic Approach

This approach – also known as the atomistic spin dynamics (ASD) model, uses the effective spin properties (moment, anisotropy, and exchange interaction) obtained from experiments or a DFT model, to model magnetic interactions on a per-atom basis. Thermal fluctuations of atomic spins are also taken into account. This approach originated with Ising in 1925 [47] – where the spins were analyzed in lattices with 2 dimensions. This model has been extended into 3-dimensions and includes quantum mechanical effects – yielding the Heisenberg model [47]. Now, thermal fluctuations have been added in unison with quantum mechanical effects. The equations used to model the behaviour of atomistic spins can be written as [48]:

$$\frac{\partial \boldsymbol{S}_i}{dt} = -\frac{\gamma_i}{(1+\lambda_i^2)}[(\boldsymbol{S}_i \times \boldsymbol{H}_i) + (\lambda_i \boldsymbol{S}_i \times (\boldsymbol{S}_i \times (\boldsymbol{H}_i)))] \tag{2.1}$$

$$\boldsymbol{H}_i = \boldsymbol{\xi}_i(t) - \frac{1}{\mu_{s,i}}\frac{\partial \widehat{H}}{\partial \boldsymbol{S}_i} \tag{2.2}$$

$$\widehat{H} = -\sum_{i<j} J_{ij} \boldsymbol{S}_i \cdot \boldsymbol{S}_j - \sum_i k_{ui}(\boldsymbol{S}_i \cdot \boldsymbol{e}_i)^2 - \sum_i \mu_{s,i} \boldsymbol{S}_i \cdot \boldsymbol{H}_{app} \tag{2.3}$$

These equations will be referred to as the stochastic LLG (sLLG) equations, and they characterize the precessional motion of spins in a given effective magnetic field. Equation 2.1 represents how the i'th atomistic spin, $\boldsymbol{S}_i$, changes over time, equation 2.2 represents how the i'th magnetic field at any given spin site is affected by $\boldsymbol{\xi}_i(t)$, also known as the time-dependent coloured noise thermal fluctuation function [49] (this models the irreversible exchange between thermal and electron spin fluctuations), and equation 2.3 represents the equation of the Hamiltonian in terms of the three major parameters mentioned in the beginning of this chapter (K_{ui}, μ_s, J_{ij}). $\boldsymbol{\xi}_i(t)$ is modelled as a Gaussian, and obeys Langevin's equation for Brownian motion [50]. For a given sample, the Hamiltonian for each atom (equation 2.3) is computed and added together. In the equations, λ_i, which is the damping factor for an atom, determines how strongly a spin wants to go back to its lowest energy position (parallel to the anisotropy axis). Also, γ_i, which is the gyromagnetic ratio for a given atomic spin, is the ratio of an atom's magnetic moment to its angular momentum. Additionally, $\mu_{s,i}$, which is the atomic spin moment of a given atom i, is the magnetic moment caused by the spin of electrons within an atom. The spin of protons, along with the spin-spin interaction between the electrons and the nucleus are ignored from these calculations, as the magnetic moments produced within the nuclei are typically too small [48]. $\boldsymbol{e}_i$ is a unit vector referring to the magnetic easy axis for a given site i. By solving those equations, the spin orientation of any atom at any given period of time can be found [47]. Section 2.4 of this thesis will discuss the approaches of solving equation (2.1). With this model, the exchange interaction is the strongest interaction by 2-4 orders of magnitude [51] and is responsible for determining how the atoms are aligned by each other. By looking at each atom individually, more details regarding the preferred anisotropy directions, intramolecular effects, thermal fluctuations and interlayer behaviour can be obtained [48]. This provides more insight about complex magnetic systems as they are more degrees of freedom that represent the magnetic material. However, a major disadvantage comes from how the material is discretized – if there are too many atoms/discretization steps, then it will take too long to run a simulation, and too much memory will be required to store a model of the material, making it computationally unfeasible.

2.3.2 Macro-spin approach

The macro-spin approach involves using a weighted averaging system to average out all the atom spin values obtained from the atomistic approach, then treating the nanoparticle system as it has one spin [52]. The majority of the spin's component will be in the direction of the easy axis, meaning that more weight is added towards that direction. This approach makes analyzing the magnetization dynamics of a magnetic medium easier and less resource exhaustive, saving a lot of computational time and memory. Additionally, this makes choosing the parameters used to model the nanoparticles a lot easier because fewer matrices are required, as there is only 1 spin value to care about. In a sense, the nanomaterial is treated as one atom [52]. However, by making such a broad approximation, more complex interactions such as those occurring in antiferromagnetic materials cannot be captured as there are fewer details regarding the individual spins of each atom. Additionally, this model does not work when the spin direction reverses through domain-wall switching [53]. Domain-walls are produced when certain areas of a magnetic material have a different spin orientation, leading through a boundary region with frustrated spin configurations. However, when the size of the particle is small compared to the size of domains separated by domain walls, one can assume that no domain wall exists and a macro-spin approach is justified.

2.4: Approaches of determining how the magnetic spins change over time

Both of the methods in this section use an iterative approach to solve the equations mentioned in section 2.3. Although both methods are iterative and recursive, both methods approach the problem of solving the equations differently by choosing the next point in a different way, moving to the next spin-state and how the initial spin states are chosen. Additionally, both methods have different restrictions on the magnetic spin states and field, along with different theoretical limitations – as both methods have different convergence requirements

2.4.1: LLG-Heun Method

The LLG-Heun method refers to using Heun's method to solve equations 2.1-2.3, which are a set of differential equations that define the magnetization dynamics at the nanoscale level [54]. Heun's method is a modified form of Euler's method – instead of using the tangent line of a given function at the beginning of a chosen interval as an estimate of the predicted direction of the next point, the tangent at both sides of a given interval are used, then averaged out [55]. Figure 2.2 shows a visualization of how the next step is chosen for the Euler and Heun method.

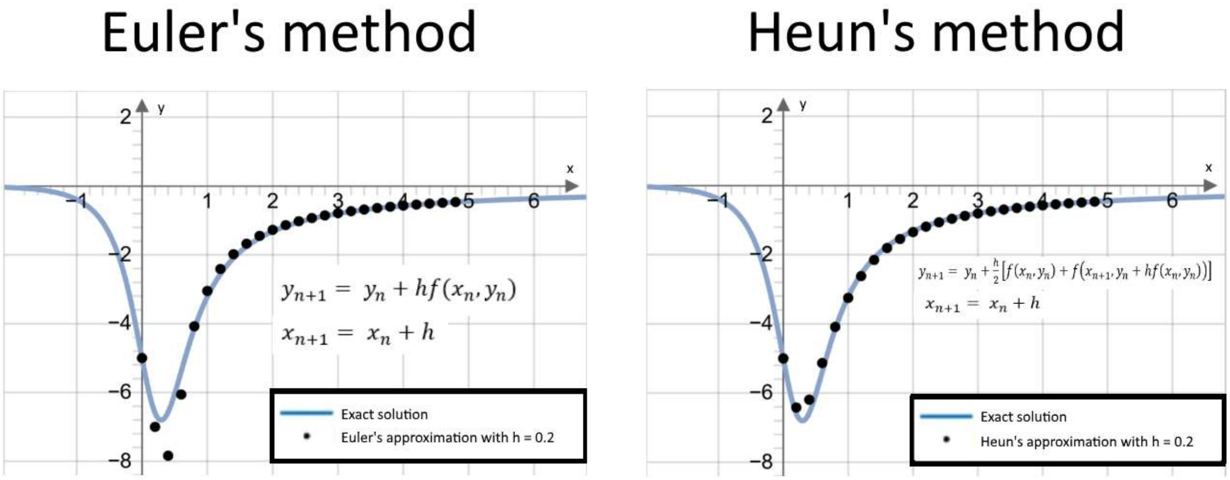

Fig 2.2. A comparison between the Euler's method and Heun's method on an arbitrary function, and how each step is chosen [56]. Note that $f(x, y) = \frac{dy}{dx}$. $'h'$ represents the step size of the approximation, which indicates the amount to increment the x and y values by for each n-th iteration.

In other words, this approximation takes two steps when computing the next point (also known as the two-staged Runge-Kutta method). Usually, the tangent to the left of the interval underestimates the next point, while the tangent to the right overestimates the other, which attempts to balance-out the error. Additionally, Euler's method assumes that smaller step sizes produces smaller errors, which is not true if the function's shape changes a lot, as seen in figure 2.2 [55]. Since small step sizes (h) require a lot of computation time, it is encouraged to use a large enough value for h (nothing less than 0.2), which means that errors add up at a faster rate.

With regards to magnetization dynamics, the spin directions over a given atom at any given position and time will be computed. Note that the definitions of $\boldsymbol{\xi}_i(t)$, λ_i and γ_i can be found in section 2.3.1. $\boldsymbol{\xi}_i(t)$ changes at each time-step for each position i. The first step involves choosing an initial spin direction at a given position i, $\boldsymbol{S}_i$, and settings for the effective field acting on that point, $\boldsymbol{H}_{eff}^{i}$. A fixed time-step, Δt, is also chosen. The next step involves calculating the spin direction at the next position, $\boldsymbol{S}_i'$, based on $\Delta\boldsymbol{S}$, which represents the direction at which the prediction of the next spin state, $\boldsymbol{S}_i'$, should be for the same effective field stated in the initial conditions by performing a standard Euler integration step, which can be seen as [54]:

$$\boldsymbol{S}_i' = \boldsymbol{S}_i + \Delta\boldsymbol{S}\Delta t \tag{2.4}$$

$$\Delta\boldsymbol{S} = -\frac{\gamma_i}{(1+\lambda_i^2)}[(\boldsymbol{S}_i \times \boldsymbol{H}_{eff}^{i}) + (\lambda_i\boldsymbol{S}_i \times (\boldsymbol{S}_i \times \boldsymbol{H}_{eff}^{i}))] \tag{2.5}$$

$$\boldsymbol{H}_{eff}^{i} = \boldsymbol{\xi}_i(t) - \frac{1}{\mu_{s,i}}\frac{\partial\hat{H}}{\partial\boldsymbol{S}_i} \tag{2.6}$$

After each iteration, the revised effective field, $\boldsymbol{H}_{eff}^{i\prime}$, has to be computed, as the field changes over a given time step Δt. This procedure is repeated until all of the spins directions have been initialized. Afterwards, all of the vectors are re-normalized, and their changes are analyzed over equally spaced time-steps, Δt. The spin position at the next time-step at a given position i, $\boldsymbol{S}_i^{t+\Delta t}$, is computed by performing a second-order Runge-Kutta approximation (also known as Heun's method), which can be seen as [54]:

$$\boldsymbol{S}_i^{t+\Delta t} = \boldsymbol{S}_i^t + \frac{1}{2}(\Delta\boldsymbol{S}_i + \Delta\boldsymbol{S}_i')\Delta t \tag{2.7}$$

$$\Delta\boldsymbol{S}_i' = -\frac{\gamma_i}{(1+\lambda_i^2)}[(\boldsymbol{S}_i' \times \boldsymbol{H}_{eff}^{i'}) + (\lambda_i\boldsymbol{S}_i' \times (\boldsymbol{S}_i' \times \boldsymbol{H}_{eff}^{i'}))] \tag{2.8}$$

$\boldsymbol{S}_i^t$ represents the spin of the i^{th} spin at a given time, *t,* and $\Delta\boldsymbol{S}_i'$ represents the prediction of the direction at which the spin state after $\boldsymbol{S}_i'$ should be. The above equation is repeated for each position i, then a time-step is taken. The "interval" here is the size of the time-step. Note that each spin vector is normalized to ensure numerical stability and convergence to the solutions shown in the set of equations at the end of this section (also known as the Stratanovich solution set for cartesian coordinates) [57]. Typical values for time-step lengths are $\Delta t = 10^{-15}\ s$. The reason why a time-step length of 1 fs is chosen is due to the existence of a time correlation between the thermal and magnetic spin fluctuations that occur at the nanoscale level, which typically occur in the order of 10 fs [58]. As a result, thermal fluctuations can no longer be modelled as white noise (the noise is now "coloured"), as white noise cannot model the exchange between thermal and magnetic spin fluctuations in accordance to the fluctuation dissipation theorem. Therefore, a timescale of 1 fs is reasonable for capturing such effects. For materials with a higher Curie temperature, smaller time steps (typically 0.1 fs) are necessary due to the decreased correlation times between thermal and magnetic spin fluctuations which result from stronger thermal fluctuations at higher temperatures [57]. For the simplest case, where the damping factor (λ_i) is set to 0.1 (small enough, so that processional effects are included, but will not continue indefinitely), and thermal fluctuations are ignored, the error is computed by finding the difference between the computed spin values (equations 2.8 to 2.9) to the ideal spin values (equations 2.10 to 2.12, inclusive) for each time, t, then computing the average error for each time [57]. The simulation stops once convergence to a solution set is reached (no change in solutions between two time-steps). The error was computed to be as low as 10^{-6}, which is a very promising result [57]. The ideal equations, for the spin in each direction, at a given time, t, for each position, i, can be shown as [57]:

$$\boldsymbol{S}_x(t) = \operatorname{sech}\left(\frac{\lambda\gamma H}{1+\lambda^2} t\right) \cos\left(\frac{\gamma H}{1+\lambda^2} t\right) \tag{2.9}$$

$$\boldsymbol{S}_y(t) = \operatorname{sech}\left(\frac{\lambda\gamma H}{1+\lambda^2} t\right) \sin\left(\frac{\gamma H}{1+\lambda^2} t\right) \tag{2.10}$$

$$\boldsymbol{S}_z(t) = \tanh\left(\frac{\lambda\gamma H}{1+\lambda^2} t\right) \tag{2.11}$$

2.4.2: Monte-Carlo heuristic method

The Monte-Carlo method works by simulating all the ranges of possible outcomes for an event that is uncertain in nature. In this case, the spin states change randomly due to thermal fluctuations [59]. A probability distribution is chosen for a given set of variables, then the value of each variable at a given time is computed many times until the variable converges to a certain value.

To start, a random spin direction of a given atom, i, is chosen ($\boldsymbol{S}_i$), then the spin changes to a new random direction ($\boldsymbol{S}_i'$). The change in energy ($\Delta E = E(\boldsymbol{S}_i') - E(\boldsymbol{S}_i)$) required by the system to change the direction of the spin is calculated, then this move is accepted with probability $P = e^{(-\frac{\Delta E}{k_b T})}$, where T is the temperature of the system [60]. This procedure is repeated for each spin *N* times, where *N* is the number of atoms in a given system. In order for a spin state transition to be acceptable, the change must be reversible and theoretically possible to attain (ergodic) [57]. To ensure that these two conditions (reversibility and ergodicity) are satisfied, the spin is assumed to have a gaussian distribution, and the spin magnitudes and directions are restricted along a unit sphere. This ensures that the simulation results are realistic, and lower in error because if the solution is stuck in a state where the change in energy is not optimal, the simulator can always re-trace its steps to fix this issue.

The error is computed in the same way as the LLG-Heun case, and the results seem to align with the same degree of accuracy as the LLG-Heun case.

However, there are some drawbacks with this method, which will be mentioned in the next section [57].

2.4.3: Comparison between the two methods

In terms of convergence speed, the Monte-Carlo algorithm is up to 10 times faster than the LLG-Heun method. However, as Monte-Carlo systems are very difficult to parallelize, the efficiency of the Monte-Carlo method starts to decrease as the system size increases [61]. Therefore, once the system size exceeds 10 nm x 10 nm x 10 nm, it is best to use the LLG-Heun method for computing the spin directions and magnitudes of the system [57]. Additionally, unlike the Monte-Carlo method, the LLG-Heun method uses educated guesses based on the theories behind spin dynamics to predict the next spin state instead of a randomized set of trials to choose the next state. This makes it easier to understand why and how the spins change over time. Moreover, in the Monte-Carlo case, the spin states are forced to follow a specific probability distribution, leading to a bias in the results produced. This helps with finding patterns in error and convergence, making the results more reasonable. The damping factor and the time step are tunable with the LLG-Heun method, making it easier to adjust the computation time and accuracy. Overall, if the system size is smaller than 10 nm x 10 nm x 10nm, and damping effects are negligible, then the Monte-Carlo simulator is the best choice as the simulations are performed at a faster rate, while maintaining the same accuracy as the LLG-Heun simulator [57]. Otherwise, the LLG-Heun simulator is a better choice, as not only is this simulator easier to parallelize, but convergence is easier to attain as the size of the system gets larger due to the non-randomized nature of the simulation. Performing random trials, and assuming the spins states to distribute themselves in a Gaussian manner is very unreasonable when the system size gets larger because of thermal fluctuations; the energy of the system increases as the system size gets larger, meaning that there are a lot more energy configurations to take into account [62]. Additionally, there will also be more thermal fluctuations as the number of atoms increases, meaning that the simulations will become more randomized and time-consuming, as there is not a reasonable, theoretical approach that is being followed. Therefore, careful considerations regarding the choice of the initial spin states, energy system, and how the next spin state is chosen is necessary for producing accurate and reasonable results in a timely manner. As a result, the LLG-Heun simulator was chosen over the Monte-Carlo simulator, as this simulator is easier to parallelize, and calculations are performed in a non-randomized manner, which minimizes computation time and approximation errors as the system size increases.

2.5: Methods of computing the dipolar field

As mentioned in section 1.2.2, computing the demagnetizing field is a computationally expensive procedure that can drastically affect the simulation results. More specifically, the average case performance of each method is proportional to ${N_{cells}}^2$, where N_{cells} represents the number of "cells" (see figure 2.3 for a visualization) in the thin film [60]. Therefore, careful considerations must be made when choosing how to interpret and calculate the cells, which will alter the effects of the dipolar field on the switching probability. A major trade-off between computation time and accuracy has to be made; each sub-section after 4.3.1 represents a method that attempts to balance both aspects as evenly as possible [63]. The atomistic approach is the most fundamental method of computing and analyzing demagnetizing affects found within nanomaterials – the macrocell and tensor approach work by modifying the equations used in the atomistic approach in attempts to increase computation speed, while trying to maintain the same accuracy as the atomistic approach.

2.5.1: Atomistic approach

Although the atomistic approach produces the most accurate results, it has the slowest computation time. To begin, the demagnetizing tensor, also known as the dipolar tensor, is computed between each atom and every other atom in the system. Afterwards, the dot product between the demagnetizing tensor and the magnetization vector of the system is computed [60]. These two steps are repeated every time for each atom within the system whenever the system temperature or the magnitude of the applied magnetic field changes. This will be referred to as the demagnetizing field of the system. The equations for the demagnetizing field and tensor can be seen as [60]:

$$N = N_{dipole-dipo} - N_{self} = \frac{\mu_o}{4\pi}\left(\sum_{p \neq q} \frac{3(\boldsymbol{m}_{mc}^{q} \cdot \hat{\boldsymbol{r}}) \cdot \hat{\boldsymbol{r}} - \boldsymbol{m}_{mc}^{q}}{r^3}\right) - \frac{\mu_o}{3} \frac{\boldsymbol{m}_{mc}^{p}}{V_{mc}^{p}} \tag{2.12}$$

$$\boldsymbol{H}_{Demagnetizing} = -N \cdot \boldsymbol{m} \tag{2.13}$$

Where N represents the demagnetizing tensor, $\boldsymbol{m}$ represents the magnetization vector of the entire system, μ_o represents the permeability of free space, r represents the distance between two atoms in a system, $\boldsymbol{m}_{mc}^{q}$ represents the magnetization vector of the atom q (other atom) in a given macrocell (more detail in section 4.3.2), $\boldsymbol{m}_{mc}^{p}$ represents the magnetization vector of the atom p (the atom of focus) in a given multicell, and V_{mc}^{p} represents the volume of the macrocell surrounding a given atom p. The demagnetizing tensor can be split into two terms; (1) $N_{dipole-dipol}$ represents the contribution towards the demagnetizing tensor from other atoms, while (2) N_{self} represents the atom's contribution towards its own demagnetizing field [64]. As seen in the equation for N, the dipole fields are proportional to $\frac{1}{r^3}$, meaning that dipole field effects can be experienced at a very long range. In other words, atoms that are very far away from the atom whose dot product is being computed with will still greatly contribute to the demagnetizing effect, as the exchange interaction is proportional to e^{-r}, which decays faster than

$\frac{1}{r^3}$ at larger distances [65]. Although the exchange interaction is more dominant between atoms closer to each other, the demagnetizing effects are more dominant as the atoms start to get farther away from the atom of focus. Therefore, as the system size starts increasing past 10 nm x 10 nm x 10 nm, this effect starts to take up a majority of the computation time [57]. Due to this consideration, the calculation of dipole fields are very expensive, and cannot be ignored, meaning that new methods are required in order to make simulations computationally feasible, even if it means sacrificing a bit of accuracy.

2.5.2: Macrocell approach

For this approach, the entire system is broken up into macro-cells of a given size that is smaller than the system size [60]. A visualization of the macrocell approach can be seen in figure 2.3. Afterwards, the magnetization of each atom is averaged out within a given cell, and the same calculations in section 2.5.1 are performed. The only difference between the atomistic and the macrocell approach are how V_{mc}^{p} and r are computed - V_{mc}^{p} is the volume of the macrocell instead of the atom, and r is the distance between the centers of two macrocells [57]. This increases computation time by reducing the effective number of atoms; instead of repeating the calculations for every atom, the calculations are repeated for the macrocells, which are lower in quantity. Therefore, the summation term shortens drastically, meaning that fewer computations have to be made. However, the accuracy starts to reduce because not every atom within a macrocell will behave the same [57]. In other words, this method cannot be used when analyzing complex magnetic structures such as domain walls and interlayer effects.

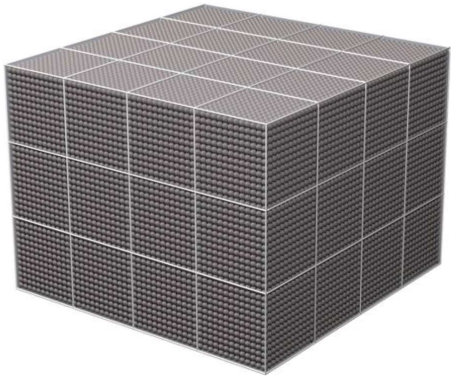

Fig. 2.3. A visualization of how a system is broken down into macrocellular cubes. Note: the atoms will not always arrange themselves in a perfect rectangular prism; therefore, some macrocells might have more atoms within it than others [60].

2.5.3: Tensor approach

The tensor approach is an upgrade from the macrocell approach in the sense that the accuracy of the demagnetization field is improved by adding a cut-off radius [60]. A visualization of this method can be seen in figure 2.4. Each small arrow represents the spin of an atom, while the larger arrow represents the spin of the macrocell. Within a certain cut-off radius from an atom, the neighbors of the atom are treated like atoms. Neighbors outside this radius are treated like macrocells [57]. Therefore, two different interpretations of the equations mentioned in section 2.5.1 are used here; if the macrocell touches the cut-off radius, or is inside the circle produced by the radius of that spin, the atomistic interpretation is used to compute the demagnetizing effects of those atoms [65]. However, if the dipole effects are computed with atoms that are contained within macrocells that are not inside or touching the edge of the circle, then the macrocell interpretation is used to compute the demagnetizing field between those two atoms [57]. The major difference between the approaches is the volume and the distance between atoms and macrocells, and how they're computed. Although the computation time increases exponentially (worst case: N^2, where N = number of atoms), the results become more accurate, as the effects of the atoms that are closest to the atom are considered in more detail. This is of importance because as mentioned in section 2.5.1, the dipolar effects start to dominate over the exchange interaction at greater distances with respect to a given atom. However, since interlayer effects and domain walls are excluded from our model, it is not necessary to drastically exponentially increase our computing time for a small increase in accuracy. In section 2.5.4, three easy and hard-axis hysteresis loop simulations will be ran for an arbitrary Co-Pt sample in our lab – (1) without dipolar effects, (2) macrocell approach, and (3) tensor approach, then these three loops will be compared in figures 2.5 and 2.6. Due to how oversimplified our model is, it might not be necessary to even include dipolar effects.

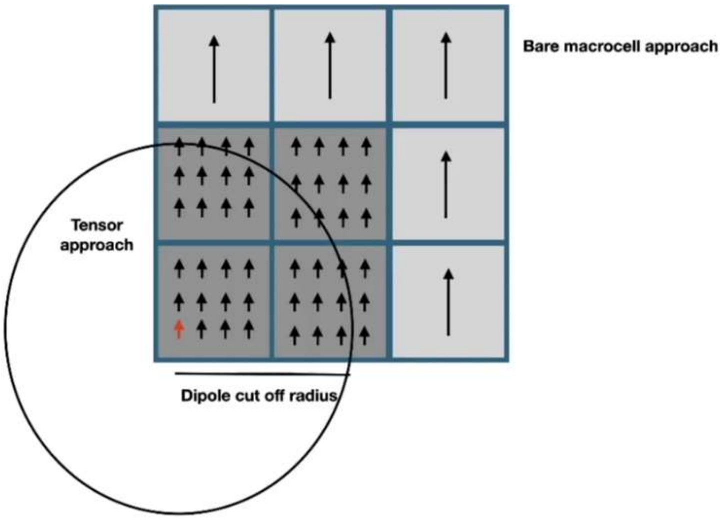

Fig 2.4. A visualization of how VAMPIRE interprets the system with the tensor approach to modelling demagnetization effects at the nanoscale level [60].

2.5.4: Analysis of dipolar effects with VAMPIRE

From looking at figures 2.5 and 2.6, the changes in coercivity and anisotropy field due to dipolar effects are negligible for all three methods. Additionally, when looking at table 2.1, the memory requirements for the macrocell and tensor method are 160 and 355 times higher than a normal simulation, respectively, and the macrocell and tensor simulations take longer than a simulation ignoring dipolar effects, it is best to ignore dipolar effects, as one of the major requirements of this framework is to be memory and computationally efficient. For a 60 nm x 60 nm x 3.3 nm thin-film, a macro-cell size of 2 nm x 2 nm x 2 nm, a dipolar field update rate of 1000 time-steps, and a cut-off radius of 2 nm (tensor approach only) was chosen. The model of only one of the four samples in our lab was tested because the structure of each sample was modelled in a similar fashion – the only thing that differs are the stoichiometries of cobalt and platinum within the sample, along with the values for μ_s, T_c and K_{ui}. Additionally, the easy and hard axis hysteresis loops (see section 1.6 for more detail) were only tested at 300°K, as our lab only has hysteresis loops at this temperature, making those loops our only reference. Overall, dipolar effects will not affect the switching probability as much, as they do not affect the hysteresis loop values as much.

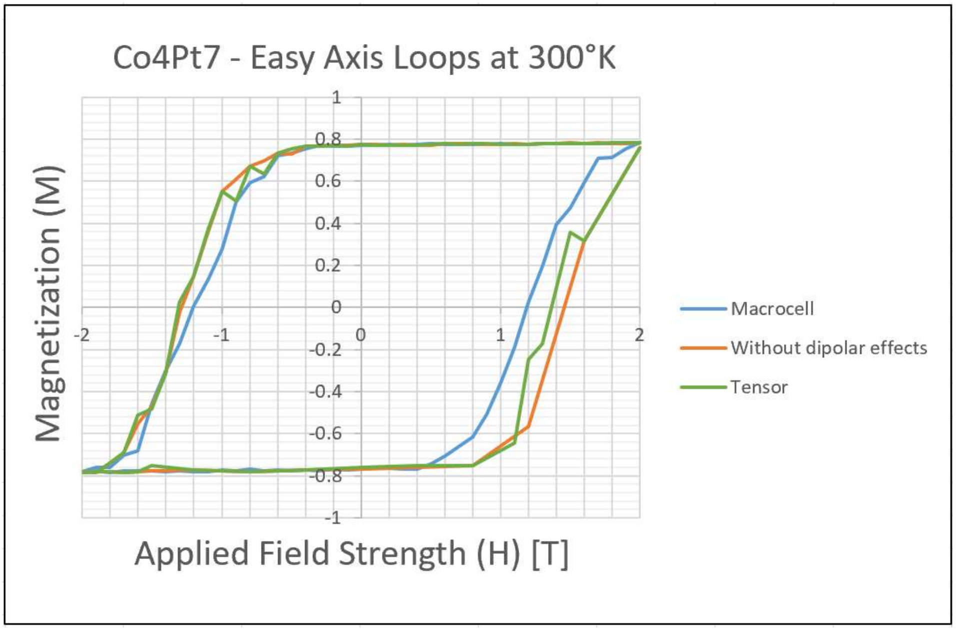

Fig 2.5. Comparison of the easy-axis hysteresis loops with and without dipolar effects for a single particle of Co_4Pt_7.

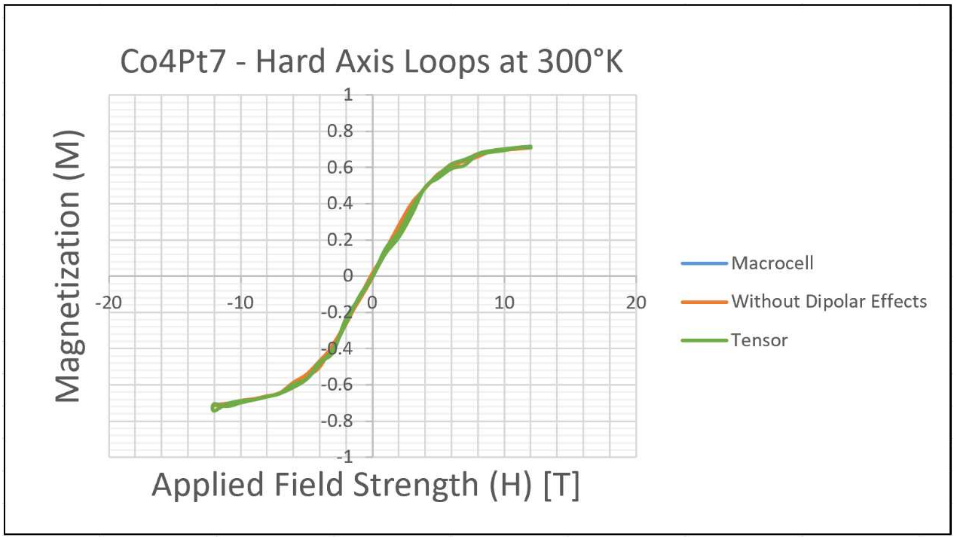

Fig 2.6. Comparison of the hard-axis hysteresis loops with and without dipolar effects for a single particle of Co_4Pt_7.

Table 2.1: Comparison of the performance requirements between the three kinds of dipolar simulations. For each simulation, 64 CPU's/cores were used, and the simulation was split into 16 processes. Note that the hard and easy axis loop simulations took nearly the same time to run.

Dipolar effects	**Memory required**	**Simulation time (s)**
N/A	256 MB	87300
Macrocell	42 GB	142212
Tensor	91 GB	213140

2.6: Structural formations of Co-Pt thin-films

The structure of the thin-film affects the total magnetization of the film by adjusting the boundary conditions of each spin, changing how the thermal energy is distributed across the medium, and re-distributing the dipolar field in a different manner. Additionally, different dipole sizes and cut-off radii have to be used if the shape changes, as the number of atoms that interact with the boundary will change as the shape of the boundary changes [34]. As a result, the switching probability is dependent on the shape of the material because if the distribution of atoms changes, then the magnetic spins will behave different, meaning that the total magnetization changes [66].

2.6.1: The Co-Pt multi-layer structure

A multi-layer is a structure composed of layers of two or more materials that repeat in a periodic manner. In order to build a multi-layer, the layers must be grown on top of each other in a way that their atomic lattice structures match. Co-Pt multilayers are in essence a superlattice, but modeling each Co and Pt layer independently would require accurate knowledge of the exchange interactions between Co and Pt. In this work, the atoms will be modelled as a weighted combination of cobalt and platinum, then the atoms will be repeated in a periodic arrangement. In essence, the model uses a fictitious atom in a crystal that averages out the lattice and magnetic properties of the Co and Pt atoms in the multilayer. An FCC unit cell will be used to model the multi-layer structures of Co and Pt, as that is how Co-Pt atoms are deposited [67]. A visualization of this FCC unit cell structure can be seen in figure 2.7. As mentioned in the introduction, this approach will be used to obtain the correct values of μ_s, T_c and K_{ui}, as a majority of the literature studied Co-Pt thin films in their superlattice form [67]. However, when modelling thin-films, it's best to use a more realistic model to illustrate the distribution of atoms, as a perfect crystal does not have the granular structure found in thin films. The best way to approximate such structures is to use the Voronoi approach, which will be introduced in the next section.

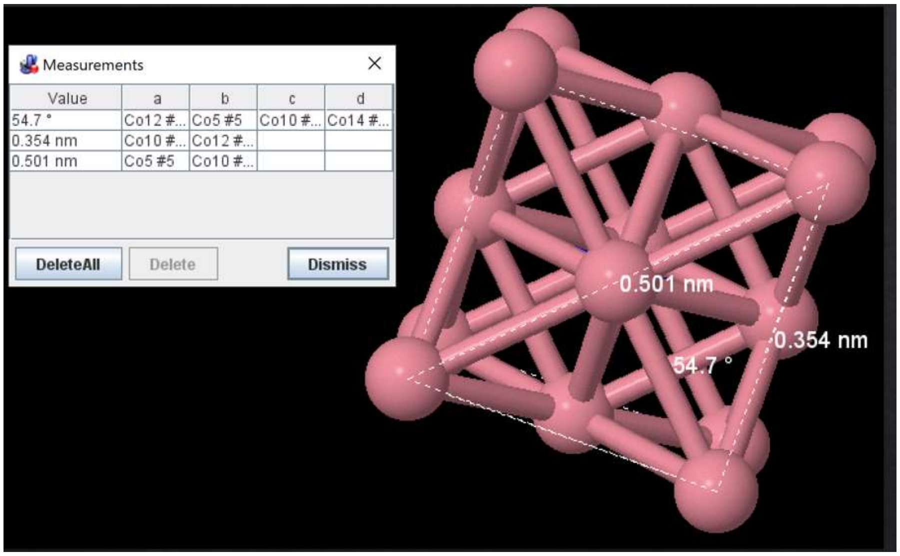

Value	a	b	c	d
54.7 °	Co12 #...	Co5 #5	Co10 #...	Co14 #...
0.354 nm	Co10 #...	Co12 #...		
0.501 nm	Co5 #5	Co10 #...		

Fig 2.7. A visualization of a 0.5 nm x 0.5 nm x 0.5 nm FCC structure with the use of jmol, an open-source Java viewer for chemical structures in 3D.

2.6.2: Voronoi approach

The Voronoi approach originates from Voronoi diagrams, which are also referred to as: Dirichlet tessellations or Thiessen polygons [68]. It is a way to fill a space in a way that resembles the natural nucleation and growth of crystals in a thin film. Let's assume that N points of references are scattered along a k-dimensional space [69]. The main goal now is to enclose each point within a polygon in a way that ensures each vertex that makes up the polygon is closer to the point enclosed within the polygon than any other point of reference within the entire k-dimensional space. This can be mathematically represented by the following equations [70]:

$$Vor(S) = \bigcup_{i=1}^{N} Vor(s_i) \tag{2.14}$$

$$Vor(s_i) = \{q: dist(s_i, q) \leq dist(s_j, q)\ for\ i \neq j, s_j \in S\} \tag{2.15}$$

$$dist(s,q) = \sqrt{(s_1 - q_1)^2 + (s_2 - q_2)^2 + \cdots + (s_k - q_k)^2} \tag{2.16}$$

Let S be a set of reference points, $\{s_1,\ s_2 \ldots, s_N\}$, where $2 < N < \infty$. N represents the number of points in set P. Let q be the set of vertices that encloses a given reference point s_i. Each point, s and q have coordinates $(s_1, s_2, \ldots, s_k)$ and $(q_1, q_2, \ldots, q_k)$, respectively, where $2 < k < \infty$. By finding the union of all the polygons, this encloses the entire space with Voronoi polygons surrounding each reference point. Geometrically, this can be done by drawing lines that attach all of the points of reference, then finding the perpendicular bisector for each line in the diagram [69]. Afterwards, the perpendicular bisector lines are extended until the boundaries of the space have been reached, and all the intersections between the perpendicular bisectors are attached together with lines [69]. By attaching the intersection points of each perpendicular bisector, the desired polygons have been made. A visualization of this procedure is shown in figure 2.8. Voronoi structures will be used to model the Co-Pt thin film structure, as this is how thin-films organize themselves [71]. In this work, each point represents a Co-Pt grain, which is a cylindrical arrangement of atoms. Each grain has a varying surface roughness and volume. In other words, not all grains will be perfect cylinders with the same volume. The amount of grains is dependent on the size of the average grain and the system space, which is what the user controls. Grains are added until the size of the polygons surrounding each grain is minimized. The centroid of each grain will be used to produce the Voronoi diagram [72]. This is a more realistic model of how Co-Pt thin-film structures are made – cobalt and platinum atoms are sputtered in sequence onto a substrate, and the deposition rate and system pressure determines how the atoms will re-arrange. It turns out that as the multi-layer grows, each grain can be separated from its neighbors and they naturally take on a rough cylindrical shape filling 2-dimensional space – akin to a Voronoi film. A visualization of this structure with jmol can be seen in figure 2.9.

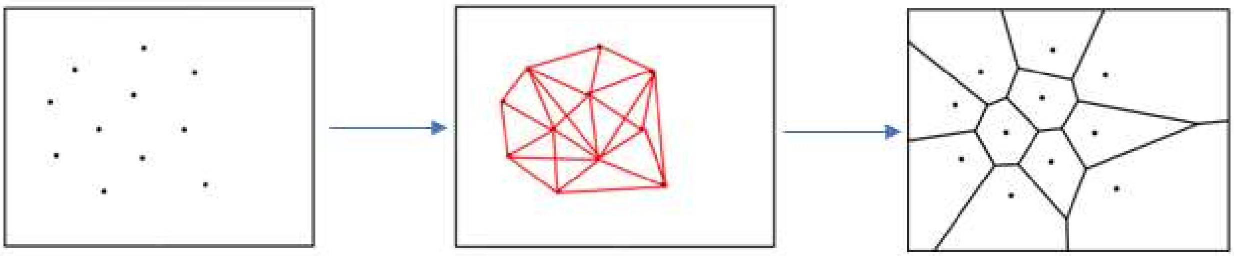

Fig 2.8. A visualization of how a Voronoi diagram is produced for a set of 11 points/grains within a 2-dimensional space [69].

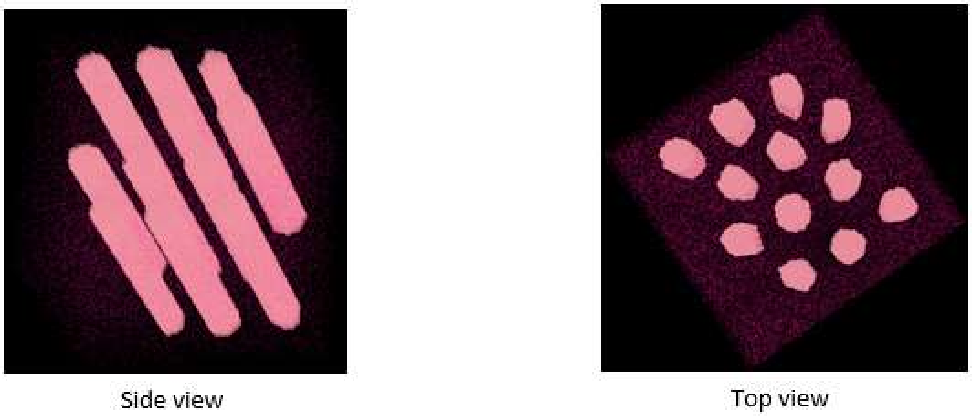

Fig 2.9. Visualization of 2.7 nm diameter grains (12 grains) distributed along a 20 nm x 20 nm x 18 nm space with the use of jmol. The atoms surrounding the grains are non-magnetic atoms that were added to ensure every computing process contained atoms (a requirement of the VAMPIRE software when the simulation process is parallelized). The magnetic spin of each atom is averaged to one value.

2.7 Ultrafast magnetization dynamics software

This section will discuss the software suitable for this experiment, along with a comparison between each competitor. In order to be viable for this experiment, it must be open-source, contain an LLG simulator that accounts for thermal fluctuations of magnetic spins, can perform Curie temperature, hysteresis and field cooling analyses and provide a visualization of the atoms and magnetic spins of the Co-Pt nanomaterial being studied.

2.7.1 VAMPIRE

VAMPIRE is a free, open-source, Linux-based software package that is easy to use, provides a visualization of the atomic structure, and computationally efficient [73]. By being open-source, anyone is able to freely use and modify the code base, meaning that not only can many groups and individual researchers collaborate to the code base, but the correctness and performance of various algorithms used by VAMPIRE can be verified. VAMPIRE only requires an input.txt file to define simulation parameters and dimensions, and a .mat file to provide descriptions about the material properties. Optionally, a .ucf file could be added to describe how the atoms interact and organize themselves amongst each other in more complex structures. The output is provided as an array of values in a .txt file, and a set of atom and spin coordinates provided by .data and .meta files that can be converted into an .xyz file that can be analyzed using visualization software like jmol. The output file can further be analyzed with MATLAB or Microsoft Excel. A visualization of this procedure can be seen in fig 2.10. Nanoparticles, multilayers and user-defined atomic systems can be produced, and the spins of each atom can be visualized. With the use of the message passing interface (MPI) library, VAMPIRE is able to make use of multiple processors when running an atomistic simulation [73]. In other words, multiple cores can be used to run one simulation. VAMPIRE also includes GPU accelerated features compatible with CUDA and OpenCL, meaning that simulations can be run up to 40 times faster [73].

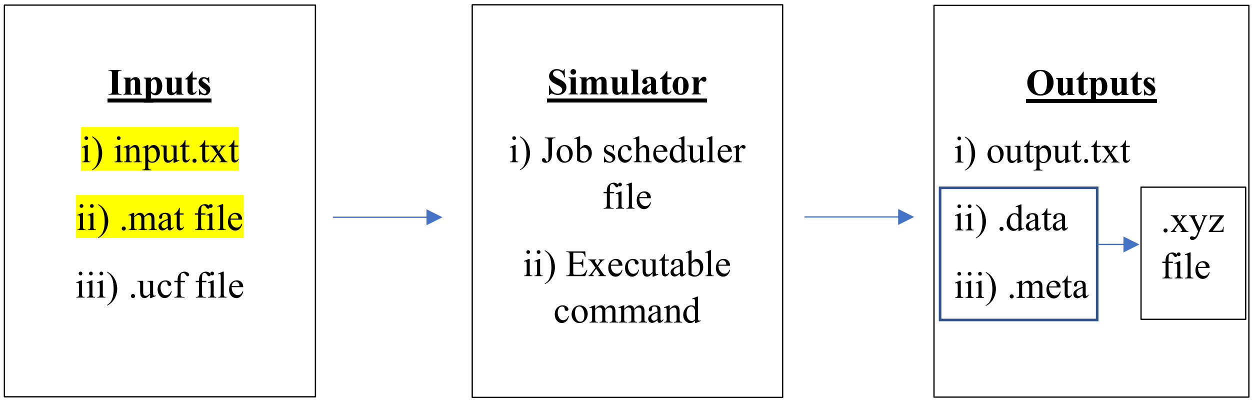

Fig. 2.10. A general flowchart of how to use VAMPIRE, along with what could be added to make this process more efficient. Note that when using 64 CPU/cores and splitting each simulation into 16 processes, up to 4 simulations can be executed at a time with the Graham supercomputer – more simulations can be run if more memory and processors are available. The files highlighted in yellow are the mandatory inputs required by the simulator.

2.7.2 Other competitors

Notable candidates include: UppASD (Uppsala Atomistic Spin Dynamics) and Boris. Boris, UppASD and VAMPIRE are all atomistic magnetic simulators capable of solving the LLG equations on multi-processor hardware. However, unlike VAMPIRE, UppASD can only produce 2D models of atoms and their spins [74]. Since lattice structures and thin-films are typically 3D in nature, it is better to use a software that can produce accurate models, making it easier to debug errors in code and to ensure a given script of code produces the correct model. Additionally, unlike VAMPIRE, Boris is only able to solve differential equations such as the LLG equations with the LLG-Heun method [75]. Since there is a possibility that the Monte-Carlo simulator could provide more accurate solutions in a time-efficient manner, and a possibility that a given script of code could produce a thin-film or lattice that does not match its expected appearance, it is better to use VAMPIRE. There is also more flexibility with regards to how the structure can be modelled in VAMPIRE – the other competitors only have an ordered alloy capability. Most importantly, VAMPIRE has more contributors, making the software more functionally reliable because it was likely to be tested more intensively. VAMPIRE’s predictions are compared to theoretical literature.

2.8 Methodology used in this computational work

VAMPIRE will be the simulator used to model ultrafast magnetization dynamics software, multi-layer values will be used in an effective medium, and an atomistic-spin model will be used when analyzing the spin dynamics. A visualization of the thought process used to come up with this methodology can be seen in fig 2.11. A visualization of the thought process of how the magnetization dynamics are modelled for a given atomic model and structural formation can be seen in figure 2.12. With the use of an effective-medium atomistic spin model that is solved by using the LLG-Heun method, while neglecting dipolar effects due to how little they affect the hysteresis loops, not only will HAMR systems be realistically modelled (as thin-films are typically used in HAMR systems), but the calculations can be performed at a faster rate, while keeping the computational demands low [76]. Although the atomistic-spin model is a simplistic model regarding how the spins are distributed amongst a system, complexities to this model will slowly be built up throughout chapters 3 and 4.

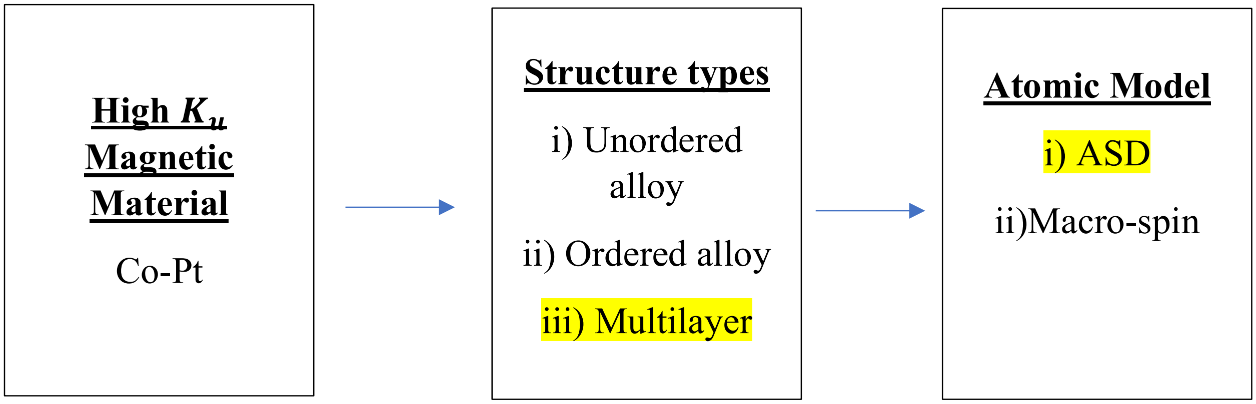

Fig. 2.11. A visualization of how the structural and atomic framework has been chosen. First, a magnetic material must be chosen, then the appropriate material structure must be chosen. Afterwards, the appropriate software to model the structure of the nanomaterial is either found or produced. For this simulation, VAMPIRE will be used as the software of choice. The terms highlighted in yellow are the options that were chosen.

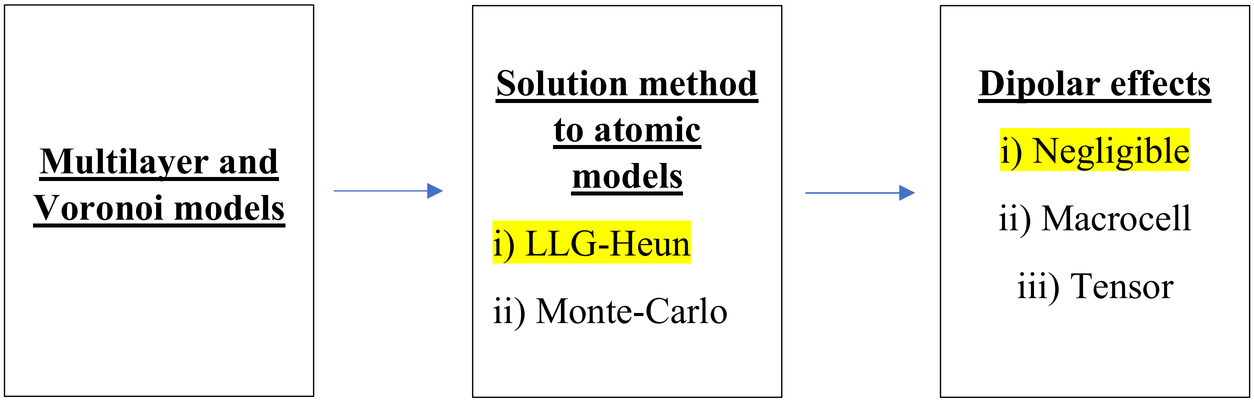

Fig. 2.12. A visualization of how the magnetization dynamics framework has been chosen for a given set of atoms.

2.9: Chapter 2 Summary

When modelling Co-Pt based thin films, the first thing to consider is how a single atom/particle is going to be structured, then considering how all the atoms are going to arrange themselves amongst one another (alloy or multi-layer). These considerations will drastically affect how K_{ui}, μ_s, J_{ij} are interpreted and obtained from literature values. After the structural properties have been determined, the equations representing the magnetization dynamics of a Co-Pt structure will be chosen, along with an appropriate solver. Optionally, on top of the effective applied field ($\boldsymbol{H}_{eff}^{i}$), dipolar effects could be added to make computations more accurate. Once the magnetization dynamics have been verified for an arrangement of atoms/particles, a method of structurally modelling the Co-Pt thin films must be chosen. For this thesis, each atom will be a mixture of cobalt and platinum, and a disordered alloy structure will be used. This drastically reduces the complexity of our simulations by ensuring that one value of J_{ij} will be required instead of an entire matrix, as each atom is the same. However, K_{ui}, μ_s and T_c values will be obtained from multi-layer data. This is also known as an effective medium model – modelling atoms as a disordered alloy, while using multi-layer parameters. Regarding the magnetization dynamics, an atomistic sLLG model will be used. Thin film grains will be modelled using a Voronoi approach, as these grains depict realistic thin films very effectively. All of this was modelled with VAMPIRE.

CHAPTER 3: EFFECTIVE MEDIUM MODELS OF Co-Pt PARTICLES

3.1 Overview

The effective medium model is a way of modeling the macroscopic properties of nanomaterials composed of two or more different types of atoms by making assumptions about how each atom interact with each other on the atomistic scale [77] and treating the Co-Pt sample as a sample that contains one type of atom. Because each platinum atom behaves and locates themselves differently on a surface composed of cobalt atoms, the task of modelling every interaction scenario between cobalt and platinum would require too many intricate sub-models to add. As there are not enough examples or literature readings to look into, it is best to start with a simplistic model, then add complexities that VAMPIRE can handle to understand the intergranular and interfacial behaviour of Co-Pt thin-films that affect the HAMR system performance. Additionally, since there are not many software platforms capable of handling thermally induced magnetic effects, it is best to not use a model too complex for VAMPIRE or a typical supercomputer to handle. The extra complexity of adding the intricate sub-models might not even be worth exploring – it is best to have a simplistic model that can predict the future of HAMR technologies as accurately as possible so that many researchers can use and understand it with ease.

3.2 Single nanoparticle analysis

Before analyzing an effective Co-Pt model, the Curie temperature as a function of the cobalt particle size is analyzed as an "exercise" to get familiar with the tool by learning how to perform Curie temperature and hysteresis calculations, along with producing the appropriate graphs with the data outputted from VAMPIRE. In other words, this is to ensure that VAMPIRE produces the correct results for a single particle. Before producing the graphs, the μ_s and bulk T_c values were obtained from the VAMPIRE manual [78] and the literature [31], respectively. Afterwards, J_{ij} was computed from T_c by using the following formula: $J_{ij} = \frac{3T_c k_B}{\varepsilon \cdot z}$. For FCC cobalt, $\varepsilon = 0.79$ and $z = 12$ [79]. ε represents the correction factor relating to the spin wave stiffness, and *z* represents the number of spin interactions. As there is no universal curve regarding the Curie temperature and particle size graph, it is necessary to analyze the impacts of the decay of the exchange interaction at smaller particle sizes due to the effect of surface atoms that do not contribute anything to the exchange interaction. To obtain a curve representing the Curie temperature as a function of particle size, the normalized magnetization as a function of temperature (as seen in figure 1.9 of section 1.5) was computed for the following particle sizes: 0.25 nm, 0.5 nm, 0.75 nm, 1.0 nm up to 8.0 nm in 1.0 nm increments, and bulk (periodic boundary conditions for x, y and z dimensions). Afterwards, the Curie temperature was calculated for each particle size by doing the curve fitting method mentioned in section 1.5, and plotted. Note that the same analysis is not performed for a single platinum particle because they are paramagnetic (low μ_s), meaning they do not retain any permanent magnetic properties once an external magnetic field is removed. At the end of section 3.5, the Curie temperature vs. particle size graphs for a single Co particle, along with the three types of Co-Pt particles, will be compared (see figure 3.12, or table 3.3). The easy and hard axis loops for a single Co particle at $0^{\circ}K$ and $300^{\circ}K$ were produced to analyze thermal effects and their impacts on the hysteresis loops. Looking at figure 3.1, the reason why the easy and hard axis hysteresis loops have the same shape is because the anisotropy constant is set to zero (single particles do not have anisotropy). Looking back at section 1.6, hysteresis is produced when a material has a spontaneous magnetization without an applied field.

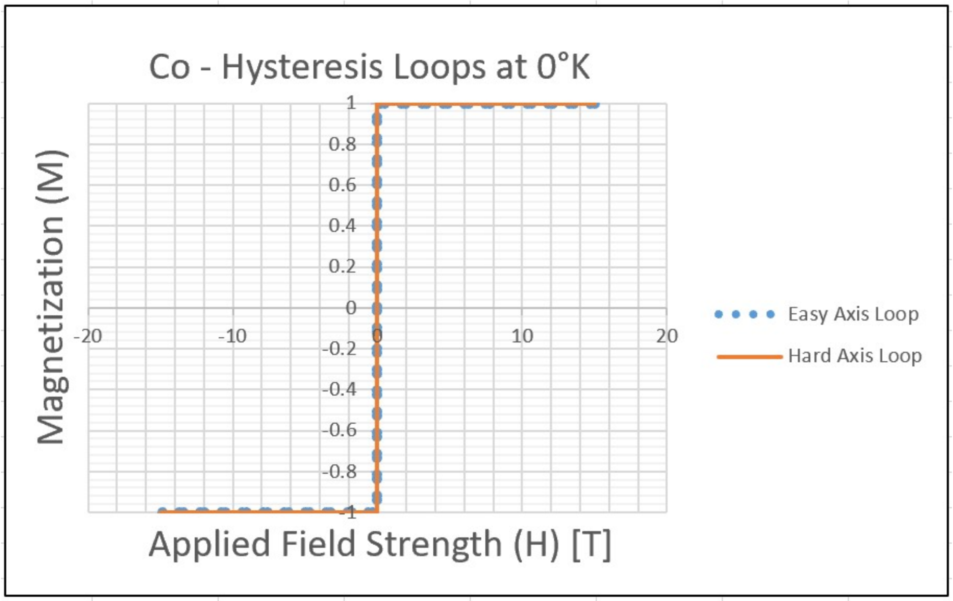

Fig 3.1. Easy and hard axis loop for bulk Co at 0°K.

Due to not having any anisotropy, figure 3.1 and 3.2 will have similar shapes. However, due to thermal fluctuations, the saturation magnetization value will never reach 1.0 due to thermal fluctuations that randomly change the spin directions throughout the simulation. Instead, an arbitrary value between 0.80 to 0.90 will be reached.

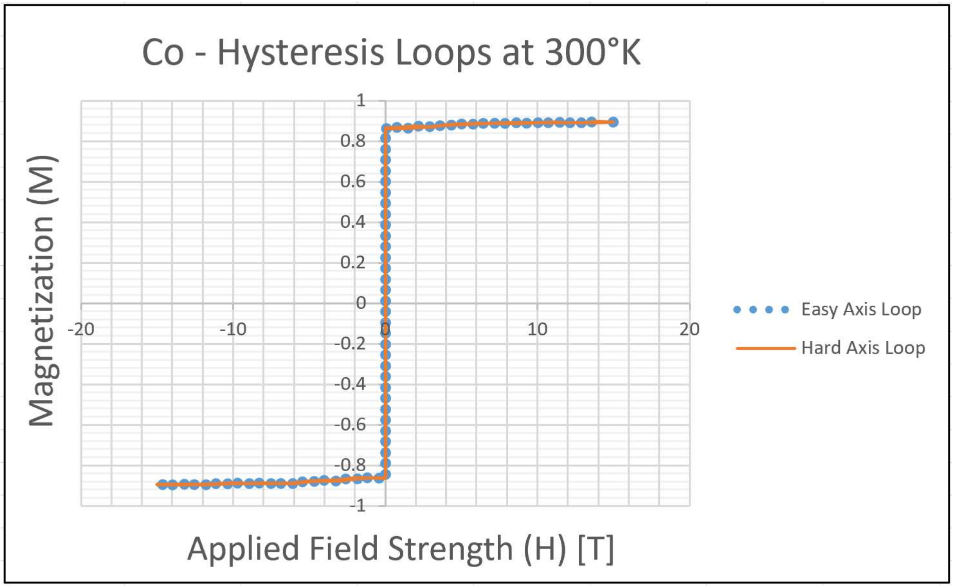

Fig 3.2. Easy and hard axis loop for bulk Co at 300°K.

3.3 Procedure of developing an effective medium model

Several modifications will have to be made with regards to how the multi-layer values are interpreted. Instead of using a matrix to represent the exchange parameter (J_{ij}), a single value is used. This reduces the complexity of the multi-layer model because all of the different types of interactions between cobalt and platinum atoms do not have to be accounted for. The most important parameters are: K_{ui}, μ_s, J_{ij}. These values are entered in the model on a per atom basis rather than a volumetric parameter such as that obtained from experiments. Therefore, in order to calculate these parameters from available data from the literature, calculations seen in section 3.3.1 must be performed in order to obtain these values. Table 3.1 contains the list of physical property values for each sample, while table 3.2 contains the magnetic property values for K_{ui}, μ_s, J_{ij}. The atoms are treated as a combination of cobalt and platinum – in other words, there is only one type of atom that contains properties of both cobalt and platinum, depending on the % composition of cobalt and platinum within the atom. By increasing the % amount of cobalt within the atom, it is expected to see an increase in μ_s and K_{ui} due to its ferromagnetic nature. Details on how these values were obtained will be outlined throughout this section.

3.3.1 Obtaining the molar mass and density of a Co-Pt sample

In order to begin, the thickness of the cobalt and platinum layers must be provided. These values were obtained from previous measurements of Co-Pt nanomaterial samples available in the HEATED lab. These samples were grown at the Helmholtz-Zentrum Dresden-Rossendorf by Ms. Olga Andryievska under the supervision of Prof. Olav Hellwig (University of Chemnitz). The relative layer thickness and total number of layers is obtained through careful tuning of the deposition rates and verified through X-Ray reflectivity. To obtain the number of atomic layers within the sample, the cobalt and platinum layer thicknesses were divided by the layer separation of the cobalt and platinum bulk crystals, respectively [80]. The layer separation was obtained by finding the lattice parameter of cobalt and platinum. By using the appropriate selection of substrate layers (see figure 1.7), both cobalt and platinum layers have a face centered cubic (FCC) lattice structure [81, 82]. Once the number of atomic layers has been found, the concentration of cobalt and platinum atoms (also known as the % composition) were obtained by dividing the number of atoms of a particular type by the total number of atoms within a layer. To obtain the molar mass and density of a Co-Pt thin-film, the molar masses and densities of cobalt and platinum were obtained from datasheets from MaterialsProjects.org [83, 84], then each value was multiplied by the concentrations of the cobalt and platinum atoms, respectively. Afterwards the molar masses and densities were added to each other. The calculation performed was a weighted average calculation.

3.3.2 Obtaining the uniaxial anisotropy constant

To obtain the uniaxial anisotropy constant, a graph that was obtained from a study performed by the Material Science Department of the Lawrence Berkeley National Laboratory was interpolated in order to get the appropriate uniaxial anisotropy value. The graph can be seen in figure 3.3. Afterwards, the units were converted from $\frac{erg}{cm^3}$ to $\frac{J}{atom}$ by using the following equation:

$$K_{ui}\left[\frac{J}{atom}\right] = K_{ui}\left[\frac{erg}{cm^3}\right] \cdot 10^{-7}\left[\frac{J}{erg}\right] \cdot \frac{M_M\left[\frac{g}{mol}\right]}{\rho\left[\frac{g}{cm^3}\right] \cdot N_a\left[\frac{atoms}{mol}\right]} \tag{3.1}$$

The purpose of the above equation is to express the anisotropy energy in terms of atomic interactions as opposed to an arbitrary volume within the medium. This equation comes in 2 parts: (1) converting J to erg by multiplying by the conversion factor of 10^{-7} (as per definition) and (2) finding the volume each atom occupies up with the conversion factor $\frac{M_M}{\rho N_a}$. To find the volume each atom occupies, the molar mass of each atom was converted to units of mass per atom by dividing by Avogadro's constant, N_a. Afterwards, to get the amount of volume each atom occupies, the mass per atom is divided by the density of the material of focus ($\frac{cm^3}{atoms}$). The second part of the equation is responsible for converting cm^3 to number of atoms. The above conversion is necessary because VAMPIRE uses $\frac{J}{atom}$ units for the uniaxial anisotropy constant. The units are shown in square brackets beside each variable in equation 3.1.

Table 3.1: Physical property values [35]. Given a sample, Co_xPt_y, x and y represent the layer thickness (in Angstroms) of the cobalt and platinum within a thin-film, respectively.

Sample type	Number of atomic layers	Concentration	Molar Mass $[\frac{g}{mol}]$	Density $[\frac{g}{cm^3}]$
Co_4Pt_7	Co: 2 Pt: 3	Co: $\frac{2}{2+3} = \frac{2}{5}$ Pt: $\frac{3}{2+3} = \frac{3}{5}$	140.63	15.948
Co_4Pt_{11}	Co: 2 Pt: 5	Co: $\frac{2}{2+5} = \frac{2}{7}$ Pt: $\frac{5}{2+5} = \frac{5}{7}$	156.144	17.276
Co_6Pt_6	Co: 3 Pt: 3	Co: $\frac{3}{3+3} = \frac{1}{2}$ Pt: $\frac{3}{3+3} = \frac{1}{2}$	127.01	14.79

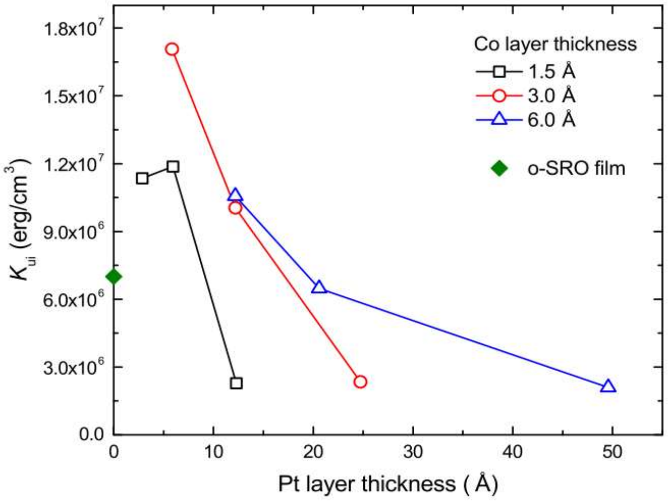

Fig. 3.3. Uniaxial anisotropy at 300 °K vs. the layer thickness of the platinum portion of a Co-Pt multilayer thin film [85].

3.3.3 Obtaining the exchange interaction constant

To obtain the exchange interaction constant, the Curie temperature must be obtained first because the exchange constant is dependent on the Curie temperature. The Curie temperature was interpolated from a graph produced by the Material Science Department of the Lawrence Berkeley National Laboratory. The graph can be seen in figure 3.4. Afterwards, the exchange interaction constant was calculated by using the following equation:

$$J_{ij}\left[\frac{J}{atom}\right] = \frac{3\cdot T_C[K]\cdot k_B[\frac{J}{K}]}{\varepsilon\cdot z[atoms]} \tag{3.2}$$

The main purpose of the above equation is to find how much energy is being expended per atomic interaction. The Curie temperature is first multiplied by Boltzmann’s constant to convert temperature to energy, then divided by the number of spin interactions that occur within an FCC lattice, z. We multiply by 3 to account for each dimension, then divide by ε to account for spin wave stiffness found within atoms that originates from the orbital structure of a given atom. In other words, this represents how slowly the energy gets transferred between each atom, resulting in a deduction of energy per atom. The expected curie temperature for a given Co-Pt sample is used, and the FCC values for ε and z values, which are 0.79 and 12, respectively, are used [32].

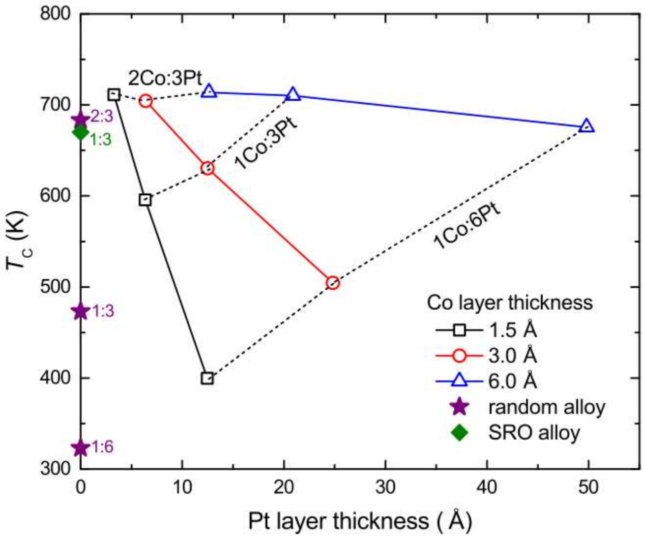

Fig. 3.4. Curie temperature vs. FCC Pt layer thickness for multi-layers of varying FCC Co compositions (different coloured lines represent different compositions) [85].

3.3.4 Obtaining the atomic spin moment value

To obtain the atomic spin moment value, a graph that was obtained from a study performed by the Material Science Department of the Lawrence Berkeley National Laboratory was interpolated in order to get the appropriate atomic value. The graph can be seen in figure 3.5. Afterwards, the values for the saturation magnetization of the samples were converted from $\frac{emu}{cm^3}$ to $\frac{A}{m}$, and expressed as multiples of Bohr units (μ_b), by performing the following calculation:

$$\mu_s[\mu_b] = M_s\left[\frac{emu}{cm^3}\right] * 1000\left[\frac{A\cdot cm^3}{m\cdot emu}\right] * \frac{\ell_{cell}{}^3\,[m^3]}{4\cdot\,\mu_b[A\cdot m^2]} \tag{3.3}$$

$$\ell_{cell}\,[m] = (\frac{4\cdot M_M}{\rho\cdot N_a})^{\frac{1}{3}} \tag{3.4}$$

Note that $\mu_b = 9.274\cdot 10^{-24}\ \frac{J}{T}\ or\ A\cdot m^2$. Equation 3.3 represents the formula for converting M_s to its corresponding atomic spin value in Bohr units (μ_b), μ_s, which is the unit that VAMPIRE uses. The '4' in the denominator is for the number of atoms per unit cell in an FCC lattice. Dimensional analysis is performed to convert $\frac{emu}{cm^3}$ to $A\cdot m^2$. Regarding equation 3.4, the lattice cell length (ℓ_{cell}), also known as the lattice parameter *(a)*, for an FCC lattice is shown in equation 3.4. Since the FCC lattice structure is shaped like a cube, the volume can be found by cubing ℓ_{cell}.

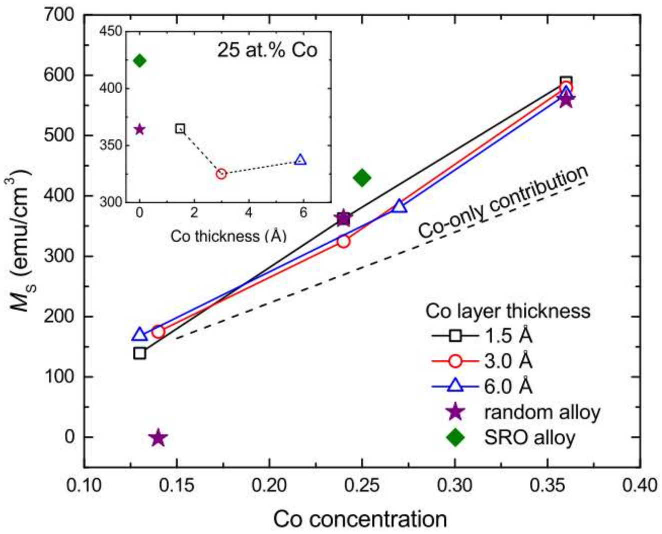

Fig. 3.5. Saturation magnetization vs. Co concentration for varying layer thicknesses [85].

Table 3.2: Values of magnetic properties calculated for the simulations performed in section 3.4 of this thesis. Note: $\mu_b = 9.27 * 10^{-24} \frac{J}{T}$.

Sample type	$\text{K}_{\text{ui}} \left[\frac{J}{atom}\right]$	$\text{J}_{\text{ij}} \left[\frac{J}{atom}\right]$	$\mu_s\ (300^{\circ}K)$
Co_4Pt_7	$9.024 \cdot 10^{-22}$	$3.058 \cdot 10^{-20}$	$0.936\mu_b$
Co_4Pt_{11}	$6.529 \cdot 10^{-22}$	$2.760 \cdot 10^{-20}$	$0.647\mu_b$
Co_6Pt_6	$2.721 \cdot 10^{-23}$	$3.058 \cdot 10^{-20}$	$1.154\mu_b$

3.4 Fine-tuning the effective medium model for our Co-Pt samples

Once all of the calculations in section 3.3 have been performed, K_{ui}, μ_s and J_{ij} must be tuned to ensure that the Curie temperature and saturation values matched the literature values. This section will describe some of the simulations performed with VAMPIRE, and how they were used to verify the results obtained from the calculations performed in section 3.3. Table 3.3 contains the values of K_{ui}, μ_s and J_{ij} used in the calculations in the following chapters, so that the Co-Pt thin-films behave in accordance to the literature and measurements made on our own samples [85]. The values were changed with educated guesses – increasing K_{ui} increased the saturation field in hard axis loops, increasing μ_s decreased the saturation magnetization value, and increasing J_{ij} increased the Curie temperature.

Table 3.3: Table of values showing the adjusted values of table 3.2 (at $300^{\circ}K$, except for μ_s). Note: $\mu_b = 9.27 * 10^{-24}\ \frac{J}{T}$

Sample type	$K_{ui}\left[\frac{J}{atom}\right]$	J_{ij}	$\mu_s\ (0^{\circ}K)$
Co_4Pt_7	$3.131 \cdot 10^{-23}$	$3.108 \cdot 10^{-21}$	$1.246\mu_b$
Co_4Pt_{11}	$2.761 \cdot 10^{-23}$	$2.589 \cdot 10^{-21}$	$0.983\mu_b$
Co_6Pt_6	$2.721 \cdot 10^{-23}$	$3.139 \cdot 10^{-21}$	$1.32\mu_b$

3.4.1 Exchange interaction value

The Curie temperature of the bulk Co-Pt crystals was modelled by letting the unit cell of an FCC lattice having the effective medium magnetic properties determined above have periodic boundary conditions in all cartesian dimensions The value for J_{ij} was adjusted until the correct Curie temperature was obtained [85]. The obtained exchange values were smaller than what was calculated in section 3.3 exchange values to produce the calculated Curie temperature by up to a factor of 10. A possible reason for this offset is that equation 3.2 is valid for ferromagnets with nearest-neighbor exchange. Since the values for J_{ij} in Table 3.3 are smaller than anticipated, it suggests that the exchange interactions in Co-Pt are not limited to nearest neighbor (NE) exchanges alone, and contributions from atoms that are further away play a role in ferromagnetic ordering.

3.4.2 Uniaxial anisotropy constant

Hard axis loops were computed for the bulk Co-Pt crystals (using the same effective medium model and periodic boundary conditions). Regarding the hard axis loop, the K_{ui} value was adjusted until the anisotropy field, H_k, of the model matched the values obtained in the literature, knowing that $H_k = \frac{2K_{ui}}{M_s}$ [85]. The hard axis loops at $300\ °K$ for the three types of Co-Pt multi-layers analyzed in this work are shown in figures 3.6 to 3.11, inclusive. To get H_k, the values of K_{ui} and M_s were obtained from figures 3.3 and 3.5, respectively (kept in c.g.s units), and plugged into formula 1.1 of section 1.2.2 (ignoring the shape anisotropy term, $H_k = \frac{2K_{ui}}{M_s}$). Afterwards, the units of H_k were converted to Teslas by multiplying it by 10^{-4}. A different value of K_{ui} had to be used for simulations running at a temperature of $0°K$ and $300°K$ since the literature only contained values at $300°K$, whereas material properties in VAMPIRE are specified at $0°K$. Equation 3.5 had to be used to convert the K_{ui} from $300°K$ to $0°K$ [86]:

$$K_{ui}\ @\ 0°K = \left(\frac{[M_s\ value\ at\ 0°K]}{[M_s\ value\ at\ 300°K]}\right)^3 \cdot [K_{ui}\ @\ 300°K] \qquad (3.5)$$

The calculated values of the uniaxial anisotropy at $300°K$ constant were larger than the required K_{ui} values to produce the calculated H_k value by up to a factor of 5. A possible reason for this includes: conversion between H_k and K_{ui} values produced more uncertainty, as the relationship between them included the value of M_s. According to a study done by Vickie W. Guo et al. [87], a decrease in interfacial smoothness occurs as the Pt layer thickness (t_{Pt}) decreases, which affects the K_{ui} value. For multi-layers with a Co layer thickness (t_{Co}) between 0.4 and 0.7 nm, deviations from the linear relation seen in figure 3.3 occur when t_{Pt} is less than 0.5 nm. For multi-layers with t_{Co} below 0.4 nm, deviations from the linear relation occur when t_{Pt} is less than 1 nm. This can be seen in figure 3.6.

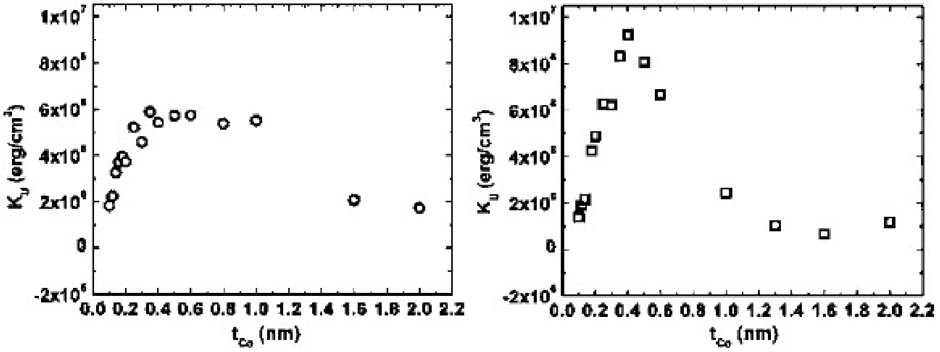

Fig 3.6. K_{ui} at $300\ °K$ vs. t_{Co} for a t_{Pt} value of 1.0 nm (left) and 0.5 nm (right) [87].

3.4.3 Atomic spin moment

Easy axis loops were also computed for the bulk Co-Pt sample. The μ_s value was adjusted until the room temperature saturation magnetization of the sample matched the values obtained in the literature. The easy axis loops at $300°K$ for the three types of Co-Pt multi-layers analyzed in this work are shown in figures 3.6 to 3.11, inclusive. For the bulk material, the coercivity and anisotropy field values are equal to each other [85], as the spin direction needs to overcome the anisotropy field value in order to switch. However, by changing μ_s, H_k also changed, meaning that K_{ui} had to be adjusted by a bit. Additionally, since μ_s decays with temperature, and since the literature only contained values at $300°K$, the following equation had to be used to convert the μ_s from $300^{\circ}K$ to $0^{\circ}K$ [86]:

$$M_s\ at\ 0°K = \frac{[M(T=0°K)][M_s\ at\ 300°K]}{[M(T=3\quad °K)]} \tag{3.6}$$

As a reminder, we note that $M(T) = (1 - \frac{\mathrm{T}}{\mathrm{T_C}})^{\frac{1}{3}}$. More details regarding $M(T)$ can be found in section 1.5 of this thesis. The M_s value at $300°K$ was obtained from figure 3.5. Overall, the values of μ_s used were 20-50% larger than the calculated values – possible differences could arise from the way the effective medium model oversimplifies the induced magnetization that Pt atoms neighboring the Co atoms obtain (Pt becomes slightly magnetic next to Co, but the effect is only near the surface at the Co/Pt interface).

3.5 Single Co-Pt particle analysis

Once the proper K_{ui}, μ_s and J_{ij} have been obtained, the same analysis performed in section 3.2 will be done for each of the samples found in our lab. Note that every figure description for each hysteresis loop contains the coercivity and anisotropy field value. The main purpose of this analysis is to see how the particle size affects the Curie temperature amongst different samples; this trend may come in handy for section 5 of this thesis, where the factors affecting switching probably is analyzed. Unlike section 3.2, the easy and hard axis loop shapes should not look the same due to hysteresis that arises from anisotropy effects. However, all loops share the fact that magnetization value of “1” is only attainable at $0°K$, as there are no thermal fluctuations at this temperature. An increase in temperature is expected to reduce the coercivity and anisotropy field of a given Co-Pt sample, as an addition of thermal energy makes it easier to switch spin directions.

3.5.1: Hysteresis loops of Co_4Pt_7 particles

Looking at the easy axis loops from figures 3.6 and 3.7, the coercivity reduces by a factor of approximately 3.5 $(\frac{10.2\ T}{2.9\ T})$. The reason for this is because at a higher temperature, the spins have more thermal energy, making it easier to change their spin direction. Therefore, less field strength is required to change the direction of the spins. The anisotropy field value decreases by a factor of 3.4 $(\frac{11.3\ T}{3.3\ T})$, as less magnetic field is required to alter the direction of the spins due to an increase in thermal energy within the system. Figure 3.8 has more “noise” due to thermal fluctuations that occur at room temperature.

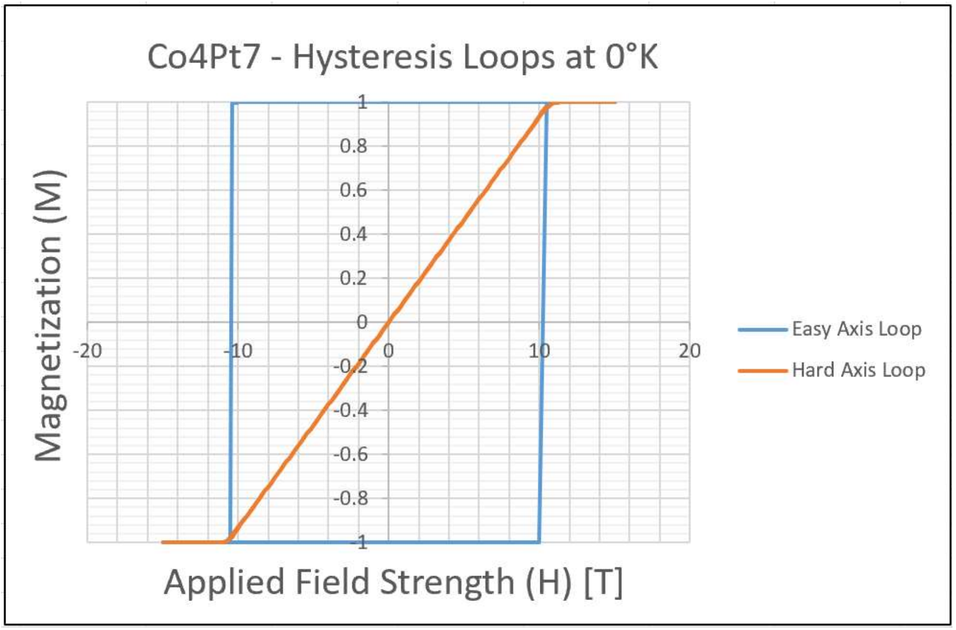

Fig 3.7. Hysteresis loops of bulk Co_4Pt_7 produced at 0°K. The coercive and anisotropy field values are approximately 10.2 T and 10.7 T, respectively.

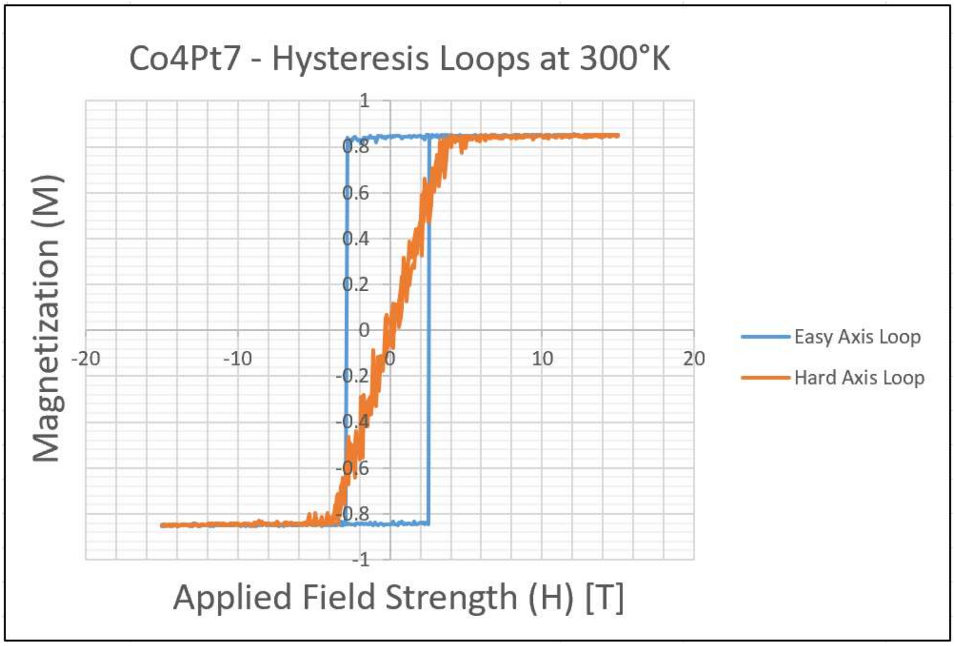

Fig 3.8. Hysteresis loops of bulk Co_4Pt_7 produced at 300°K. The coercive and anisotropy field values are approximately 2.9 T and 3.3 T, respectively.

3.5.2: Hysteresis loops of Co_4Pt_{11} particles

Looking at the easy axis loops from figures 3.7 and 3.8, the coercivity reduces by a factor of approximately 6.7 ($\frac{19.5\,T}{2.9\,T}$) due to the same reasons mentioned in section 3.5.1. Additionally, when looking at the hard axis loops from figures 3.9 and 3.10, the anisotropy field value decreases by a factor of 5.0 ($\frac{20.1\,T}{4.0\,T}$), due to the same reasons mentioned in section 3.5.1. Figure 3.9 has more "noise" due to thermal fluctuations that occur at room temperature.

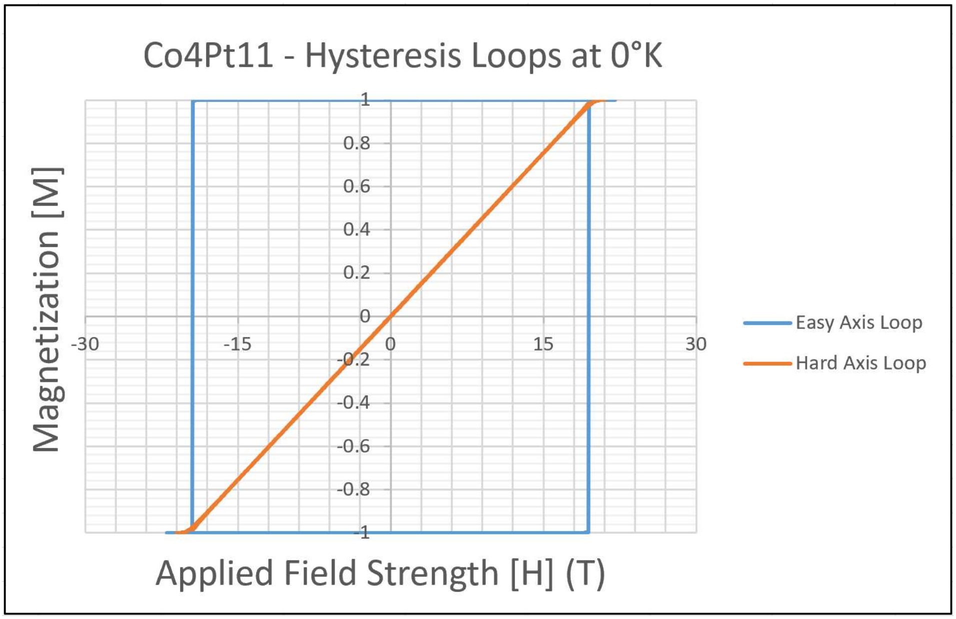

Fig 3.9. Hysteresis loops of bulk Co_4Pt_{11} produced at 0°K. The coercive and anisotropy field values are approximately 19.5 T and 20.1 T, respectively.

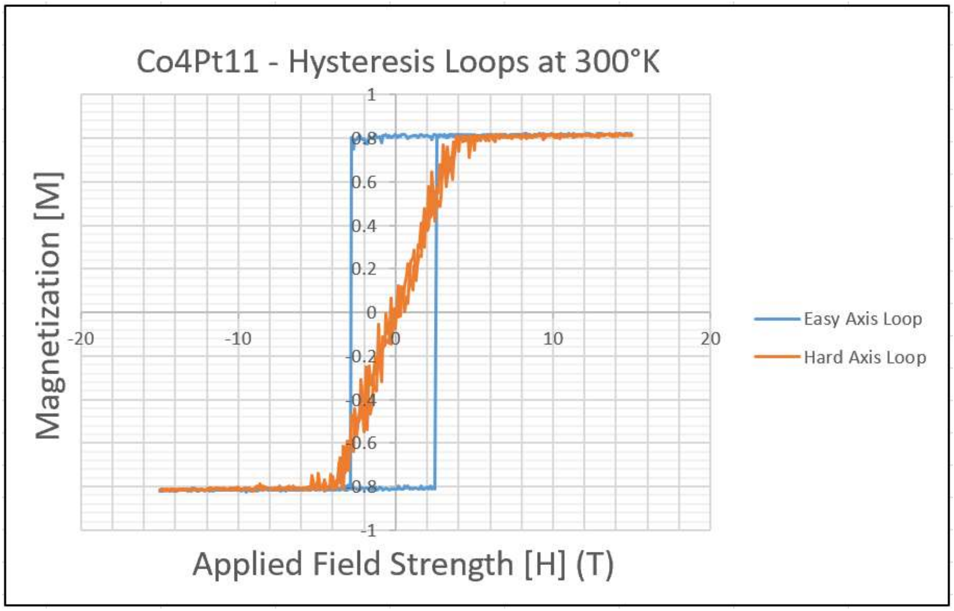

Fig 3.10. Hysteresis loops of bulk Co_4Pt_{11} produced at 300°K. The coercive and anisotropy field values are approximately 2.9 T and 4.0 T, respectively.

3.5.3: Hysteresis loops of Co_6Pt_6 particles

Looking at the easy axis loops from figures 3.10 and 3.11, the coercivity reduces by a factor of approximately 10.4 ($\frac{10.4\ T}{1.0\ T}$) due to the same reasons mentioned in section 3.5.1. Additionally, when looking at the hard axis loops from figures 3.11 and 3.12, the anisotropy field value decreases by a factor of 2.8 ($\frac{11.1\ T}{4.0\ T}$), due to the same reasons mentioned in section 3.5.1. Figure 3.9 has more “noise” due to thermal fluctuations that occur at room temperature.

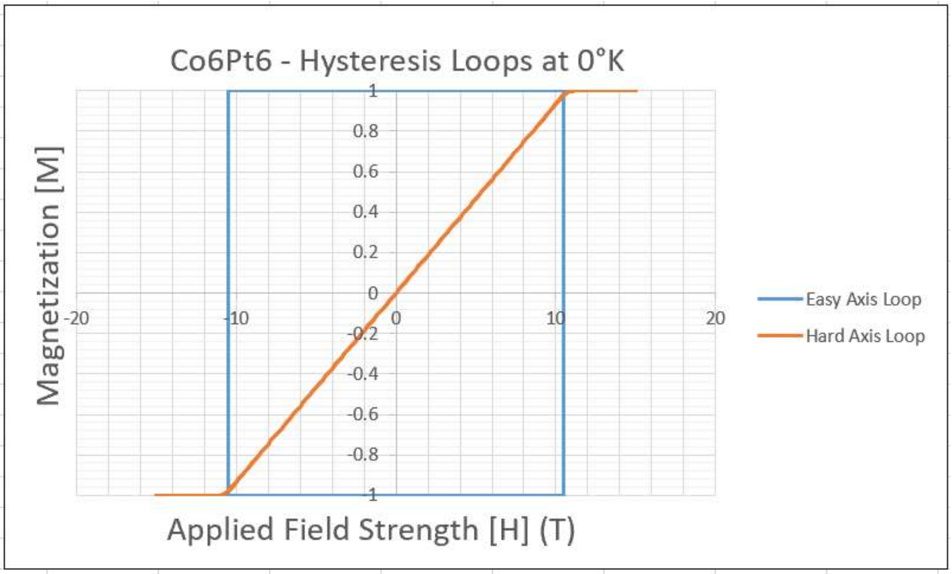

Fig 3.11. Hysteresis loops of bulk Co_6Pt_6 produced at 0°K. The coercive and anisotropy field values are approximately 10.4 T and 11.1 T, respectively.

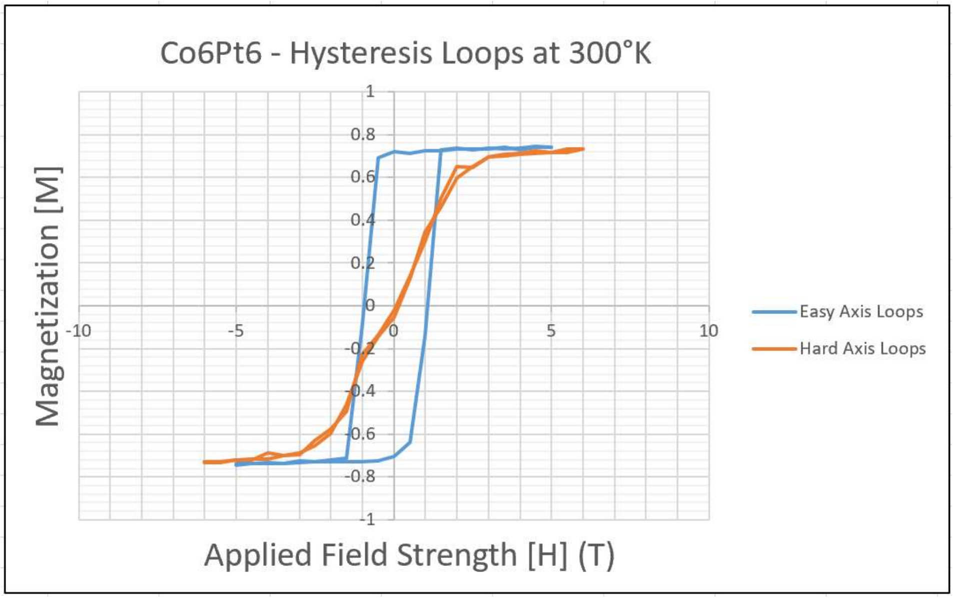

Fig 3.12. Hysteresis loops of bulk Co_6Pt_6 produced at 300°K. The coercive and anisotropy field values are approximately 1 T and 4 T, respectively.

3.6 Expected Results and Trends

The values for the exchange interaction and uniaxial anisotropy constant obtained from graphs from simulations performed on VAMPIRE match the values obtained from theoretical calculations. The easy and hard axis hysteresis loops at 0°K and 300°K seem to scale proportionally with the proportionalities listed in the case study performed by Felipe Garcia Sanchez from the Universidad de Salamanca [86] (see tables 3.5 and 3.6), which verify the impacts of thermal fluctuations on the coercivity and saturation magnetization values. For a single Co particle, the easy and hard axis loops have the exact same shape at 0°K and 300°K (different shape at different temperatures). Looking at figure 3.13, it seems that the Curie temperature of Co_4Pt_{11} increases the slowest with respect to the particle size as it requires the largest particle size to reach a Curie temperature that is 90% of the bulk Curie temperature. This implies that the exchange interaction decays the slowest as the particle size decreases. On the other hand, Co_4Pt_7 increases the fastest with respect to the particle size, as it requires the smallest particle size to reach a Curie temperature that is 90% of the bulk Curie temperature. This implies that the exchange interaction decays the fastest with respect to particle size, meaning that the more energy is required to adjust the spins of adjacent atoms. Additionally, looking at tables 3.5 and 3.6, Co_6Pt_6 has the lowest coercivity value at room temperature, meaning that its anisotropy value is low. This means that the energy barrier is smaller, making it easier to change the spin states. However, although not much higher than Co_6Pt_6, Co_4Pt_{11} has the highest saturation magnetization value, meaning that there is a stronger natural driving force to overcome the spins. This gives Co_4Pt_{11} some promise with overcoming the large anisotropy barrier it contains. Overall, it seems that Co_6Pt_6 particles look like the most promising candidate due to its combination of a large particle size to reach a Curie temperature 90% of the bulk Curie temperature, low coercivity, and high saturation magnetization value. Once all of the appropriate parameters have been chosen, the magnetization dynamics of the thin-films can now be analyzed in chapter 4, then the results and trends will be summarized in chapter 5.

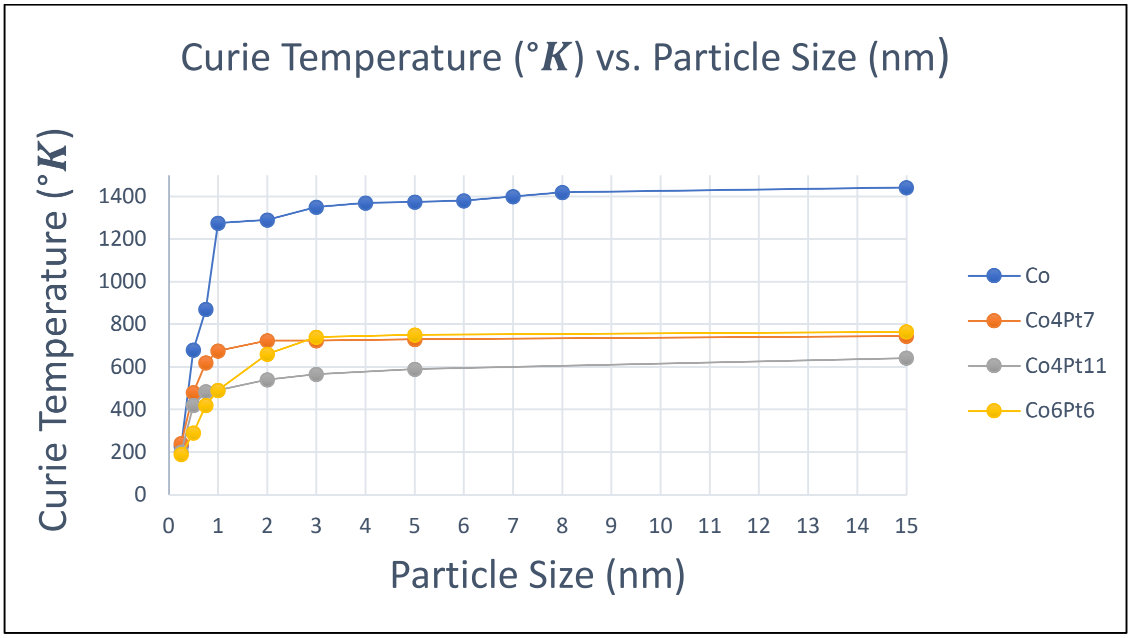

Fig 3.13. Comparison between the size distributions of Curie temperatures for the different types of samples in our lab.

Table 3.4: Summary of figure 3.12

Particle type	Particle size at which the T_c is 90% of $T_{c,bulk}$ [nm]
Co	2.1
Co_4Pt_7	0.95
Co_4Pt_{11}	3.2
Co_6Pt_6	2.4

Table 3.5: Summary of hysteresis loop data at $0^{\circ}K$

Particle type	H_c [T]	H_k $[T]$
Co	0	0
Co_4Pt_7	10.2	10.7
Co_4Pt_{11}	19.5	20
Co_6Pt_6	10.4	11.1

Table 3.6: Summary of hysteresis loop data at $300^{\circ}K$

Particle type	H_c [T]	H_k $[T]$
Co	0	0
Co_4Pt_7	2.91	3.3
Co_4Pt_{11}	2.86	3.91
Co_6Pt_6	0.992	4.0

3.7: Chapter 3 Summary

This section covers how the important parameters pertaining to a single particle of Co-Pt were obtained from the literature, and how these parameters were verified and adjusted to match trends found in literature. The results in chapter 4 (thin films) strongly depend on the accuracy and validity of the results obtained from the section. Before obtaining K_{ui}, μ_s and T_C for each sample, the composition of cobalt and platinum in terms of the atomic layers had to be calculated, along with the weighted average density and molar mass. J_{ij} was converted to T_C with formula 3.2 in this chapter (found in section 3.3.3). To verify the validity of our results, the Curie temperature as a function of particle size was analyzed for each sample, along with the easy and hard axis loops at 0°K and 300°K. Since Co_4Pt_7 has the smallest particle size in table 3.4, its exchange interaction decays the fastest, making it difficult to switch. When looking at the hysteresis loops, since Co_6Pt_6 has the lowest K_{ui} value, it has the lowest coercivity at room temperature, making it easier for thermal fluctuations to control switching behaviour. On top of that, since Co_4Pt_{11} has the lowest μ_s value, it will have the highest anisotropy field value due to the lack of natural driving force to overcome anisotropy effects. Due to these results, it is safe to hypothesize that a high K_{ui} value, along with a high μ_s value and a slow decay of J_{ij} (large particle size in table 3.4) is necessary for a magnetic medium with a high switching probability and areal density.

CHAPTER 4: MAGNETIZATION DYANMICS OF Co-Pt MULTILAYERS

4.1 Overview

As mentioned in section 2.3, there are two types of models that represent the magnetization dynamics of magnetic materials: i) atomistic and ii) macrospin models. Regardless of the model used, the equations can still be solved using the same iterative methods mentioned in section 2.4. The shape of the film also impacts the solutions to the equations in section 2.3 – more specifically, the boundary conditions and the shape anisotropy factor will change. Every time a simulation is performed, the resulting magnetic configuration may be different, as the thermal fluctuations affecting the magnetic spins are statistic in nature [60]. As a result, the switching probability of a thin-film strongly depends on statistical variances, temperature and the size of the overall fields experienced within the thin-film (externally applied and anisotropy field). Additionally, computational settings such as the time-steps and sampling rate affect the switching probability because by taking fewer samples, the results will be less accurate as the behaviour between time steps is unknown [88]. In this section, all theoretical, statistical and computational effects will be described, along with how they impact switching probability, and how they vary near the Curie temperature. In this work, grain size distributions were not varied, and the variance was kept at a constant value of 0.1.

4.2 Particle diameter and film thickness

Once all of the bulk values of Co-Pt match the literature, an appropriate particle size has to be chosen for the thin-film, so that the coercive field in the model matches that of the samples available in our lab. Given a multilayer $(Co_aPt_b)_c$, where a and b denote the Co and Pt layer thickness in Angstroms respectively, and c decontes the number of Co-Pt bi-layer repeat units, the thickness is equal to $\frac{(a+b)c}{10}$ nm (the division by 10 is a unit conversion from Angstroms to Nanometers). The *z*-dimension in the model represents the thickness of the thin-film, which is constrained to the thickness of the multi-layer $(Co_aPt_b)_c$. The grain size distribution follows a Gaussian ordering – The grain size is the mean value, and the variance is set to 0.1 nm, as suggested by the VAMPIRE manual. The *x* and *y*-dimensions, also known as the lateral film dimensions, along with the grain spacings (see figure 2.9 for a visualization), are chosen in a way that at least 50 grains (magnetic storage units) are present in a simulation. This way, computing hysteresis loop simulations will take no longer than 48 hours to complete. With more grains, more precision can be attained when measuring the switching probability. For example, if a thin-film has 50 grains, switching 99.9% of the grains would be impossible (at least 1000 grains would be required, as 999/1000 = 0.999). With at least 50 grains in the simulation, the uncertainty in the switching probability is within 2%. Once this step is finished, multiple types of grains having differing composition of Co-Pt atoms (effective model) were simulated. Table 4.1 displays the film dimensions, grain size (diameter) and spacing between adjacent grains, and the number of grains present within each multi-layer composition. Figure 4.1 displays the $M(T)$ curves for each of the four samples listed in table 4. Table 4.2 displays the Curie temperature of each multi-layer, which was calculated with the curve fitting method mentioned in section 1.5. The results obtained from figure 4.1 and table 4.2 are reasonable, as the results strongly depend on the particle size and the exchange interaction constant. Figure 4.1 and table 4.2 will be relevant in section 5.3, where the blocking temperature is calculated.

Table 4.1: Physical properties of the thin-film samples simulated.

Multi-layer Composition	Film Dimensions (nm x nm x nm)	Grain Size (nm)	Grain Spacing (nm)	Number of Grains
$(Co_4Pt_7)_3$	60 x 60 x 3.3	5.0	1.0	87
$(Co_4Pt_7)_{12}$	40 x 40 x 13.2	2.3	2.0	63
$(Co_4Pt_{11})_{12}$	45 x 45 x 18	2.7	2.0	56
$(Co_6Pt_6)_{12}$	40 x 40 x 14.4	2.3	2.0	63

4.3 Curie temperature graphs

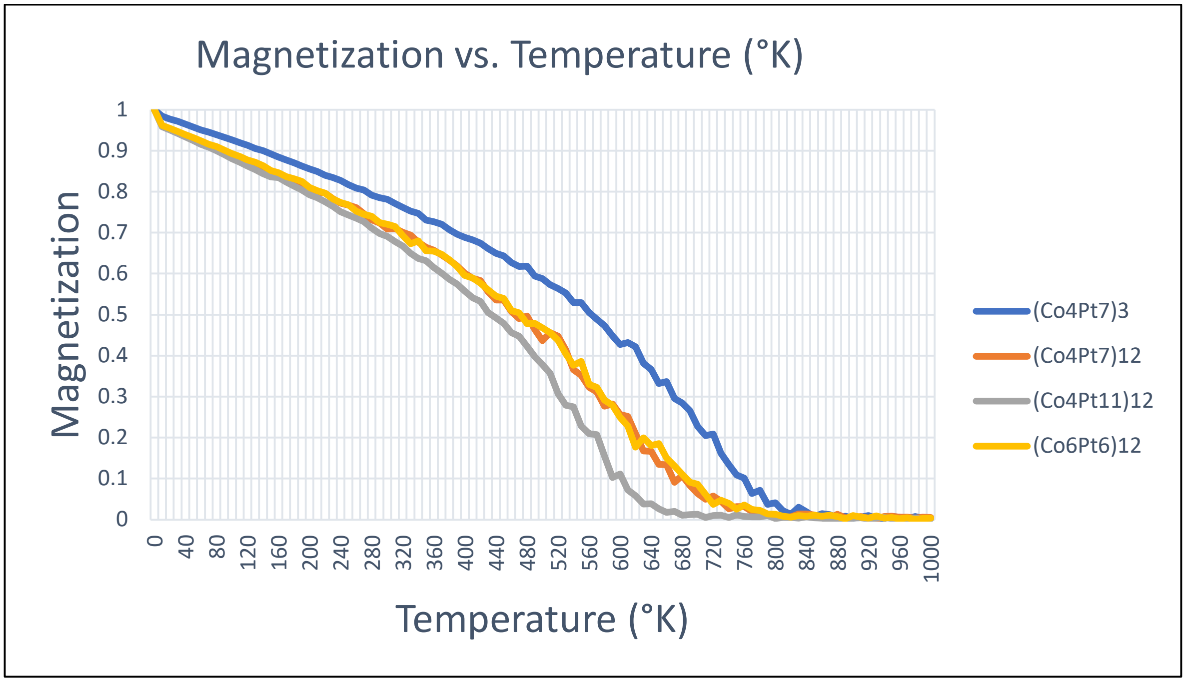

Fig 4.1. Magnetization vs. Temperature graphs for each of the 4 samples in table 4.1. $\boldsymbol{T_c}$ values, along with the procedure to obtain them, can be found in table 4.2.

When looking at figure 4.1, it is expected that the magnetization of $(Co_4Pt_7)_3$ decreases the slowest with respect to temperature due to its large grain size (as seen in table 4.1), and its high J_{ij} value (as seen in table 3.3), resulting in the highest T_c value, as seen in table 4.2. On the other hand, it is expected that $(Co_4Pt_{11})_{12}$ decreases the fastest with respect to temperature due to its combination of a small grain size and a low J_{ij} value, resulting in the lowest Curie temperature value.

Table 4.2: Curie temperature of each sample. These values were obtained from the curve fitting procedure explained in section 1.6.

Multi-layer Composition	Curie Temperature [°K]
$(Co_4Pt_7)_3$	754.57
$(Co_4Pt_7)_{12}$	685.28
$(Co_4Pt_{11})_{12}$	605.85
$(Co_6Pt_6)_{12}$	695.50

4.4 Hysteresis loops from our lab

This section will display the easy axis loops at $300^{\circ}K$ of all the four samples that were experimentally measured in our lab, along with the easy axis loops at $300^{\circ}K$ that were produced with the use of VAMPIRE. Afterwards, the shape of these loops, along with their coercivity values, will be compared with each other. The hard axis loops were not recorded, as the experimental anisotropy field was much higher than the field that was available in the magnetometer. It will be assumed here that the anisotropy field of the samples are the same as those in the reference material compositions found in the literature and discussed in chapter 3. Here, the models are matched to the experimental hysteresis loops by varying the particle size, as once the K_u, T_c, H_{app} and M_s have been fixed, the only way to adjust the coercivity of the sample is by adjusting the particle size. The coercive field is also known as the minimum applied magnetic field required for switching. The smaller the particle size, the smaller the coercive field. See figure 1.10 from section 1.7.1 for a review on how the coercive field values are obtained. The deposition pressure of the samples in our lab were varied, but the effects on the coercivity due to pressure will not be presented here. In practice, low-pressure deposition yields closely interconnected grains that cause the film to switch through domain wall nucleation and propagation. These films are not suitable for high-density magnetic recording. On the other hand, higher deposition pressure yields grains that are decoupled so that the grains switch independently. A pressure that is too high yields grains that are too small, leading for them to be superparamagnetic (particle size at which $T_c \leq 90\%\ of\ T_{c,bulk}$). We select the films that are deposited at the most optimal pressure, which yields grains that are decoupled and produce high-coercivity hysteresis loops containing a relatively square shape. Figures 4.2 to 4.5 (inclusive) will compare the simulated and experimental hysteresis loops between each other for each sample. The coercivities are expected to match, but the simulated loop will be a bit more sheared due to how the grain distributions are modeled (more detail in section 4.5). Note that for the experimental hysteresis loops, all of the magnetization values have been normalized to their corresponding saturation magnetization values. All coercivity values for the simulated and experimental loops can be found in table 4.3.

4.4.1 Hysteresis loops of a $(Co_4Pt_7)_3$ thin film

Looking at figure 4.2, the simulated hysteresis loop is more sheared, while the experimental hysteresis loop appears to be nosier, especially around the parts where the sample is saturated. The reason for the noise arises from measurement uncertainties not modelled by the simulator, and possible domain-wall effects that were not taken into account. The experimental coercivity value matches the simulated coercivity. Possible reasons for mismatches in loop shape include: lack of thermal stability of the grains at room temperature during the experiment, and an incorrect modeling of the anisotropy field with respect to the grain size.

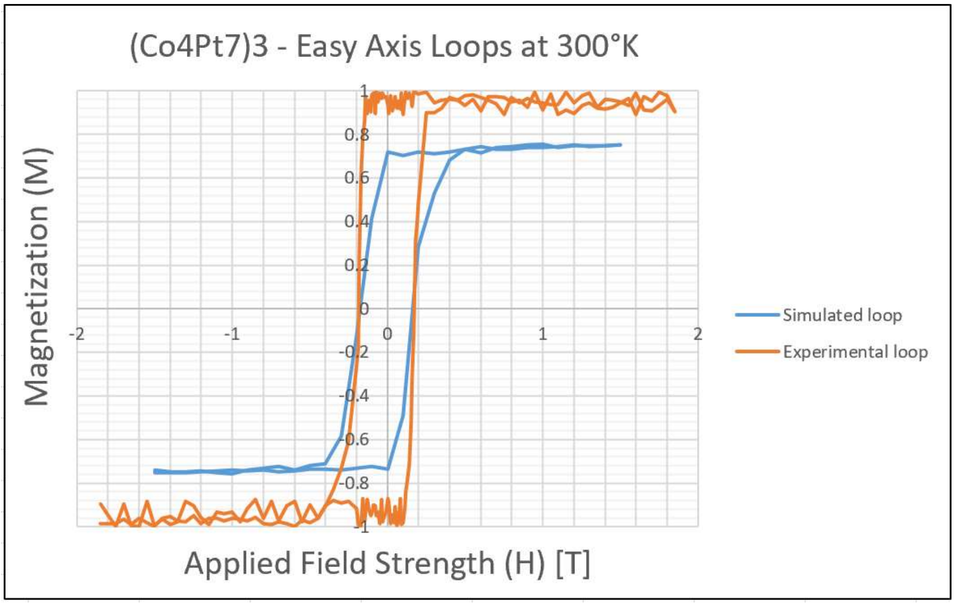

Fig 4.2. Easy axis loops of a $(Co_4Pt_7)_3$ particle produced at 300°K.

4.4.2 Hysteresis loops of a $(Co_4Pt_7)_{12}$ thin film

Looking at figure 4.3, the simulated and experimental coercivity seem to match. Similar to figure 4.2, the simulated hysteresis loop is still sheared, albeit not as significantly, which is expected because the volume and coercivity of this sample are significantly larger than that of $(Co_4Pt_7)_3$. Additionally, there is a lot less noise present within the experimental loop. This implies that this sample is more thermally stable than the $(Co_4Pt_7)_3$ sample.

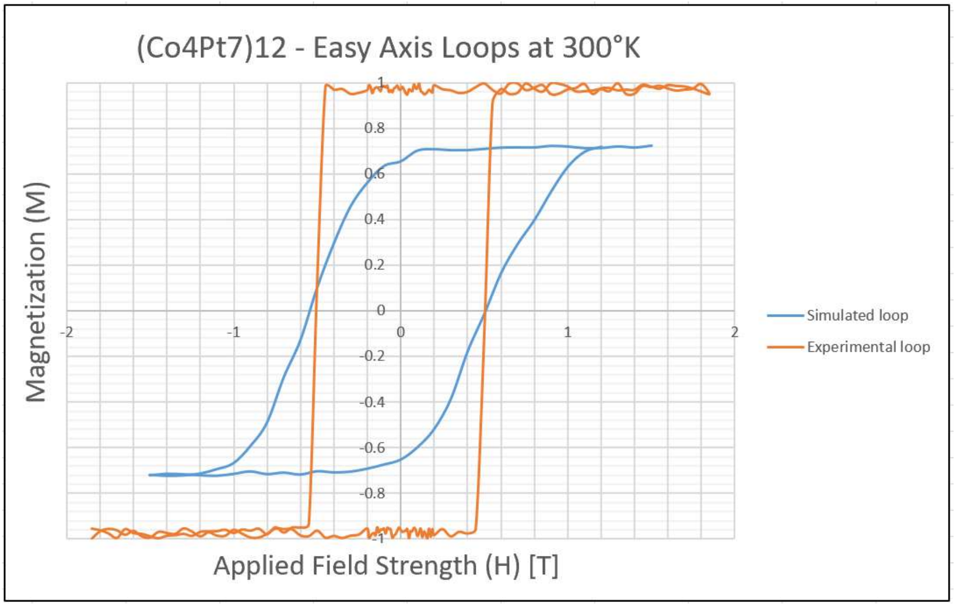

Fig 4.3. Easy axis loops of a $(Co_4Pt_7)_{12}$ particle produced at 300°K.

4.4.3 Hysteresis loops of a $(Co_4Pt_{11})_{12}$ thin film

Looking at figure 4.4, there is less shearing found in the simulated $(Co_4Pt_{11})_{12}$ loop, meaning that the simulated grain size distributions and the anisotropy field modelling seem to match the experimental values. A possible reason for this could be that the grain thickness for this sample is the largest out of all the others. The coercivity of the simulated loop is slightly larger than experimental loop, and the noise from the experimental loop is similar to that of the experimental loop found in figure 4.3.

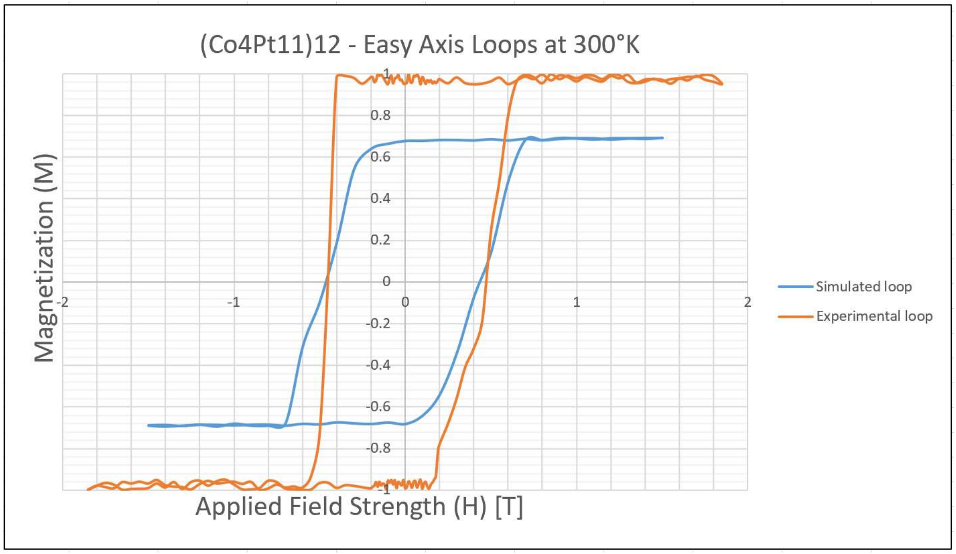

Fig 4.4. Easy axis loop of a $(Co_4Pt_{11})_{12}$ particle produced at 300°K.

4.4.4 Hysteresis loops of a $(Co_6Pt_6)_{12}$ thin film

Looking at figure 4.5, the simulated and experimental hysteresis loops seem to look very similar to figure 4.4, albeit a bit noisier. This indicates that both $(Co_4Pt_{11})_{12}$ and $(Co_6Pt_6)_{12}$ obey a similar grain size distribution and anisotropy model. This makes sense, as they both have similar grain sizes (thickness and diameter), and the same anisotropy field value. Looking at table 4.3, the coercivity values for the simulated and experimental hysteresis loops seem to match.

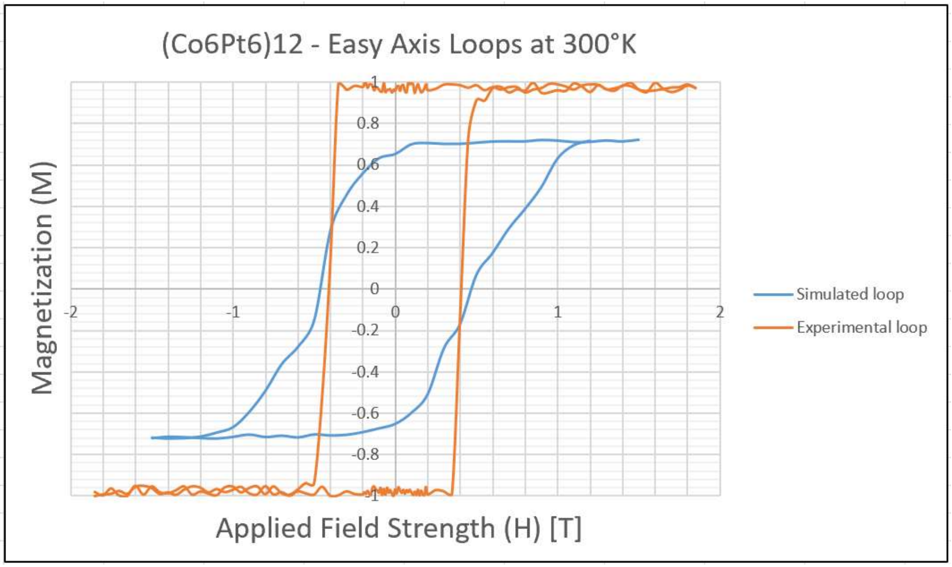

Fig 4.5. Easy axis loop of a $(Co_6Pt_6)_{12}$ particle produced at 300°K.

4.5 Switching probability analysis and summary of results

Once the Curie temperature values and hysteresis loops for each sample matches the theoretical values and experimental results, the switching probability can be calculated. Judging from table 4.3, the simulated and experimental coercivity values seem to match, but the simulated hysteresis loops seem more sheared and have a lower remanent magnetization (lower magnetization at zero applied field), particularly for the case of $(Co_4Pt_7)_3$. Possible reasons for this could include: incorrect modelling of the anisotropy field differences in the grain size and their distribution between the experiment and simulation. Slight differences in coercivity values come from experimental errors found from experimental methods when obtaining values for T_c, M_s and K_u (around ±10% error). The $(Co_4Pt_7)_3$ sample has the smallest overall volume and a relatively low coercivity, so the grain size distribution of this thin-film will contain the highest probability of yielding grains that are not thermally stable at room temperature and a less remnant loop. Afterwards, the switching probability is calculated by computing a thermal cooling simulation that cools a Co-Pt sample that is initially at a temperature that's $50^{\circ}K$ higher than its Curie temperature down to a room temperature (~$300^{\circ}K$). This is done at a given applied magnetic field, magnetic field angle with respect to the film anisotropy axis and given cooling rate. Afterwards, a plot between temperature and the total magnetization projected along the z-axis is plotted, which is indicative of how many grains end up with spin up or down. More details about this procedure can be found in chapter 5. Overall, a sample with a high J_{ij} value, along with a larger volume and coercivity will yield grains that are more thermally stable at higher temperatures, making it easier to set spins to their desired state.

Table 4.3: Comparison of experimental and simulated coercivity values

Particle type	**Experimental H_c [T]**	**Simulated H_c [T]**
$(Co_4Pt_7)_3$	0.18	0.18
$(Co_4Pt_7)_{12}$	0.50	0.55
$(Co_4Pt_{11})_{12}$	0.46	0.48
$(Co_6Pt_6)_{12}$	0.45	0.48

4.6 Chapter 4 Summary

This section covers how the thin films were designed, and compared with experimental values. The same values for K_{ui}, μ_s and J_{ij} from table 3.3 were used. Note that $(Co_4Pt_7)_3$ and $(Co_4Pt_7)_{12}$ are composed of the same type of particle. The only difference from the simulations performed in chapter 3 is the additional layer of complexity added – instead of working with single particles, cylindrical grains composed of many Co-Pt atoms are now being analyzed. Therefore, the grain size, spacing and dimensions of the thin film have to be chosen. The number of grains present on a thin film, which determines the switching probability precision, is increased by increasing the x and y-dimensions of the thin film. The z-dimension is obtained from the total thickness of a given sample from our lab. Afterwards, the Curie temperature vs. magnetization plots and easy-axis hysteresis loops for each sample was analyzed. Looking at table 4.2, although $(Co_4Pt_7)_3$ and $(Co_4Pt_7)_{12}$ have the same J_{ij} value, $(Co_4Pt_7)_3$ has the higher Curie temperature value due to its larger particle size. This indicates that the grain size has a stronger affect on the Curie temperature than the J_{ij} value. Looking at figures 4.2 – 4.6, the shape of the simulated easy axis hysteresis loop does not match the experimental loop due to inconsistencies in the grain size distribution, Samples with a large grain size and coercivity value will be more thermally stable, making them easier to switch.

CHAPTER 5: HAMR switching probability analysis of Co-Pt thin-films

5.1 Overview

The long-term success of HAMR-based systems are determined by the switching probability – what is the probability that a spin state of a grain will successfully switch to its desired state [89]? This behaviour becomes more unpredictable at higher temperatures due to the gain in thermal fluctuations of the spins within a small grain. These fluctuations randomize the spin states and work against the applied field that is used to set the spins in the desired state. Time is also a factor – the longer the switching process, the more time the spins have to re-align themselves into new switching states. If the temperature is too low, the thermal fluctuations will be small, but the energy barrier between the states set by K_u may be too high for the applied field to overcome. However, if the temperature of a material is increased beyond the Curie point of a material, the K_u value becomes zero due to the excess amount of thermal fluctuations that randomize the spin states, making it unclear which spin configuration is the equilibrium state. Although this makes the spins easily writable, the thermal fluctuations will be too high for any stable configuration to be produced, making the spins unwritable. The desired spin configuration could be set once the spins are cooled down to room temperature in the applied field [3]. As a result, there is a chance the switching probability could improve, depending on how the material is heated and cooled down. Additional factors that impact the switching probability include: the ratio between the amount of cobalt and platinum in a given sample (which determines the magnetic properties), and the magnitude and direction of the applied magnetic field. As mentioned in chapter 1, there are not many studies regarding the spin dynamics at higher temperatures, so it is best to perform a thorough study of how the spin dynamics affect the switching probability at higher temperatures.

5.2 Modeling set-up

To test the switching probability, a field cooling routine of the VAMPIRE simulator will be used. In this work, the light-matter interaction is not directly modeled, so the HAMR laser pulsing effect is modeled by specifying the temperature of the system and the cooling rate, along with the applied field strength. The maximum and minimum allowable temperature (T_{max} and T_{min}, respectively) of the simulation can be chosen [90], as well as the equilibration temperature (T_{eq}), which represents the temperature at which the material is initially set at. For this work, the maximum temperature will be set to a temperature that is $50^{\circ}C$ higher than the sample's Curie temperature, and the equilibration/starting temperature will be set to that as well. The reason why a temperature that is $50^{\circ}C$ higher than the sample's Curie temperature is used is to ensure the spins in the sample start from a well-randomized state (the erased state) before the writing attempt is made [34]. The minimum temperature will be set to room temperature (T_{room}), as that is the typical temperature at which most HDD's operate. A flow-chart of the workflow model can be seen in figure 5.1.

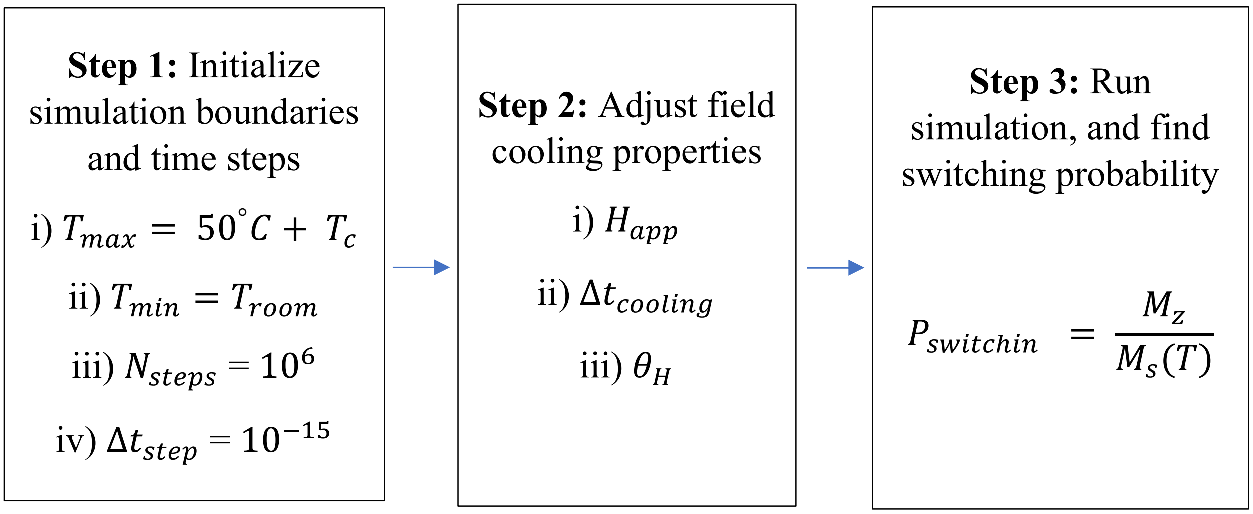

Fig 5.1. A flow-chart of the thermal ramping experiment. Details about how to obtain the switching probability (step 3) can be found in section 5.3.

$\Delta t_{cooling}$ refers to the cooling time, H_{app} refers to the applied magnetic field strength and θ_H refers to the applied magnetic field angle (with respect to the *z*-axis, also known as the anisotropy direction). More details regarding these variables can be found in section 5.5. The switching probability is defined as the ratio between the magnetization in the *z*-direction (M_z) and the maximum possible magnetization at a given temperature ($M_s(T)$). A field cooling simulation works by cooling the sample down until the minimum allowable temperature has been reached. The amount of time to reach the minimum temperature, which can be adjusted by either changing the amount of timesteps (N_{steps}) or the duration of each timestep (Δt_{step}), drastically affects the results of the simulation. The number of timesteps is proportional to the time it takes to run a simulation, meaning that it will take a longer time to reach the minimum temperature. Additionally, the thermal fluctuations are different at each time step, meaning that the magnetization dynamics will be different at each time step [89]. This means that the switching probability is dependent on how long each time step is, and the number of steps within a simulation. Therefore, it is best to pick values that do not shorten the simulation time for computational efficiency, but rather use realistic values for the total time steps and the time step duration: 10^6 and 10^{-15} s, respectively. The reason why the time step of 10^{-15} s was chosen was explained in chapter 2, whereas using 10^6 time steps sets the cooling rate $\frac{dT}{dt}$ to a value (order of $100\ \frac{°K}{ns}$) to ensure the cooling rate of a nanosecond laser pulse acting on a Co-Pt sample is accurately modelled [91], since

$$\frac{dT}{dt} = \frac{T_{max} - T_{min}}{\Delta t_{step} N_{steps}} \tag{5.1}$$

Changing N_{steps} allows the user to change the cooling rate without compromising by setting a larger value for Δt_{step}. The number of time-steps where detailed information pertaining to the magnetic moments are saved can be chosen by the user.

5.3 Obtaining the switching probability

With this information, the switching probability can be calculated by dividing the magnitude of the total magnetization in the z-direction (direction of the applied field) by the saturation magnetization at a given temperature, which represents the maximally attainable spin-alignment at that temperature. In other words, if the moment in the z-direction at the end of a field cooling experiment matches the saturation magnetization, the writing probability is 100%, since all grains point in the desired direction. The equation for the switching probability at a given temperature can be seen below:

$$P_{switching} = \frac{proj_{\boldsymbol{H}_{app}}\boldsymbol{M}}{M_S(T)} = \frac{M_z}{M_S(T)} \tag{5.2}$$

The above equation will be used for both section 5.3.1 and 5.3.2, with the only difference being how $M_S(T)$, also known as the saturation magnetization as a function of temperature, is obtained. M_Z refers to the magnetization in the z-direction (same direction as $\boldsymbol{H}_{app}$). Due to thermal fluctuations, the saturation magnetization in the easy-axis loop sets the maximum magnitude in the z-direction, which is always going to be less than 100% (obtained only at $0^{\circ}K$). The z-direction is also the anisotropy direction (the typical switching axis, as stated in section 1.2 of this thesis). It is important to note that dipolar effects will be ignored for this simulation, as they did not affect the coercivity of the saturation as much (a visualization and analysis of this effect can be seen in section 2.5.4).

5.3.1: Obtaining the saturation magnetization at $300°K$

The saturation magnetization at $300°K$ for a given sample is obtained from looking at the simulated easy axis hysteresis loops found in section 4.4, and finding the saturation magnetization value. [89]. Afterwards, equation 5.2 is used. A hysteresis loop is preferred over a Curie temperature graph because it shows the total moment in the presence of the applied magnetic field (the moment can be a function of the applied field if the sample does not have 100% magnetic remanence, which is also known as the magnetic field retained at zero applied field). However, this is not always the most efficient method.

5.3.2: Obtaining the switching probability at other temperatures

Since data regarding hysteresis loops at temperatures aside from $300^{\circ}K$ are not provided, a Curie temperature simulation for a given sample will be used instead, as this simulation provides the maximally attainable magnetic field at any given temperature. In equation 5.2, $M_s(T)$ will now be equal to $(1-\frac{\mathrm{T}}{\mathrm{T_C}})^{\frac{1}{3}}$, meaning that:

$$P_{switching} = \frac{proj_{\boldsymbol{H}_{app}}\boldsymbol{M}}{(1-\frac{\mathrm{T}}{\mathrm{T_C}})^{\frac{1}{3}}} \tag{5.3}$$

5.4 Obtaining the blocking temperature

When the magnetization is sufficiently set in the desired state, one can define the medium as having been written into. It is interesting to examine the point in time when this takes place. During a cooling process, this condition may also be interpreted as the temperature at which the magnetization reaches the desired set point, and is blocked due to the inability of the magnetization to further switch at lower temperatures. The threshold for writing is somewhat arbitrary – in this work, the temperature at which the switching probability reaches 90% is going to be used as the blocking temperature. Unfortunately, since VAMPIRE only lists magnetization values relative to the maximum possible value (the magnetization at $0^{\circ}K$), finding the blocking temperature becomes a challenge, as the magnetization changes at different temperatures [92]. Therefore, in order to find the blocking temperature, equation 5.3 will be used, and the temperature that gives a value of 90% will be the blocking temperature. When this fraction becomes 90% or greater, the blocking temperature has been reached. This method of finding the blocking temperature will be relevant for section 5.4.2, as this will help find the switching probability at different temperatures.

5.5 Simulation plan

The simulations will start with the applied magnetic field strength (H_{app}) being set at 0.1 T, cooling time ($\Delta t_{cooling}$) at 50 ps, and the magnetic field angle at

0° for each of the samples being studied. Starting with these values means there will be a small probability of switching the grains, since the applied field is small and the cooling rate is fast. The applied magnetic field strength will be increased in 0.1 T increments until a 90% switching probability is reached. The switching probability has been set arbitrarily, but it represents the threshold for a successful switching event. The cooling rate will be increased to 100 ps and the simulations as a function of the applied field are repeated, then in increments of 100 ps until 400 ps is reached. This will relax the requirements for the applied magnetic field, as slower cooling rates should result in successful writing events at smaller applied magnetic field values. The magnetization angle (θ_H), which was previously mentioned in section 5.2, will also be incremented by 15° until an angle of 60° is reached. For each simulation, the switching probability will be extracted by dividing the magnetization at $300°K$ by the saturation value of the sample. These set of simulations will be run on all of the four samples mentioned in section 4.1 of this thesis (three different Co-Pt ratios and two different multilayer thicknesses). In the worst-case scenario, there will be approximately 1000 simulations that will need to be performed (10 magnetic field values on average, 5 cooling rate values, 5 magnetic field angle values, 4 samples = $10 \cdot 5 \cdot 5 \cdot 4 = 1000$). Although there are a lot of simulations, each simulation takes approximately 35 minutes on average, resulting in a worst-case total of 24 days' worth of simulations if simulations are not run in parallel. Since up to four simulations can be run at once, the total amount of days gets divided by 4, meaning that approximately 6 days will be required to complete all of the work if simulations were to be run throughout the entire day.

5.6 Theoretical and experimental analysis of results

In this section, the theoretical effect of each parameter mentioned in this section on the switching probability will be mentioned and compared to the simulation results.

5.6.1 Applied magnetic field (Write Field)

By increasing the applied magnetic field, a stronger bias towards a given direction is applied, which gives the magnetic spins more "guidance" to fight against the thermal fluctuations experienced near the Curie temperature and point in the proper direction [13]. This implies that a higher applied magnetic field is responsible for a higher switching probability. However, as there is a limit on how high the applied magnetic field can be (~2 Tesla) due to the material-based limitations of the electromagnet used in HAMR-based systems [5], lower write field values are preferred. If a sample requires a smaller magnetic field to reach a 90% switching probability, then the sample probably has a low K_u value (ex: $(Co_4Pt_{11})_{12}$ and $(Co_6Pt_6)_{12}$). The lower K_{ui} helps in this respect as it lowers the field required to overcome the anisotropy of the sample. On the other hand, this is not helpful in HDDs as a low K_{ui} may not support high recording densities as smaller grains will not be thermally stable. To overcome this dilemma, other parameters pertaining to thermal stability could be improved on (more detail can be found within the next sub-sections). As seen in figure 5.2, the experiments support this claim.

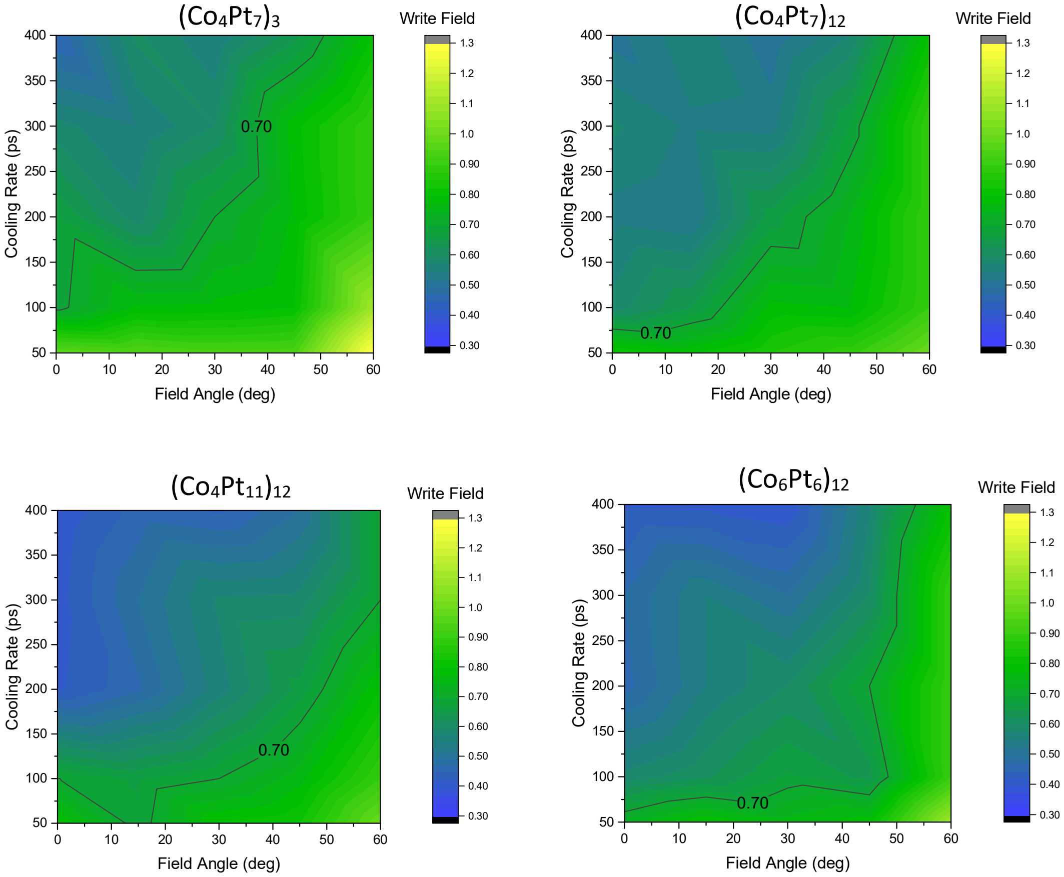

Fig 5.2. Magnetic field required to reach a switching probability of at least 90.0% for a given field angle and cooling rate. The contour labeled with “0.70” represents the magnitude of the write field (in Teslas).

5.6.2 Cooling time

By increasing the time it takes for the medium to cool after a heat pulse, the switching probability will increase, as the magnetic spins will have time to re-configure themselves into the lowest energy state [66]. In other words, a lower magnetic field is required to write into the system if the spins are already aligned into the lowest energy state, meaning that a higher cooling time implies a lower required write field. This is analogous to freezing a glass too quickly; an amorphous structure will develop. As seen in figure 5.3 the simulations support this claim, as a higher pulsing period almost always implies a lower writing field required to attain a 90% switching probability. According to the results in figure 5.2, materials with a lower K_u tend to require a lower applied magnetic field to reach a switching probability of 90% for a given cooling rate, meaning that these materials have a tendency to reach a more desirable spin configuration at a faster rate (ex: $(Co_4Pt_{11})_{12}$ and $(Co_6Pt_6)_{12}$). This observation is helpful in the light of the fact that materials with a higher K_u required a larger magnetic field to write into – this requirement can be relaxed if it is acceptable to have a longer writing time, which depends on the required bit rate and length of a given HDD system.

As seen in figure 5.3, a higher cooling time implies a higher blocking temperature to Curie temperature ratio, implying that the system “freezes” to the desired spin state earlier on during the simulation. Blocking temperatures (T_B) are normalized to their Curie temperature because each sample has a different Curie temperature, which drastically impacts the value of T_B. Since $(Co_4Pt_7)_{12}$ is the only material with a $\frac{T_B}{T_C}$ value that reaches 1, this means that the material can be written at temperatures very close to the Curie temperature. A possible reason for this could be that the system already has enough time to reach the optimal spin configuration, so the spins do not need to re-adjust themselves any further. As a result, the spin configuration “freezes” earlier on during the simulation at a higher temperature, which is supported by our simulations. This is an interesting aspect considering that writing in HAMR HDDs takes place as a hot spot moves across the medium. If the writing process takes place closer to the Curie temperature and is blocked soon below it, this implies that large areal densities could be recorded provided that a large thermal gradient across the medium area can be provided by the laser source, somewhat independently of how quickly the temperature is lowered. With a medium that favours higher thermal gradients for writing, the writing precision can be improved because more heat is concentrated within a smaller point, making it possible to target smaller grains individually and make them more susceptible to the writing field. Note that as the grain size decreases, then the magnetic spin becomes more unstable due to increased effect of thermal fluctuations on the spin state. If the thermal gradient is too small relative to the blocking temperature, the bit precision would not be as good due to the lack of sharpness in spin state transitions, as the laser used by HAMR makes the magnetization of the grains more susceptible to the write field [3]. On the other hand, the $(Co_6Pt_6)_{12}$ sample, which looked promising in terms of low writing field requirements, has a $\frac{T_B}{T_C}$ ratio that is generally much lower and therefore is not as conducive to supporting high-density recording.

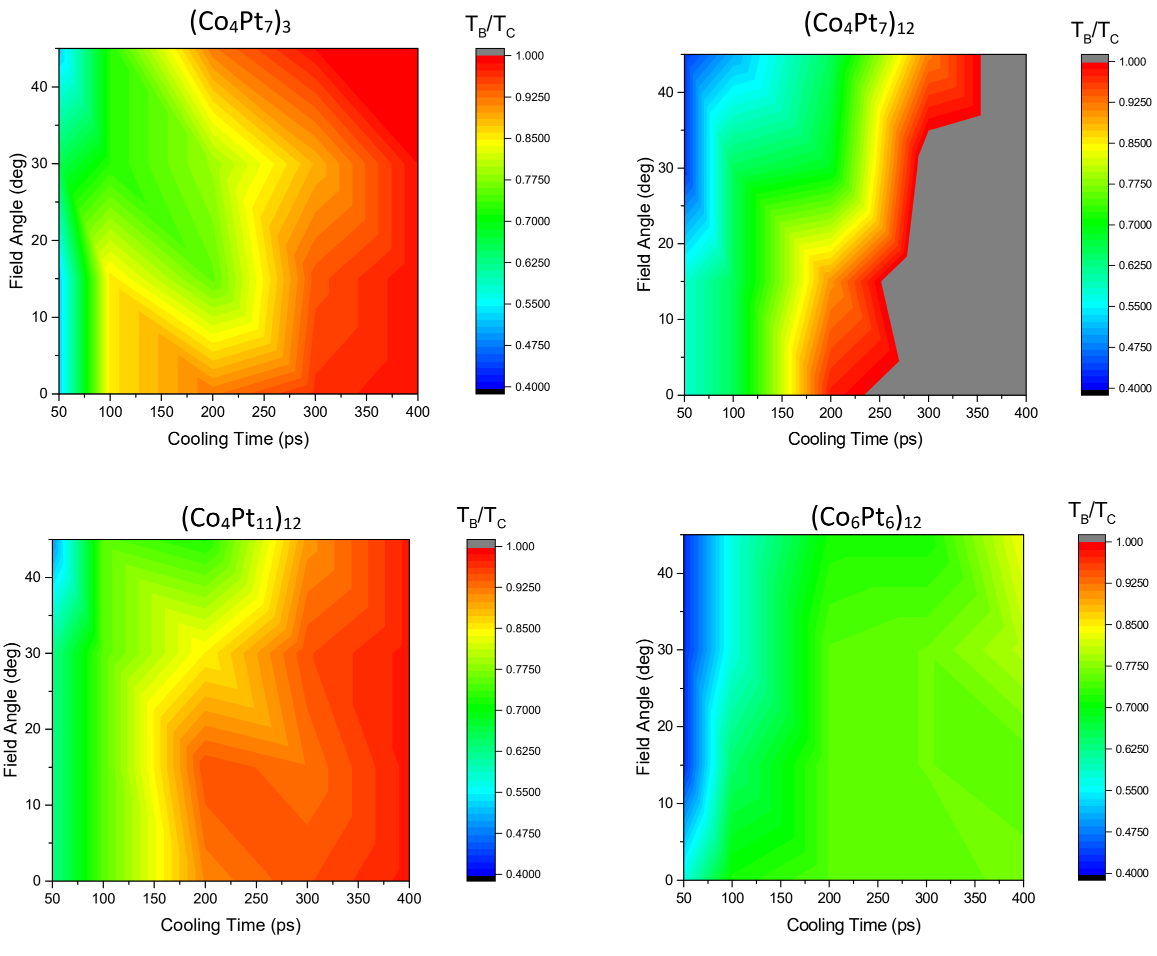

Fig 5.3. Graph representing how the sample composition and thickness, field angle and cooling time impact the ratio between the blocking and Curie temperature.

5.6.3 Applied field angle (θ_H)

The angle at which the magnetic field is applied onto the sample relative to the anisotropy direction (θ_H) affects the magnetic torque of the spins. Since the damping factor is not zero, the spin will always want to return to its lowest energy position, which produces a magnetic torque. Therefore, there exists an optimal angle at which the torque is highest and directs the spin towards the desired orientation as efficiently as possible. If θ_H is too high, then the magnetic spins will reach a configuration where the *z*-component of the magnetic spin points "up" or "down" with similar probabilities [48]. On the other hand, if θ_H is too low, then not enough torque will be produced for writing, meaning that a higher magnetic field will be required. According to the results from figure 5.2, it is evident that a value of θ_H less than 20 degrees seems to be the optimal value when looking at the $(Co_4Pt_7)_3$ and $(Co_4Pt_7)_{12}$ graphs. For the other two graphs, it seems that an angle less than 45 degrees is optimal. This indicates that the materials with the lower K_u value switch with a higher θ_H. The reason for this is not clear beyond the argument made in the next section regarding the torque (i.e. less torque at the blocking temperature indicates the spins have stabilized in the desired direction). This is an important finding, since the magnetic field angle acting on the magnetic medium in a HAMR HDD cannot have angles near perpendicular, due to the difficulties of collocating the near-field transducer that heats the medium and the magnetic pole that provides the applied field. Therefore, magnetic media that can switch more easily at larger field angles (ex: $(Co_4Pt_{11})_{12}$ and $(Co_6Pt_6)_{12}$) are desirable.

5.6.4 Magnetic Torque

The magnetic torque produced at the blocking temperature is typically what causes all of the writing to spins happens, as this is where the magnetic torque is at its highest value before the magnetization freezes (recalling equation 1.5 of section 1.9, the torque is proportional to the magnetization, which increases with decreasing temperature). Typically, the higher the magnetic torque, the stronger the force of the applied field influencing the spins. On the other hand, if this torque value is too high, then the torque will cause spins to precess longer, which could lead to writing instability issues. Therefore, from a theoretical perspective, there is an ideal amount of torque required, depending on the details of the spin dynamics. As the torque is a vector quantity, the applied field angle also impacts the torque, as the torque is a cross product between the applied field direction and the spin's magnetization direction. Looking at figure 5.4, it seems that materials with a lower K_u (ex: $(Co_4Pt_{11})_{12}$ and $(Co_6Pt_6)_{12}$) tend to have a lower torque at the blocking temperature, which somewhat surprisingly are the materials that are easier to switch. On the other hand, the torque at the blocking temperature appears to be the highest at higher field angles, which is a more demanding switching condition associated with smaller switching probabilities, as magnetic media capable of switching at large field angles and lower applied magnetic fields are desirable. This might indicate that if the torque is substantial at the blocking temperature, the switching dynamics that minimize the energy of the system are not finalized and the probability of freezing the spins into the desired state is lower. Therefore, it is possible that writing happens at a lower temperature in a field cooling simulation.

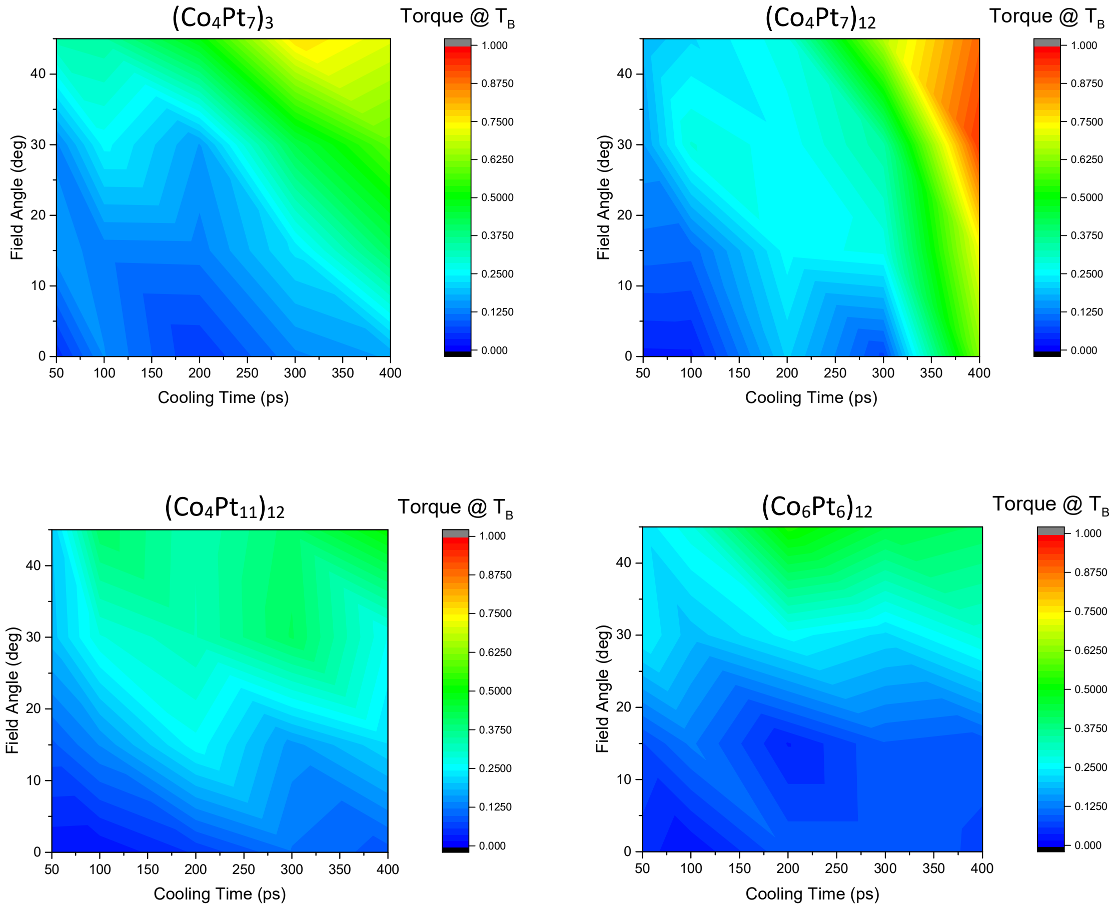

Fig 5.4. Magnetic torque at the blocking temperature for a given sample under a different magnetic field angle and cooling time.

5.6.5 Alloy type

By having a higher composition of cobalt within the sample, the μ_s value increases due to ferromagnetic nature of this material [18]. On the other hand, since platinum is not a ferromagnetic material, having a higher concentration of platinum will reduce the μ_s value. This can be verified when looking at table 5.1 - $(Co_6Pt_6)_{12}$ has the highest composition of cobalt, thereby having the highest μ_s value (refer to table 5.2). With regards to the K_u value, the anisotropy originates from the fact that platinum becomes partially magnetic at the interface between cobalt and platinum due to induced magnetism [18]. Therefore, the K_u value is proportional to the number of interfaces there are per unit length, which depends on the number of layers present within a sample.

Table 5.1: Summary of calculation results pertaining to the number of interfaces per unit length

Sample Type	Number of Interfaces	Thickness $[nm]$	Interfaces per unit length	$K_{ui}\left[\frac{J}{atom}\right]$
$(Co_4Pt_7)_3$	5	3.3	1.515	$3.131 \cdot 10^{-23}$
$(Co_4Pt_7)_{12}$	23	13.2	1.742	$3.131 \cdot 10^{-23}$
$(Co_4Pt_{11})_{12}$	23	18	1.278	$2.761 \cdot 10^{-23}$
$(Co_6Pt_6)_{12}$	23	14.4	1.597	$2.721 \cdot 10^{-23}$

The number of layers is represented by the subscript c in $(Co_aPt_b)_c$. Each sample has $2c-1$ interfaces, a thickness of $\frac{(a+b)c}{10}$ nm, and $\frac{2c-1}{[\frac{(a+b)c}{10}]}$ interfaces per nanometer. These values for each sample can be seen in table 5.1. However, due to interfacial roughness effects mentioned in section 3.4.2, the interfaces per unit length results seen in table 5.2 do not proportionally scale with the value of K_u, as the material with the fewest interfaces per unit length does not have the lowest K_u value. Lastly, with regards to T_C, as platinum has a Curie temperature of $0°K$, while Cobalt has a very high Curie temperature. As a result, the Curie temperature increases in proportion to the percentage composition of Cobalt, since an effective medium model is being used. An effective medium model practically mixes the atoms into one material, so more cobalt present within the sample implies more cobalt-like behaviour within the sample. Looking at table 5.2, with the exception of $(Co_4Pt_7)_3$ and $(Co_6Pt_6)_{12}$, it seems that an increase in the concentration of Cobalt implies a higher Curie temperature. Possible reasons for the exception experienced between $(Co_4Pt_7)_3$ and $(Co_6Pt_6)_{12}$ could come from surface atoms present in $(Co_6Pt_6)_{12}$. Since those atoms do not contribute to the exchange interaction, J_{ij} will be lower, thereby reducing the Curie temperature of the sample. Therefore, the composition, number of interfaces, and thickness of the sample affect the T_C, K_u

and μ_s values, which affects the switching probability, $\frac{T_B}{T_C}$, and freezing time as seen in figures 5.2, 5.3 and 5.5, respectively.

Table 5.2: Summary of all material properties of each sample

Sample Type	Composition	T_C (°K)	$K_{ui}\left[\frac{J}{atom}\right]$	μ_s $(at\ 0^{\circ}K)$
$(Co_4Pt_7)_3$	Co: $\frac{2}{5}$ Pt: $\frac{3}{5}$	754.57	$3.131 \cdot 10^{-23}$	$1.246\mu_b$
$(Co_4Pt_7)_{12}$	Co: $\frac{2}{5}$ Pt: $\frac{3}{5}$	685.28	$3.131 \cdot 10^{-23}$	$1.246\mu_b$
$(Co_4Pt_{11})_{12}$	Co: $\frac{2}{7}$ Pt: $\frac{5}{7}$	605.85	$2.761 \cdot 10^{-23}$	$0.983\mu_b$
$(Co_6Pt_6)_{12}$	Co: $\frac{1}{2}$ Pt: $\frac{1}{2}$	695.50	$2.721 \cdot 10^{-23}$	$1.32\mu_b$

5.6.6 Blocking temperature

As a field-cooling simulation starts off above T_C, then ends at room temperature ($300^{\circ}K$), a higher blocking temperature implies that the sample "freezes" at a particular spin state configuration sooner [90]. Depending on whether the spins had sufficient time to align themselves along the applied field direction, the sample may be stuck in a non-optimal spin state, meaning that a higher magnetic field or cooling time will be required to attain a 90% switching probability. Therefore, a lower blocking temperature is typically better to obtain a higher chance of writing, as the spins have more time to re-configure themselves into a more energetically favorable configuration. On the other hand, low blocking temperatures, and consequently longer switching times, will result in a medium that is limited in terms of how quickly information can be written on it, therefore limiting data transfer rates. According to the results in figure 5.2 and 5.3, it seems that a lower blocking temperature implies that less magnetic field and a cooling time is required to attain a 90% switching probability, meaning that the system is more robust to thermal fluctuations. In other words, materials with a lower K_u tend to have lower $\frac{T_B}{T_C}$ values, meaning that a lower $\frac{T_B}{T_C}$ value is typical for materials that are easier to switch. Additionally, when looking at figure 5.5, these materials require more time to reach a stable configuration state, with $(Co_6Pt_6)_{12}$ being the worst performer. Conversely, $(Co_4Pt_7)_3$ is the fastest switching material, but it is the most difficult to write into. One should keep in mind that with figures 5.3-5.5, which involve the use of the blocking temperature, the magnetic field is kept at 1 Tesla. Therefore, nothing explicit can be said about the impacts on the effect on blocking temperature by adjusting the applied magnetic field, since the blocking temperature depends on the applied field. However, it can be inferred that a higher magnetic field will imply a higher blocking temperature (assuming that the field is applied at an angle less than 30°), as by adding a larger bias, the spins can be forced into the lowest energy state earlier on during the simulation. Therefore, the limited switching probability and fast writing speed observed for $(Co_4Pt_7)_3$ can be balanced by a larger writing field. Similarly, a larger writing field should cause the easier to switch material, $(Co_6Pt_6)_{12}$, to be able to switch at shorter time scales.

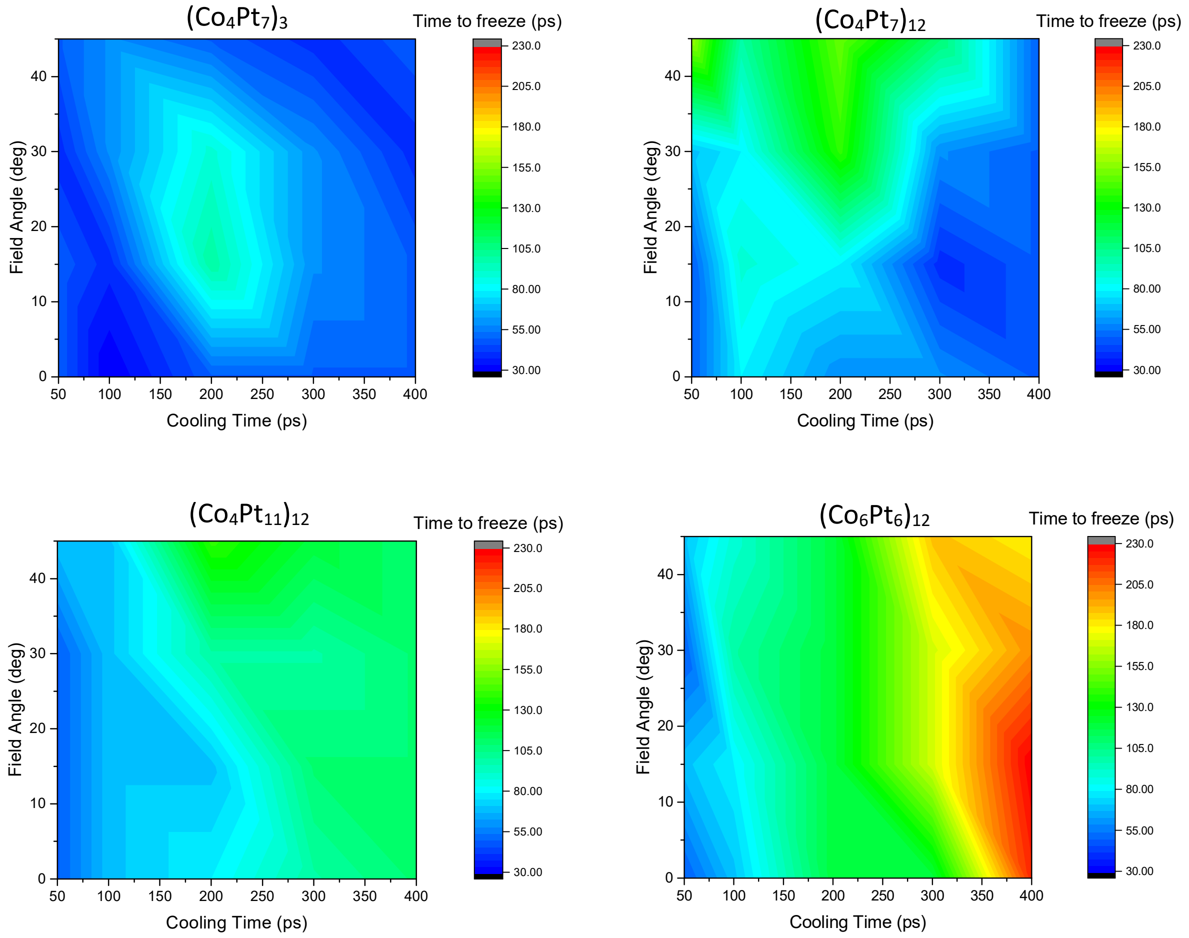

Fig 5.5. A visualization of how long it takes for a sample to reach the blocking temperature (when the spin states are “frozen” to a specific configuration) under a given field angle and cooling time.

5.6.7 Grain Thickness and Particle Size

In this case, the number of layers, represented by the subscript c in $(Co_aPt_b)_c$, is adjusted by changing the value of “*c*” of the thin-film. However, since an effective medium model is used, the ratio to cobalt and platinum will be the same amongst samples with the same cobalt and platinum concentration (refer to table 3.1), but with different numbers of layers [85]. This is because when an effective medium model is used, only one type of atom containing both properties of cobalt and platinum is used, meaning that the various types of interactions that occur between cobalt and platinum particles, along with interlayer effects, are ignored. Now, as each layer is composed of the same type of atoms, the number of layers now represents the height of each grain, also known as the grain thickness. As a result, the anisotropy and saturation magnetization values will be the same for $(Co_4Pt_7)_3$ and $(Co_4Pt_7)_{12}$. If we ignore dipolar interactions, the only difference that will exist between samples with the same Co and Pt concentrations is the Curie temperature. By increasing the *z*-dimension of the film, the height of the grain increases, thereby increasing the volume more so than the surface area. Note that grains are modelled as cylinders. This results in a decrease in the surface area to volume ratio – a higher surface area to volume ratio will typically yield a lower Curie temperature due to the presence of more atoms residing at the surface of the thin-film [36]. However, recall that the particle diameter was adjusted to match the coercive field of the samples, meaning the Curie temperature will be affected due to this reason as well. The result in our case is that $(Co_4Pt_7)_3$ is composed of thinner grains, but has a lower surface area to volume ratio and larger T_C. This implies that the particle size of a material has a stronger effect on J_{ij} than the surface area to volume ratio and the grain thickness. This can be seen when realizing the following size discrepancies between $(Co_4Pt_7)_3$ and $(Co_4Pt_7)_{12}$ in table 5.3: the difference in thickness (z-dimension length) is 9.9 nm ($(Co_4Pt_7)_{12}$ being the thicker sample), the difference in particle sizes is 2.7 nm ($(Co_4Pt_7)_3$ being the sample with larger particle sizes). Despite having a smaller difference in particle size, $(Co_4Pt_7)_3$ still has a noticeably higher Curie temperature. This implies that more atoms reside on the surface of a $(Co_4Pt_7)_{12}$ film, which reduces the Curie temperature of the sample. This makes sense, as a smaller particle sizes implies that the atoms are more likely to reside around the surfaces of a thin-film. Additionally, when looking at figure 5.3, it can be seen that the blocking temperature of the $(Co_4Pt_7)_{12}$ sample is near the Curie temperature – implying that the anisotropy of the material changes at a slower rate than the saturation magnetization value with respect to temperature [90]. Therefore, increasing the particle size of a material has a more prominent effect on increasing J_{ij} than increasing the grain thickness, but a high $\frac{T_B}{T_C}$ ratio implies a slower change in magnetic properties with respect to temperature.

Table 5.3: Summary of all dimensional properties of each sample. Note that the surface area to volume ratio formula for a cylindrical grain is $\frac{2(\frac{d}{2}+t)}{\frac{d}{2}t}$.

Sample Type	Surface Area to Volume ratio $[nm^{-1}]$	Particle diameter (*d*) $[nm]$	Grain thickness (*t*) $[nm]$	Curie Temperature $[°K]$
$(Co_4Pt_7)_3$	1.41	5.0	3.3	754.57
$(Co_4Pt_7)_{12}$	1.89	2.3	13.2	685.28
$(Co_4Pt_{11})_{12}$	1.59	2.7	18.0	605.85
$(Co_6Pt_6)_{12}$	1.87	2.3	14.4	695.50

5.7 Chapter 5 Summary

This chapter covers the methodology used to obtain the switching probability and blocking temperature of a given sample under a given temperature range, timestep number and duration, cooling rate, field angle and write field (applied magnetic field). Section 5.5 covers how the simulations were planned out in attempts to strike a balance between accuracy and time efficiency. Afterwards, the switching probability (figure 5.2), blocking to Curie temperature ratio ($\frac{T_B}{T_C}$, figure 5.3), magnetic torque at T_B (figure 5.4), and time taken to reach the blocking temperature (figure 5.5) were analyzed. Figures 5.2 and 5.3 indicate a trade off between switching probability and areal density by showing that materials with a high K_{ui} value tend to be harder to switch, but are able to be written into near the Curie temperature, thereby allowing for a larger thermal gradient for writing (high $\frac{T_B}{T_C}$ ratio). Figure 5.4 shows that writing may happen at a lower temperature because the torque value is not substantial enough (less than 0.9) for writing. Figure 5.5 indicates that materials with a low K_{ui} value tend to require more time to write into, indicating that issues with thermal stability are present. Sections 5.6.5 and 5.6.7 discuss trends in material properties of each sample based on sample's composition and thin-film dimensions, respectively. For high-density recording, a material is required to have a high $\frac{T_B}{T_C}$ ratio, large grain size and a high K_{ui} value.

CHAPTER 6: Conclusion

6.1: Contributions

This thesis provides a background of the developments of HDD's, theoretical approaches of modelling the magnetization dynamics at higher temperatures, and approximating the Co-Pt based multi-layer structure. Due to the lack of a model theory to guide HAMR developments, reaching the 10 $\frac{Tb}{in^2}$ requirement by 2025 is wishful thinking - it is 2024, and areal densities are in the 1– 2 $\frac{Tb}{in^2}$ range [93]. With Co-Pt based multi-layered structures, the concentrations of Co and Pt are allowed to be tuned, making it possible to see the effects of changing material parameters such as the anisotropy, saturation magnetization and Curie temperature on the switching probability of a given thin-film. The four samples in our lab, based on granular films of the multi-layers - $(Co_4Pt_7)_3$, $(Co_4Pt_7)_{12}$, $(Co_4Pt_{11})_{12}$ and $(Co_6Pt_6)_{12}$, were modelled using VAMPIRE – an atomistic simulator for magnetic materials. T_c, K_u, H_k, M_s and the sample dimensions were obtained from the literature, and H_c (tuned by adjusting the grain size) was obtained from past experiments from our lab. An effective medium and atomistic spin model were used to model the atomic properties and spins, respectively. The magnetization spin dynamics were modelled using the LLG equations, while neglecting dipolar effects, as they had negligible effects on the hysteresis loops. The bulk magnetic properties and the hysteresis loops of the thin-films were matched to the experimentally observed characteristics, then their switching probabilities as a function of simulation parameters such as the applied magnetic field value, applied field angle, and cooling were measured and calculated for each of the samples. A magnetic medium with a low K_{ui} and torque at T_B will make it easier to switch for smaller magnetic field strengths and larger field angles. This is necessary, as the magnetic field strength is limited to 2 Teslas, and the field angles are near perpendicular in an experimental setting. However, such magnetic media have a lower $\frac{T_B}{T_C}$ value and more thermal instability issues, which reduces the areal density and switching probability of the medium, respectively. Additionally, these materials require more time to write into due to their high freezing times. If a larger cooling time is allowed, then the areal density can be improved. Additionally, thermal instability issues can be fixed by increasing the medium's grain size and thickness, which increases the J_{ij} value. Therefore, good magnetic media typically have larger K_u values, as this increases the areal density and reduces the writing time of a given sample. If a material has a low K_u value, then issues with slow writing times and areal density can be improved by increasing the applied magnetic field and cooling time, respectively. Thermal instability issues can be fixed by increasing the grain size and thickness, regardless of K_u. The extensive analysis of Co-Pt based thin-films done in this thesis has helped with finding the ideal parameters a medium should have and be under to ensure maximal switching probability and maximal areal density, and a way to link theoretical findings with experimental results obtained from our lab through an effective medium model with the help of VAMPIRE.

Major Contributions

- Modeled an effective medium model that uses values from literature (T_c, K_u and J_{ij}) and experiments (H_c, film thickness and Co:Pt ratio) performed on samples from our lab with the use of VAMPIRE.

- Analyzed trends in switching probability and areal density in a way that strikes a balance between theoretical and experimental studies and trends.

Major Takeaways

- A magnetic medium with a low K_{ui} and torque will make it easier to switch for smaller magnetic field strengths and larger field angles.

- However, magnetic medium with a low K_{ui} tend to have a lower $\frac{T_B}{T_C}$ value, along with more thermal instability issues, which reduces areal density.

- There is not enough information to determine which medium is better for HAMR systems. A compromise between K_{ui} and $\frac{T_B}{T_C}$ must be investigated.

6.2: Future work

This thesis provides a foundation for future work in the areas of modelling and designing HDD’s in general, along with future research directions. Our research has provided a path to follow when it comes to choosing the proportions of cobalt and platinum – it seems that a higher concentration of platinum is typically better when designing Co-Pt-based thin-films, as that provides lower anisotropy values. However, if there is too much platinum in the sample, then the saturation magnetization value will be a bit too low, meaning that a higher applied magnetic field will be required and the readback signal of the HDD read sensor will be limited. Therefore, more studies could be done with regards to the switching probabilities of thin-films with higher platinum concentrations, including the modeling of the detected read signal to noise ratio.

With regards to modelling the structure and magnetization dynamics of the material, as explained in chapters 2-4, the geometry and parameters used to model the multi-layer is very simplistic. Additional details, such as the behavior between adjacent layers, and details about the magnetization at each atom, should be studied in greater detail in order to unravel more details regarding how magnetic torque and thermal fluctuations affect the sample. Such optimizations with the model may yield improvements to the fidelity of the simulations that affect the overall switching probability, and provide specific details with regards to how the multi-layer should be designed to maximize the K_u values. Our research has shown that by adding more multi-layers, the blocking temperature decreases, and the magnetic torque at the blocking temperature increases, which leads to more writing success. Therefore, to get more realistic data, and unravel more information about the thin-film and how it affects the switching probability, the experiments performed in chapter 5 could be repeated in the lab with the samples that were modeled here, and compared with the data obtained from this thesis. Alternatively, these models could be tested with the use of another LLB simulator, and differences in results can be compared, which could unravel more missing details without adding too many layers of complexity.

A possible experiment that could be performed to verify our results could involve setting up a simplistic laser and magnetic coil system to work on top of a Co-Pt sample from the HEATED lab. The cooling rate could be adjusted by using a modulator, and the field angle could be adjusted by co-locating the laser and magnetic coil alongside with each other. The temperature of a sample can be adjusted by changing the power of the laser pulse, or adjusting the cooling rate. Once the experimental apparatus has been set up, the magnetization within a given direction can be measured using a magnetometer, and the blocking temperature can be analyzed by reducing the temperature of the sample until the measured magnetization stops changing.

Interesting questions that arose from this modeling work include: i) which location on the disk does writing take place at, and ii) how long does it take to write into a HDD. Unfortunately, without a 3-D thermal and magnetization profile of the writing head and sample, it is impossible to determine a specific location at which “writing” happens for a disk at a given angular speed. However, our results here show what the optimal cooling rate, magnetic field strength and angles are for a given Co-Pt medium, which is useful to design the write head. Nonetheless, there is still a lot of experimental work that has to be done with regards to analyzing and evaluating the magnetization and thermal profiling of Co-Pt. With regards to waiting for writability, the wait time after heating a sample at room temperature to its Curie temperature, then back down to room temperature can be tested through a future experiment. For these simulations, the heat was uniformly distributed throughout the sample. Our work has provided a starting point by finding a way to perform field cooling as a function of time, and extracting the blocking temperature and switching probability from it. The next step could be to analyze the wait time for writability by simulating how a heat pulse affects the switching of a medium as a laser profile moves with respect to a patch of grains in a medium with the use of VAMPIRE’s laser pulsing functions. This allows to establish a lateral thermal gradient, which allows for testing different combinations of grains and how the thin-film’s writability is affected. That way, more detail could be obtained with regards to the magnetization dynamics and how they are affected by adjusting the laser profile, and ways of performing field cooling in a way that produces the maximal switching probability at any given set of conditions.

To summarize, more experimental work should be done with regards to the thermal and magnetization profile of Co-Pt thin-films, along with the specific interlayer structure. Additionally, more experiments regarding minimizing the areal density and writing speed of the HAMR system should be performed. Our work indicates that samples with a larger K_u value should be further investigated as they provide more flexibility in tailoring the magnetic properties, meaning that the areal density and writing speed of HDD's can be optimized. On top of that, our work also provides a method of utilizing HAMR systems by finding the magnetic field, cooling rate and magnetic field angle to attain writability for a given sample. To ensure accurate results with regards to the optimal material parameters and simulation conditions, and details with regards to why things happen (analysis of magnetization dynamics at higher temperatures), more detailed modelling and experimental analyses with samples with higher concentrations of platinum should be performed.

REFERENCES

[1] S. Bhargava and E. Yablonovitch, "Lowering HAMR near-field transducer temperature via inverse electromagnetic design," IEEE, Berkeley, 2015.

[2] L. Ceci, "Hours of video uploaded to YouTube every minute as of February 2022," 2022.

[3] O. Hovorka, S. Devos, Q. Coopman, W. J. Fan, C. J. Aas, R. F. L. Evans, X. Chen, G. Ju and R. W. Chantrell, "The Curie temperature distribution of FePt granular magnetic recording media," Applied Physics Letters, 2012.

[4] F. G. Sanchez, "1.2 Magnetic recording crisis and challenges," Madrid.

[5] B. T. Nguyen, S. Ruta, O. Hovroka, R. F. Evans and R. W. Chantrell, "Influence of finite-size effects on the Curie temperature of L10−FePt," 2022.

[6] M. Strungaru, B. Nguyen, K. Yuanmae, R. Evans, R. Chantrell, P. Chureemart and J. Chureemart, "HAMR switching dynamics and the magnetic recording quadrilemma," 2022.

[7] J. Wang, Y. K. Takahashi and K.-i. Uchida, "Magneto-optical painting of heat current," Nature Communications, Tsukuba, 2020.

[8] L. Cassioli, "Wikipedia," 2005.

[9] K. Oldham, S. Felix, R. Conway and R. Horowitz, "Design and control of a dual-stage disk drive servo system with a high-aspect ratio electrostatic microactuator," IEEE, Seattle, 2008.

[10] J. Einsle, C. Gatel and Bowman, "In situ electron holography of the dynamic magnetic field emanating from a hard-disk drive writer," Nano research, Belfast, 2015.

[11] B. Hayes, "Bit-player," 2016.

[12] F. Ismail, "Western Digital Launched 22TB and 26TB Hard Drives," 2022.

[13] M. Chapline, C. Papusoi, A. Ajan and P. Dorsey, "Characterization of the Magnetic Properties of HAMR Media Using the Temperature Dependence of the AC Susceptibility," San Jose, 2015.

[14] R. Wood, "Future hard disk drive systems," San Jose, 2008.

[15] T. Coughlin, "We Need A Boost In HDD Areal Density!," Forbes, New York, 2022.

[16] J. Handy, "Why SSD and HDD Prices Move in Parallel," 2016.

[17] Y. Hu, H. Wu, Y. Meng and D. Bogy, "Head flying characteristics in heat assisted magnetic recording considering various," American Institute of Physics, Berkeley, 2018.

[18] M. Daniel, R. Arun and P. Sabareesan, "Impact of magnetic surface anisotropy on the precessional switching of magnetization in Pt-alloy nanofilms," Physica B, Kolkota, 2012.

[19] M. Tzoufras and M. Grobis, "Dynamics of single-domain magnetic particles at elevated temperatures," New Journal of Physics, 2015.

[20] S. Eimer, H. Cheng, J. Li, X. Zhang, C. Zhao and W. Zhao, "Perpendicular magnetic anisotropy based spintronics devices in Pt/Co stacks under different hard and flexible substrates," Science China Information Sciences, Beihang, 2021.

[21] H. Kirchmayr, "Magnetic Anisotropy," Encyclopedia of Materias: Science and Technology, 2001.

[22] A. Lyberatos, D. Weller and G. Parker, "Finite size effects in L1o-FePt nanoparticles," Journal of Applied Physics, San Jose, 2013.

[23] P. M. Robinson, "Long-Range Dependence," London School of Economics, London.

[24] W. Scholz, J. Fidler, T. Schrefl, D. Suess, H. Forster, R. Dittrich and V. Tsiantos, "Numerical micromagnetic simulation of Fe–Pt nanoparticles with multiple easy axes," Journal of Magnetism and Magnetic Materials, Vienna, 2004.

[25] R. Boardman, "Exchange Energy". https://www.southampton.ac.uk/~rpb/thesis/node18.html

[26] X. Bi, C. Qiu, F. Qin, J. Huang and Y. Hongtao, "Controlling Exchange Interactions and Emergent Magnetic Phenomena in Layered 3d-Orbital Ferromagnets," Advanced Physics Research, 2023.

[27] "What's Magnetic Moment?," Stanford Magnets, Stanford.

[28] K. P. Driver, "The Role of Relativity in Magnetism: Calculating Magnetic Moment of Solids," 2006.

[29] D. Go, F. Freimuth, J.-P. Hanke, F. Xue, O. Gomonay, K.-J. Lee, S. Bluegel, P. M. Haney, H.-W. Lee and Y. Morkrousov, "Theory of current-induced angular momentum transfer dynamics in spin-orbit coupled systems," American Physical Society, Seoul, 2021.

[30] P. Fears, "Magnets and the Curie Temperatrue," Bunting, Berkhamsted, 2021.

[31] W. Law, T. Jin, X. Zhu, R. Nistala, N. Thiyagarajah, C. Seet and W. Lew, "Perpendicular magnetic anisotropy in Co/Pt multilayers induced by hcp-Ho at 400 °C," Journal of Magnetism and Magnetic Materials, Nanyang, 2019.

[32] R. F. Evans, "Vampire - Simulations," 2021. https://arxiv.org/pdf/2210.07875.pdf

[33] "https://ocw.mit.edu/courses/3-024-electronic-optical-and-magnetic-properties-of-materials-spring-2013/80b04608c40a0418a365206221532089_MIT3_024S13_2012lec25.pdf," Massachusetts , 2020.

[34] R. V. Ababei, "Atomistic Spin Simulations of Heat Assisted Magnetic Recording Media," University of York, United Kingdom, 2019.

[35] I. Bruvera, P. Zélis, M. Calatayud and G. Goya, "Determination of the blocking temperature of magnetic nanoparticles: The good, the bad, and the ugly," American Institute of Physics, La Plata, 2015.

[36] K. Bately, M. Nguyen, I. Kamboj, C. Korostynksi, E. Aydil and C. Leighton, "Quantitative Understanding of Superparamagnetic Blocking in," American Chemical Society, 2020.

[37] L. Afremov, S. Anisimov and I. Iliushin, "Modeling of the blocking temperature of a system of core/shell nanoparticles," Chinese Journal of Physics, Vladivostok, 2020.

[38] J. Hong, X. Li, O. Lee, W. Tian, S. Khizroev, J. Bokor and L. You, "Demonstration of spin transfer torque (STT)," American Institute of Physics, Wuhan, 2019.

[39] B. Jinnai, C. Zhang, A. Kurenkov, M. Bersweiler, H. Sato, S. Fukami and H. Ohno, "Spin-orbit torque induced magnetization switching in Co/Pt multilayers," Applied Physics Letters, Tokyo, 2017.

[40] M. A, W. Pantarsi, W. Daeng-am, S. E. Rannala, R. S.I, R. W. Chantrell, P. Chureemart and J. Chureemart, "Magnetization dynamics of granular heat-assisted magnetic recording media by means of a multiscale model," APS - Physical Review B, Mahasarakham, 2020.

[41] R. F. L. Evans, U. Atxitia and R. Chantrell, "Quantitative simulation of temperature dependent magnetization dynamics and equilibrium properties of elemental ferromagnets," APS: Physical Review Section B, York, 2015.

[42] H. Li, "Storage Physics and Noise Mechanism in Heat-Assisted Magnetic Recording," Carnegie Mellon University, Pittsburgh, 2016.

[43] O. Fesenko and P. Nieves, "Modeling of Ultrafast Heat- and Field-Assisted Magnetization Dynamics in FePt," American Physics Society, 2016.

[44] J. Zhu and Y. Yan, "Incoherent Magnetic Switching of L10 FePt Grains," IEEE Transactions on Magnetics, Pittsburgh, 2020.

[45] X. Wu, R. v. d. Veerdonk, B.Lu and D. Weller, "Coherent vs. incoherent switching for elongated CoPt-O grains in high-anisotropy medium," Journal of Magnetism and Magnetic Materials, Pittishburg, 2006.

[46] A. Dobrynin, P. Lievens and K. Temst, "Exchange coupling in hybrid magnetic nanocluster systems; Exchange koppeling in hybride nanoclustersystemen.," ORCID, Leuven, 2006.

[47] L. Filipovic, "1.2.1: Atomistic Approach".

[48] R. Evans, "Atomistic Spin Dynamics," Springer International Publishing, Heslington, 2018.

[49] M.Menarini and V.Lomakin, "Thermal fluctuations in the Landau-Lifshitz-Bloch model", 2020

[50] Y. Pomeau and J. Piasecki, "The Langevin equation," Tuscon, 2017.

[51] R. Evans, W. Fan, P. Chureemart, T. A. Ostler, M. Ellis and R. Chantrell, "Atomistic spin model simulations of magnetic nanomaterials," Journal of Physics: Condensed Matter, Yorkshire, 2014.

[52] M. Potthoff, D. Guetersloh and M. Sayad, "Macrospin approximation and quantum effects in models for magnetization reversal," Cornell University, Fisica, 2012.

[53] Daniel, Siying and Byunghun, "Beach Group," MIT Press, Massachusetts.

[54] O. D. Echeverri, "LLG Equation," Columbia.

[55] "Mathematics & Science Learning Center," San Joaquin.

[56] L. Westover, "Solution Methods for IVPs: Heun's Method," 2020.

[57] R. Evans, W. Fan, C. P, T. Ostler, M. Ellis and R. Chantrell, "Atomistic spin model simulations of magnetic nanomaterials," IOP Publishing, York, 2014.

[58] U. Atxitia and R. e. a. Chantrell, "Ultrafast Spin Dynamics: The Effect of Coloured Noise," Physical Review Letters, Madrid, 2009.

[59] M. Su, T. J. Webster, M. Hossain and A. D. Paro, "Monte Carlo and analytic simulations in nanoparticle-enhanced radiation therapy," National Library of Medicne, 2016.

[60] A. Meo, R.W.Chantrell and R. Evans, "VAMPIRE - Calculation of anisotropy energy and temperature dependence of anisotropy," Department of Physics, University of York, York.

[61] R. F. Evans, "Vampire - Day 5".

[62] A. Surpi, T. Shelyakova, M. Murgia, P. Greco, M. Fini and V. Dedju, "Versatile magnetic configuration for the control and manipulation of superparamagnetic nanoparticles," Scientific Reports, Bologna, 2023.

[63] M. Ameri, M. Shegheft, M. Akbari, S. Zamanzadeh and E. Nasiri, "A comparison of accuracy and computational time," Sage Journals, Tehran, 2012.

[64] A. Makarov, "Chapter 5 - Macro and Micromagnetic Approaches," Vienna.

[65] A. Belemuk, O. Udalov, N. Chtchelkatchev and I. Beloborodov, "Competition of magneto-dipole, anisotropy and exchange interactions in composite multiferroics," PACS, Troitsk .

[66] F. Slanovc, C. Volger, O. Muthsam and D. Suess, "Systematic parameterization of heat-assisted magnetic recording switching probabilities and the consequences for the resulting SNR," Vienna.

[67] G. Rijnders and D. A. Blank, "Build your own superlattice," Nature, Enschede, 2005.

[68] F. Bellelli, "The fascinating world of Voronoi diagrams," Towards Data Science, 2022.

[69] S. S. Snibbe, "Introduction to Voronoi Diagrams," Brown University, Rhode Island, 1993.

[70] A. Miu, "Lecture 7: Voronoi Diagrams," MIT, Massachusetts, 2001.

[71] C. N. Senent, K. Eiler, P. Salvador, J. Sort and E. Pellicer, "Lightweight macroporous Co-Pt electrodeposited films with semi-hard-magnetic properties," ScienceDirect, Barcelona, 2022.

[72] R. F. Evans, "Atomistic spin model simulations of magnetic nanomaterials," Journal of Physics and Condensed Matter, York, 2014.

[73] R. Evans, "Vamipre - Atomistic Simulation".

[74] "Uppsala Atomistic Spin Dynamics," Department of Physcis and Astronomy - Uppsala, Uppsala.

[75] S. Lepadatu, "Boris Micromagnetics," Jeremiah Horrocks Institute, Preston.

[76] F. Koehler, R. Mukherjee and P. Schmelcher, "Exploring Disordered Quantum Spin Models with a Multi-Layer," Center for optical and quantum technologies, Hamburg, 2023.

[77] J. Humlicek, "Data Analysis for Nanomaterials: Effective Medium Approximation, Its Limits and Implementations," Springer, Berlin, 2013.

[78] R. Evans F.L., "Vampire User Manual".

[79] D. Garanin, "Self-consistent Gaussian approximation for classical spin systems: Thermodynamics," Physical Review B, Hamburg, 1996.

[80] " 12.2: The Arrangement of Atoms in Crystalline Solids".

[81] "Cobalt - Tight Binding Parameters".

[82] "Tight binding parameters - Platinum".

[83] "Cobalt (Cubic) - Summary".

[84] "Platinum - Summary (Cubic)".

[85] M. Charilaou, C. Bordel, P.-. Berche, B. B. Maranville, P. Fischer and F. Hellman, "Magnetic properties of ultrathin discontinuous Co/Pt multilayers: Comparison with short-range ordered and isotropic CoPt3 films," American Physical Society, San Diego, 2016.

[86] G. F. Sanchez, "Temperature dependence of the bulk anisotropy," Rocio Yanes.

[87] V. Guo, B. Lu and B. Valcu, "A survey of anisotropy measurement techniques and study of thickness effect on interfacial and volume anisotropies in Co/Pt multilayer media," AIP Publishing, 2006.

[88] J. Spiff, "Accuracy v.s. Timestep for different techniques".

[89] G. Grinstein and R. Koch, "Switching probabilities for single-domain magnetic particles," American Institute of Physics, New York, 2005.

[90] K. Livesey, S. Ruta, A. Anderson, D. Baldomir, R. Chantrell and D. Serantes, "Beyond the blocking model to fit nanoparticle ZFC/FC magnetisation curves," Scientific Reports, 2018.

[91] F. Ruffino and M. Grimaldi, "Nanostructuration of Thin Metal Films by Pulsed Laser Irradiations: A Review," 2019.

[92] S. t. A. o. S. Nanoparticles, "Hu, M; Butt, H; Landfester, K; Bannwarth, M; Wooh, S; Aubin, H," American Chemical Society, 2019.

[93] T. Coughlin, “A new phase of magnetic recording,” Forbes, 2023